Nondestructive Evaluation Advancements for Damage Detection in Concrete

A THESIS
SUBMITTED TO THE FACULTY OF
UNIVERSITY OF MINNESOTA
BY

Katelyn Freeseman

IN PARTIAL FULFILLMENT OF THE REQUIREMENTS
FOR THE DEGREE OF
Doctor of Philosophy

Advisor: Lev Khazanovich

June 2016

Acknowledgements

I would first like to thank my advisor, Dr. Lev Khazanovich, for his guidance, support, and technical expertise throughout this process. I would also like to thank Dr. Arturo Schultz, Dr. Adam Rothman, and Dr. Mihai Marasteanu for serving on my committee. I would like to also acknowledge Dr. Kyle Hoegh for his assistance and mentoring, and my fellow graduate student colleagues for their help and encouragement during my time at the University of Minnesota. Special thanks to Paul Bergson, Jake Robole, Anna Flintrop and Lucio Salles for their much appreciated experimental assistance. Aziz Asadollahi generously shared his elastodynamic finite integration technique code and contributed to the numerical simulation efforts.

Finally, I would like to thank my family for their constant support and encouragement. To my husband for his reassurance and unwavering confidence in me, and to my friends for their comic relief during this, at times, stressful endeavor.

Abstract

While concrete is the most widely used civil engineering material, damage detection and progression in concrete structures have still proven to be difficult to address, especially when only one-sided access is available. New technological advances in nondestructive testing technology have created the opportunity to better utilize ultrasonic waves to aid in this damage detection process. However, interpretation of the signal data is a challenging task which often requires subjective assessments.

This thesis addresses these limitations via the utilization of ultrasonic array technology for nondestructive damage detection purposes. The ultrasonic shear velocity array system used for this research is particularly advantageous because it can obtain measurements on virtually any concrete specimen, from columns and beams to concrete pavements, and provides a wealth of data from a single measurement. Novel signal interpretation methods were developed for several important concrete applications.

Detection of load-induced damage in laboratory beams and a full-scale reinforced concrete column, as well as standard life-cycle damage in concrete pavements caused by freeze thaw or alkali-silica reaction degradation were considered. These investigations culminated in the development of successful and efficient quantitative damage detection methods. Finally, the development and refinement of a simulation program allowed for verification of the experimental investigation and a greater understanding of signal results.

Table of Contents

List of Tables

List of Figures

CHAPTER 1: INTRODUCTION

The nondestructive evaluation of concrete involves unique complications due to the heterogeneous nature of the material itself. The presence of reinforcement and aggregates impose additional challenges when attempting to detect damage. Moreover, the demand for in-situ evaluation of concrete structures with associated access limitations (i.e. one-sided access to pavements), provide further impediments. While previous methods have been employed for these reasons in the past, an in-situ and objective method for nondestructively detecting subsurface damage has yet to be successfully developed and implemented.

To address this shortcoming in the nondestructive testing realm, the research presented here utilized a linear array of dry point contact transducers which emit shear waves. This technology, called MIRA, was chosen due to its high measurement repeatability, immunity to moisture conditions, and avoidance of computation-intensive nonlinearity and mode conversion efforts. This device in particular is useful in that the shear wave propagation and subsequent data analyses techniques allow for a deeper understanding of the condition of concrete specimens due to the multitude of data it provides.

The goal of the research presented in this dissertation was to conduct an experimental and analytical investigation to determine the effectiveness of an ultrasonic linear array, which uses shear-horizontal waves, in determining damage present in a variety of concrete applications. The research procedure can be divided into two major research tasks, Damage Detection Applications and a Numerical Simulation.

1. Damage Detection Applications: A variety of damage scenarios were analyzed to determine applicability and effectiveness. These experimental efforts can be further divided based upon the type of damage considered.
    a. Load-induced Damage: An ultrasonic device was utilized to monitor the condition of a column subjected to simulated earthquake loading, and to test several iterations of laboratory beam specimens which underwent static and cyclic loading protocols. The data was utilized to determine if subsurface damage was detected by the device and subsequent analysis methods. Both shear wave velocity and reconstruction analyses were performed.
    b. Environmental Damage: Data was collected on several slab specimens which had various levels of freeze thaw or alkali-silica reaction (ASR) damage. The data from the experimental investigation was utilized to perform signal analysis on the results of the shear velocity array system. A quantitative indicator of the severity of damage was developed, and compared with corresponding reconstruction results.
2. Numerical Simulation: A program which aims to simulate the impulse time histories generated by MIRA was developed and refined. Refinement of this program included steps to minimize differences between the simulation results and experimental signals. In doing so, results from the previous tasks were verified and a deeper understanding of signal behavior was attained.

The content of this dissertation is divided into the following chapters:

Chapter 2: A literature review covering previous nondestructive testing methods with the broad viewpoint of general damage detection applications. A background of the ultrasonic device utilized for this research is also provided here.

Chapter 3: The experimental investigation of a reinforced concrete column subjected to earthquake loading is provided, as well as a discussion of findings.

Chapter 4: The analysis of early age damage associated with early opening to traffic was investigated via the loading of laboratory flexure beams and the results are presented here.

Chapter 5: Damage detection applications relating to environmental damage are provided here. Subsections include freeze thaw damage and alkali-silica reaction damage.

Chapter 6: The development and refinement of the numerical simulation is detailed. Trial simulations were executed and the results are compared to the experimental findings.

Chapter 7: A summary of the findings from both the experimental and simulation investigation are provided along with recommendations for future work that expand or support this research.

CHAPTER 2: LITERATURE REVIEW

This chapter discusses the applications and limitations of existing nondestructive testing methods. This includes a summary of common active testing methods, as well as a thorough description of the ultrasonic linear array device utilized for this research. Further background information is given regarding the increased capabilities provided by wave propagation simulation technology. Finally, the limitations of the discussed methods are outlined and serve as the motivation behind the research presented in this thesis.

2.1 Nondestructive Testing Methods

Many nondestructive testing methods have been utilized in the past to gain insight on the inner condition of structural specimens. Common active techniques that have the potential to detect subsurface conditions include: impact echo, ultrasonic pulse velocity (UPV), ultrasonic wave reflection, ground penetrating radar (GPR), and nonlinear methods. Relevant literature regarding freeze thaw and alkali-silica reaction damage are included in later chapters.

2.1.1 Conventional Impact Echo (IE)

Conventional impact echo (IE) is one commonly used elastic wave based method involving the generation of compression, shear, and Rayleigh waves using a mechanical impact at the surface (Schubert et al., 2001). Spectral analysis techniques are employed in this technique for signal interpretation of wave reflections caused by changes in acoustic impedance or the presence of boundaries (Scott et al., 2003). Because of this, IE can be used for thickness determination or the detection of other plate-like inclusions

caused by planar layer interfaces. However, IE testing can be time consuming and includes only one signal pair per scan, hindering special diversity. Because of this limitation, complex geometries associated with irregular flaws creates difficulties for the implementation of this technique (Carino 2001, Schubert 2008, Schubert 2003). Advancements such as air-coupled impact echo have increased measurement acquisition efficiency and introduces the opportunity for multiple measurement pairs (Borwick 1990, Buckley 1999, Popovics 2012, Zhu et al. 2002, Zhu et al. 2004, Zhu et al. 2007).

2.1.2 Ultrasonic Pulse Velocity

Ultrasonic pulse velocity (UPV) is an elastic wave-based method in which impulses are sent and received via ultrasonic transducers (Popovics et al., 1992). A liquid coupling, such as grease, is traditionally used to transfer the pulse into the concrete and back to the receiving transducer. Because of this, UPV can be time consuming and difficult to implement for in-situ testing applications.

Graveen proposed measurement of P-wave velocity as a supplement to increase the overall confidence of the maturity-based estimate of concrete strength (Graveen 2001). However, the measurement requires time-consuming application of fluid couplant to allow for transmission and reception of the wave. Despite the problems associated with speed and coverage of the method, the study showed that "the correlation of the P-wave velocity to concrete strength is supported by the similarity between the strength-age relationship and the P-wave velocity-age relationship" for field tests, and reducing error in the P-wave velocity measurements would increase the confidence in the reported P-wave velocity.

2.1.3 Ultrasonic Wave Reflection

The ultrasonic wave reflection method involves measuring the reflection coefficient of shear waves between a steel plate and the concrete pavement. The reflection coefficient is a ratio dependent upon density and wave velocity of the two materials; essentially representative of the change in amplitude between the two reflections. The reflection coefficient is equal to one when the PCC is in a liquid state because shear waves cannot be transmitted through liquids. The reflection coefficient decreases as the PCC hardens and eventually stabilizes at a final value. This coefficient is governed by the dynamic shear modulus- a value that is based upon the level of hydration present. Wave reflection methods are not affected by curing temperature differences, though it is thought that the compressive strength and reflection coefficient can be compared due to a common dependence on hydration (Voigt et. al 2006). P-wave velocity changes do not necessarily signal changes in strength, but the overall trend of rate of P-wave velocity can be useful for strength prediction purposes (Voigt et al 2005). Additionally, wave reflection measurements are repeatable for reflection loss of mortar, but these measurements cannot be predicted for concrete because of the presence of aggregates at the local level (Voigt 2003 and 2005).

2.1.4 Ground Penetrating Radar (GPR)

Ground penetrating radar (GPR) involves the transmitting of electromagnetic waves into a specimen and the resulting reflection of the waves at areas of differing dielectric characteristics gives insight. GPR has been used in the past to determine target depth based upon wave speed, which is dependent upon the dielectric properties (Abdallah 2009; Clemena 1991; Cao et al. 2008; Cao et al. 2011; Cao 2011; Economou et al. 2012;

Louliza et al. 2001; Maierhofer 2003; Scott et al. 2000; Plati et al. 2012;). GPR has also been used for structural assessment, detection of reinforcement corrosion, and characterization of pavement structure (Arndt 2011; Benedetto et al. 2012; Catapano et al. 2012; Clemena et al. 1992; Li et al. 2008; Maser 1996, 2000 and 2008; Maser et al. 1990; Morey 1998; Scullion et al. 1995). GPR has high measurement efficiency, though the measurement accuracy decreases with increases in speed and detecting non-uniform cracks is difficult (Griffiths et al., 1999). Additionally, GPR is highly sensitive to moisture conditions since water has a high dielectric constant (Scott et al 2003; Griffiths et al., 1999).

2.1.5 Nonlinear Methods

Nonlinear ultrasonic methods have been employed to characterize changes in the microstructure of materials with some success, specifically through the use of Rayleigh waves. The heterogeneous nature of concrete, however, introduces issues associated with scattering and attenuation. Kim et al. proposed the application of the second harmonic generation in Rayleigh waves to quantify microcracks in mortar and concrete (2014). The methods utilized included an air-coupled transducer for nonlinear ultrasonic measurements. This method saw success in determining nonlinearity parameters and the corresponding indication of concrete condition. However, these methods require the use of nonlinear principles, adding significant complexity which can be avoided via the use of an ultrasonic array system.

Additional work using nonlinear impact resonance acoustic spectroscopy techniques to characterize damage in concrete specimens was performed by Leśnicki et

al. (2011). The elastic modulus relationship utilized can be seen in Equation 1 below. Specifically, damage associated with alkali-silica reaction was analyzed via the analysis of the nonlinear parameter. This nonlinear parameter is a ratio of normalized resonance frequency shift with acceleration amplitude, as shown in Equation 2 below.

$$E = E_0[1 + \beta\varepsilon + \delta\varepsilon^2 + \alpha(\Delta\varepsilon + \varepsilon\,\mathrm{sgn}(\dot{\varepsilon}))] \quad (1)$$

$$\frac{f_0 - f}{f_0} = \alpha'\Delta\varepsilon \quad (2)$$

Where E_0 is the linear elastic modulus, β is the parameter for quadratic anharmonicity, δ is the parameter for cubic anharmonicity, ε is the strain, Δε is the strain amplitude, $\dot{\varepsilon}$ is the strain rate, sgn($\dot{\varepsilon}$)=1 if $\dot{\varepsilon}$>0, -1 if $\dot{\varepsilon}$<0, and 0 if $\dot{\varepsilon}$=0, α' is proportional to the hysteresis nonlinearity parameter α, f_0 is the linear resonance frequency and f is the resonance frequency at increased excitation amplitude.

This nonlinearity parameter, α', was found to change drastically with an increase in alkali-silica reaction damage (Leśnicki et al. 2013). However, only one sensor was utilized for this analysis and very small specimens were used leading to questions regarding size effect and in-situ applicability.

2.1.6 Limitations of Discussed Methods

The methods described in sections 2.1.1 to 2.1.5 have been used to detect damage in concrete structures, among other applications. The limitations of their applicability, however, have been evident in previous research due to complications such as complex geometry, large depths, sensitivity to moisture conditions, or the lack of access to more than one side of the structure. Additionally, measurement efficiency was low in some

instances due to surface preparation requirements or single transducer pair limitations. In order to mitigate these issues, an ultrasonic linear array technique was selected for this research due to its large penetration depth, improved accuracy associated with redundant measurement acquisition, independence of moisture conditions, and ability to obtain results via one–sided access without nonlinear effects.

2.2 Ultrasonic Linear Array

While conventional nondestructive testing methods provide useful information as described in section 2.1, ultrasonic array technology provides an opportunity to mitigate issues with limited transducer pairs and associated signal variability via the use of sending and receiving transducer pairs at set spacings. Spatial diversity is achieved through an array of elements within a single transducer.

To allow for field testing of heterogeneous materials such as PCC, dry point contact (DPC) transducers are used, which eliminates the need for a manual mechanical impact and time-intensive surface coupling. The use of DPC transducers also introduces multiple impulse angles that can increase reliability of measurements, allowing for reduced transducer spacing and greater precision (Bishko et al. 2008). One version of DPC ultrasonic array technology, MIRA, is shown in Figure 1 and consists of a linear array of transducers.

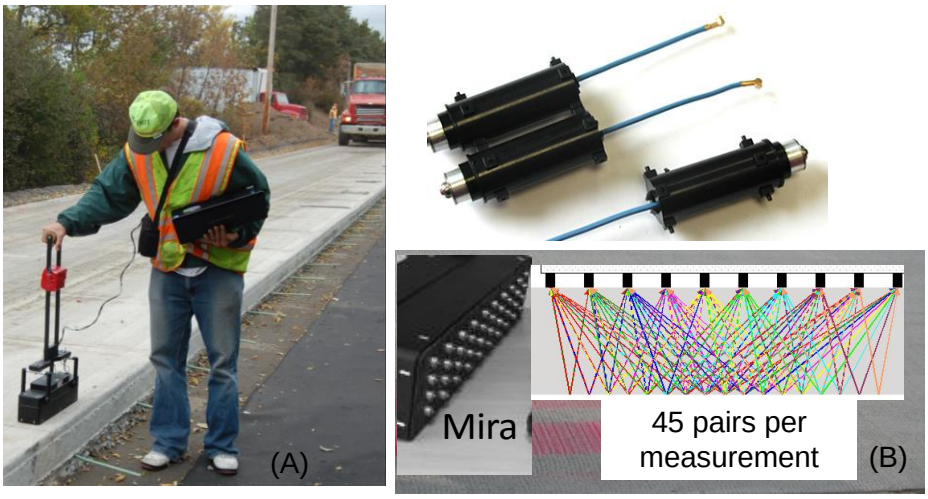

Figure 1. MIRA ultrasonic linear array device (Hoegh 2013).

MIRA is an ultrasonic shear wave device that utilizes a linear array of 40 dry point contact transducers for diagnostics. This array is arranged into groups of 4 transducers, acting essentially as one unit, which results in out-of-plane shear waves acting in a linear fashion. The emitted waves travel into the specimen, allowing for cross-sectional analysis. Because shear waves, and not compression waves, are utilized, the results are independent of moisture conditions. Each set of four transducers interacts with the remaining nine sets of transducers, resulting in 45 unique transducer pairs (i.e., 1 to 2, 1 to 3, 1 to 4,….8 to 9, 8 to 10, 9 to 10) as shown in Figure 2. The spacing between adjacent transducer channels is 40 mm (1.6 in.). As such, each acquired measurement results in nine impulse histories at 40 mm (1.6 in.) spacing, eight at 80 mm (3.1 in.) spacing, seven at 120 mm (4.7 in.) spacing, six at 160 mm (6.3 in.) spacing, five at 200 mm (7.9 in.) spacing, four at 240 mm (9.4 in.) spacing, three at 280 mm (11.0 in.) spacing, two at 320 mm (12.6 in.) spacing and one at 360 mm (14.2 in.) spacing. The utilization of this array setup allows for increased redundancy and measurement

confidence. The incorporation of multiple impact angles is ideal for the analysis of heterogeneous materials, which is essential for concrete applications (Hoegh 2013).

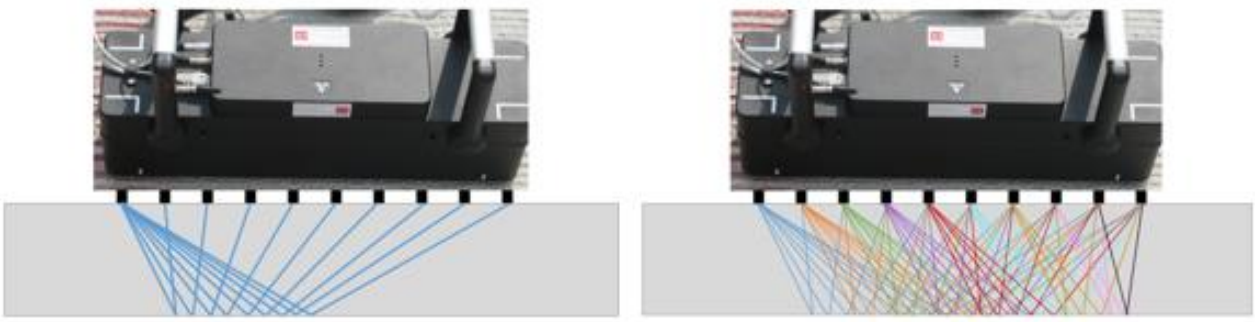

Figure 2. MIRA transducer interactions emitted from transducer 1 (left) and for all transducer pairs (right).

The 45 unique impulse time histories provide valuable information about the specimen. The impulse time histories contain reflectivity information, caused by any change in acoustic impedance that the wave encounters. Changes could be caused by air voids, damage, inclusions, or layer interfaces. An example impulse time history is shown in Figure 3 (left), along with a schematic which would result in this type of time history (right). The direct arrival pulse is the result of a portion of the wave traveling the shortest/fastest distance, in this case along the surface of the specimen, and being received by another transducer. The reflected pulse is the result of the wave propagating through the specimen and encountering a change in acoustic impedance, in this case the bottom surface of the specimen, and reflecting back to the surface. An impulse time history is created by each of the 45 transducer pairs, resulting in a large amount of information and data per scan.

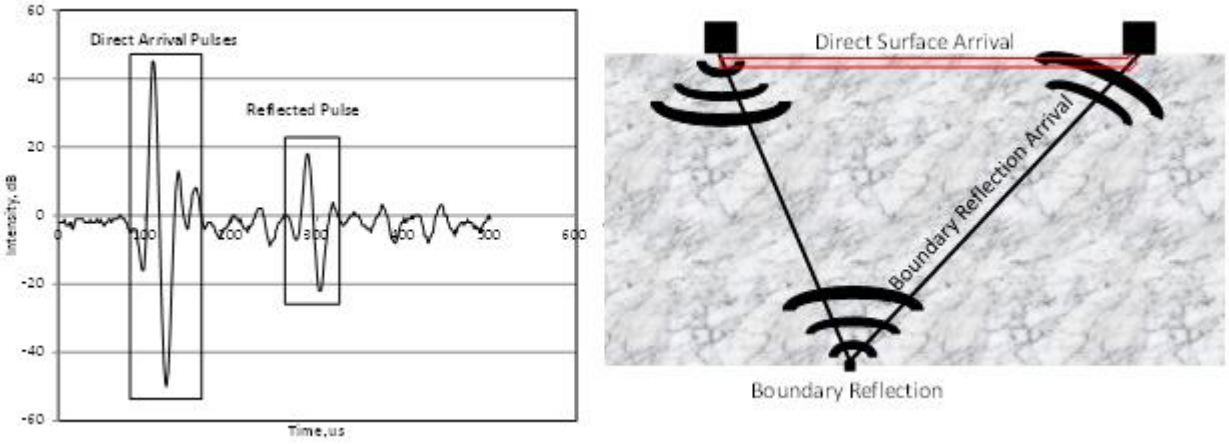

Figure 3. Example impulse time history (left), and corresponding cross section schematic (right) (Hoegh 2013).

MIRA can be used for various nondestructive subsurface diagnostic applications including poor consolidation and non-uniformity (Hoegh et al., 2012a), de-bonding between layers (Hoegh et al., 2012c), horizontal delamination (Hoegh et al. 2012b; Hoegh et al., 2013), and joint deterioration and spalling or poor consolidation around dowels (Hoegh et al. 2012c; Hoegh et al., 2013).

2.2.1 Shear Velocity Determination

In addition to providing ultrasonic reflection information, the direct arrival of the multiple channels can provide velocity information as well. The impulse time histories (such as that shown in Figure 3, left) can be utilized to determine important properties of the specimen, such as calculating the shear wave velocity. Because the transducer spacing is known, as well as the time of the direct arrival pulse, the shear wave velocity can be

calculated using the redundant information provided by the 45 pairs. This velocity can be calculated as follows:

$$v_s = \frac{x_{i,j}}{t_{i,j}} \tag{3}$$

Where v_s is the calculated shear wave velocity, i and j are the transducers 1 through 10, $x_{i,j}$ is the distance between transducer i and j, and $t_{i,j}$ is the time of the direct arrival pulse for the time history related to transducer i and j. While Equation 3 is quite simplistic, multiple transducer pairs are needed to calculate velocity accurately due to the time delay incorporated into the system. By plotting the $x_{i,j}$ and $t_{i,j}$ values for all transducer pairs, a best fit linear trendline will reveal the actual shear wave velocity, removing the time delay from all points because the delay is a constant for all transducers. An example plot, with corresponding trendline can be seen in Figure 4. As can be seen, the data points are highly linear, which allows for the accurate determination of shear wave velocity (in this case, 2.3007 mm/us or 2301 m/s) when the direct arrival is evident. This calculation is possible due to the repeatability of equally-spaced transducer pairs and the redundancy of data provided by the linear array system (Hoegh 2013). It should be noted that this calculation is only valid when the concrete is in sound condition, or without shallow damage which would inhibit the direct arrival.

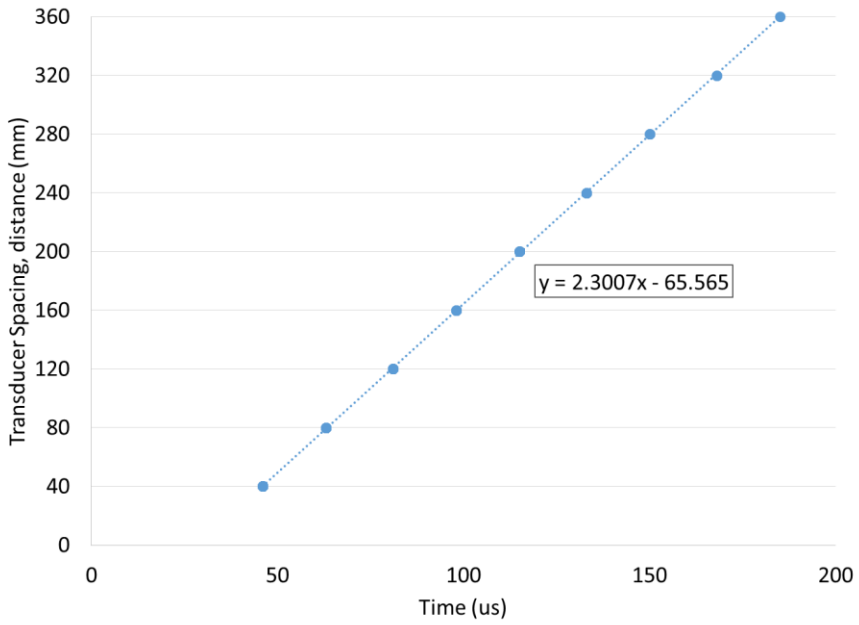

Figure 4. Example array data for calculation of shear wave velocity.

Previous research has shown that this calculated shear velocity is independent of specimen type, given the same concrete mix. Figure 5 shows the results of beam and slab measured velocities at various concrete ages. It can be observed that there is a very good agreement between the beam and slab velocities of the same mix, as shown by the linear and nearly 1:1 relationship. The monotonic relationship is positively correlated with concrete age, allowing for an extremely accurate, while practical, estimate of concrete properties.

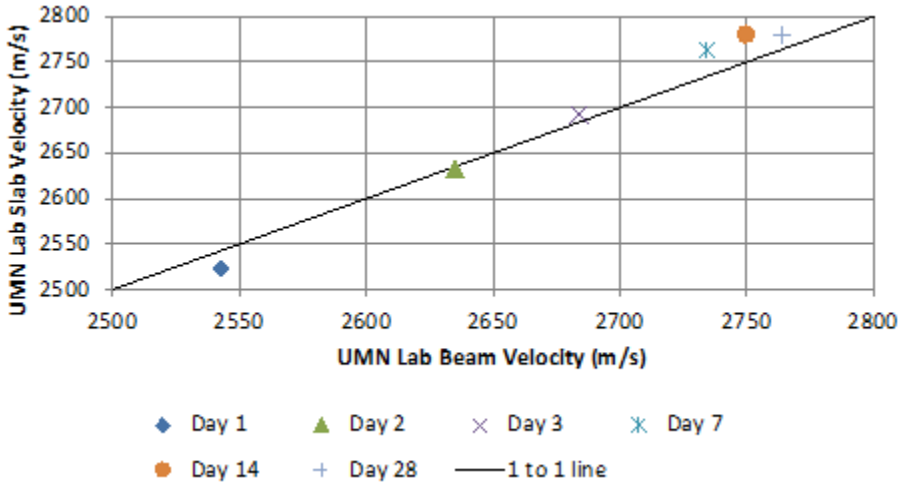

Figure 5. Ultrasonic array measured shear wave velocities for concrete beams vs. slabs at various concrete ages (K. Hoegh, personal communication).

2.2.2 Reconstruction Formulation

This shear velocity information described in section 2.2.1 can be further implemented to allow for the formulation of visual reconstructions. For visual analysis of cross section characteristics, the unique impulse time histories provided by MIRA can be used to create reconstructive images of the cross section of interest. The method used to create these images is called Synthetic Aperture Focusing Technique (SAFT). The following equations are utilized in order to create SAFT B-scans, a typical reconstruction:

$$\hat{o}_{i,k} = \sum_{e=1}^{T-1} \sum_{r=e+1}^{T} \mathrm{A}(x_r, x_e, x_i, z_k) \Psi_{e,r}(x_i, z_k) \tag{4}$$

where,

$$\Psi_{e,r}(x_i, z_k) = s\left(x_r, x_e, \frac{1}{c}\left(\sqrt{{z_k}^2 + (x_i - x_e)^2} + \sqrt{{z_k}^2 + (x_i - x_r)^2}\right)\right) \tag{5}$$

where $\hat{o}_{i,k}$ is the image reflectivity assigned to each position within the ROI, T is the number of transducer locations, e and r are the indexes for the emitting and receiving

transducers, and i and k are the indexes for the horizontal and vertical positions of the ROI, such that the ROI is represented by a W x D set of points contained in W columns and D rows, s is the magnitude of the response at the evaluated time of flight for the given transducers, x'e and x'r, and A is the apodization coefficient (Hoegh and Khazanovich 2015). This apodization factor accounts for the various incident angles and other traits of the signal (Balmer 1992).

It is then useful to implement Hilbert transform in order to calculate the instantaneous attributes of the series, computed via equations (6) through (11):

$$HT(z) = \frac{1}{\pi}\int_{-\infty}^{\infty}\frac{f(s)}{t-s}ds \tag{6}$$

where HT(t) is the Hilbert transform of a given function, f(x). The complex signal, Z(z) is then given by:

$$Z(z) = f(z) + j\,\mathrm{HT}(z) \tag{7}$$

This complex signal can then be calculated at each coordinate of the reconstruction to calculate the instantaneous amplitude:

$$\hat{\boldsymbol{o}}^{IA}(x,z) = \sqrt{\left(\hat{\boldsymbol{o}}(x,z)\right)^2 + \left(\frac{1}{\pi}\int_{-\infty}^{\infty}\frac{\hat{\boldsymbol{o}}(x,s)}{z-s}ds\right)^2} \tag{8}$$

where $\hat{\boldsymbol{o}}^{IA}(x,z)$ is the relative reflectivity that defines the new instantaneous amplitude-based SAFT reconstruction. A typical apodization factor utilized for the creation of these reconstructions is as follows:

$$\mathrm{A}(x'_r, x'_e, x_i, z_k) = \alpha_e(x'_e, x_i, z_k) * \alpha_r(x'_r, x_i, z_k) \tag{9}$$

Where:

$$\alpha_e(x'_e, x_i, z_k) = \frac{z_k}{\sqrt{(x_i - x'_e)^2 + {z_k}^2}} \tag{10}$$

$$\alpha_r(x'_e, x_i, z_k) = \frac{z_k}{\sqrt{(x_i - x'_r)^2 + {z_k}^2}} \tag{11}$$

These equations account for the fact that a transducer can act as both the emitting transducer and as the receiving transducer (Hoegh and Khazanovich 2015). Standard software to create SAFT B-scans is included with MIRA; however, a signature analysis developed at the University of Minnesota (Hoegh 2013) was instead used for greater freedom in the apodization factor, and for the corresponding increased understanding of the reconstruction components.

However, SAFT B-scan reconstructions have their limitations. The edges of each scan reconstruction spans only 400 mm, making comprehensive cross section analysis difficult. To incorporate greater confidence and redundancy via capitalizing on the overlapping nature of the eleven measurements, panoramic reconstructions can improve the results via the compiling of individual SAFT reconstructions (Hoegh 2013). Equation (12) is used to combine the individual reconstructions to create the panoramic reconstructions which have a larger region of interest:

$$\widehat{\boldsymbol{O}}^m_{PAN}(x,z) = \begin{cases} \widehat{\boldsymbol{O}}^{m-1}_{PAN}(x,z), & if\ x < D \\ \max\left(\widehat{\boldsymbol{O}}^{m-1}_{PAN}(x,z), \widehat{\boldsymbol{O}}^m_I\ (\mathrm{x},\mathrm{z})\right), & \text{if D} < \mathrm{x} < x^{m-1}_{PAN} \\ \widehat{\boldsymbol{O}}^m_I\ (\mathrm{x},\mathrm{z}), & if\ x > x^m_I \end{cases} \tag{12}$$

where each SAFT scan, $\widehat{\boldsymbol{O}}^m_I$, where m is the index of the current SAFT scan and I denotes that it is an individual scan, is combined to form the new region of interest, ROI^m_{PAN}. This

region has a vertical dimension of z and a horizontal dimension of x_{PAN}^{m}, and D is the distance from the global origin (Hoegh 2013, Hoegh and Khazanovich 2015, Freeseman et al. 2016).

These panoramic reconstructions can be powerful tools for locating dowels, determining slab thickness, and other applications (Hoegh 2013). However, these reconstructions rely upon the presence of sound concrete and difficulties can arise when significant reinforcement is present.

2.3 Wave Propagation Simulation

Simulations also serve as a valuable tool for improvements in the interpretation of results from nondestructive testing. Simulation programs allow for reverse engineering methods to be applied via comparative analyses. The finite-difference method (FDM) is the dominant method for modeling wave propagation, specifically for structural modeling (Mozco et al. 2010). FDM can be applied to isotropic or anisotropic materials, and is relatively accurate and computationally efficient. Advanced schemes have been developed that allow for a heterogeneous formulation of equations which was not previously possible (Mozco et al. 2010, Levander 1988, Olsen et al. 1995, Graves 1988, Pitarka 1999, Moczo et al. 2002).

The finite element method (FEM) is an alternative method that allows for free surface boundary conditions to be handled easily (Bathe 1996). FEM is very flexible and capable of solving any 3D problem; however, it requires a huge amount of memory and sizable computational time. As such, FEM is less computationally efficient when compared to FDM.

The finite integration technique (FIT) can be used for simulation purposes and was first proposed by Weiland in 1977 to study electromagnetic waves (Weiland 1977). This method is essentially a generalization of the finite difference time domain method (FDTD), and it has tight links to the finite element method (FEM). FDTD is faster than FEM but is not applicable to arbitrary geometry, unlike FIT. Additionally, FEM mass matrices are not diagonal, unlike the ones arising in FIT, when used in the frequency domain.

Fellinger (1991) adapted Weiland's ideas to the governing equations of ultrasonic waves in solids, and developed a numerical procedure called the Elastodynamic Finite Integration Technique (EFIT), which is used for this research. In EFIT, partial differential equations are replaced by integral equations. The integrals are then approximated on finite volumes or cells. Assuming linear interpolation of the integrand, a mean value is approximated by the value of the integrand in the center of the cells or its edges.

EFIT is an efficient numerical approach to study wave propagation in homogeneous, strongly heterogeneous, isotropic, and anisotropic linear and nonlinear elastic media (Peiffer et. al 1997). Thus EFIT is an ideal method to study ultrasonic waves in concrete. This method also allows for flexibility in handling various boundary conditions. Simplicity is another advantage of the EFIT; it can be implemented easily and efficiently on various computer platforms. In the Cartesian coordinate system, velocity-stress finite-difference formulation with a staggered grid (Virieux 1984 and 1986), which is widely used to study earthquake motions, results in exactly the same equations as EFIT. For these reasons, EFIT was utilized for this simulation program.

Since MIRA is sending horizontal shear waves, EFIT is used to obtain the discretized equations of motion for this case. The following equation shows how velocity is related to shear stresses is this method:

$$v_y^{n+1}(i,j) = v_y^n(i,j) + \frac{\Delta t}{\rho}\left(\frac{\tau_{xy}^{n+\frac{1}{2}}(i,j) - \tau_{xy}^{n+\frac{1}{2}}(i,j-1)}{\Delta x} + \frac{\tau_{zy}^{n+\frac{1}{2}}(i,j) - \tau_{zy}^{n+\frac{1}{2}}(i-1,j)}{\Delta z}\right) \tag{13}$$

and shear stresses are determined using the following two equations:

$$v_y^{n+1}(i,j) = v_y^n(i,j) + \frac{\Delta t}{\rho}\left(\frac{\tau_{xy}^{n+\frac{1}{2}}(i,j) - \tau_{xy}^{n+\frac{1}{2}}(i,j-1)}{\Delta x} + \frac{\tau_{zy}^{n+\frac{1}{2}}(i,j) - \tau_{zy}^{n+\frac{1}{2}}(i-1,j)}{\Delta z}\right) \tag{14}$$

$$\tau_{zy}^{n+3/2}(i,j) = \tau_{zy}^{n+1/2}(i,j) + \frac{\mu\Delta t}{\Delta z}\left(v_y^{n+1}(i+1,j) - v_y^{n+1}(i,j)\right) \tag{15}$$

Where $v^k(i,j)$ and $\tau^k(i,j)$ stand for velocity and stress at time $t = k\Delta t$ and at a point with coordinates $x = i\Delta x$ and $z = j\Delta z$. These equations serve as the basis for the implementation of EFIT. Further execution and discussion of these EFIT methods and equations will be discussed in Chapter 6.

2.4 Improvements to Current Technology

The technologies and analysis techniques outlined in the previous sections show promise for applications regarding damage detection in concrete. Recent technological advancements have improved efficiency and allowed for in-situ applications in the last several years via the improvements created by SAFT reconstructions. However, these methods have their limitations when applied to damaged concrete sections and remain highly subjective. Moreover, when concrete is extensively damaged, many of the

principles incorporated into these methods are no longer applicable. It is these shortcomings that are addressed via the research presented in the following chapters.

CHAPTER 3: EARTHQUAKE DAMAGE

[This chapter is adapted from the following publication: Freeseman, K., Khazanovich, L., Hoegh, K., Nojavan, A., Schultz, A. E., Chao, S. (2016). Nondestructive monitoring of subsurface damage progression in concrete columns damaged by earthquake loading. *Engineering Structures*, Volume 114, 1 May 2016, 148-157.]

The assessment of the structural integrity of infrastructure after extreme events is an important application of nondestructive technology. Advancements in elastic wave-based methods in recent years have allowed for productive and accurate quantitative analysis which was previously lacking. In this study, ultrasonic array measurements coupled with a modified signature analysis method were implemented for damage detection purposes. Full-scale testing of a reinforced concrete column subjected to simulated earthquake loading was tested using ultrasound nondestructive testing at various stages of loading. A signature analysis technique was adapted to create improved reconstructions and was coupled with a quantitative analysis incorporating Pearson's correlation coefficient. The results demonstrated the ability to detect internal damages and defects prior to appearance on the surface using one-sided access, showing promise for health monitoring applications.

3.1 Introduction

The scale of damage caused by earthquakes has been well documented and portrayed in the media in recent history. While earthquakes can cause severe damage to buildings,

there are also cases where there may be no visible damage but the structure has been weakened as a result of the earthquake. Identifying both visible and nonvisible signs of earthquake damage is extremely important in the aftermath of a quake in order to categorize the condition and serviceability of remaining infrastructure. This scenario creates the need for nondestructive evaluation in order to assess the safety and remaining structural capacity. Specifically, reinforced concrete (RC) systems create added complexity due to their heterogeneous nature.

Extensive research has been done in the past regarding the response of RC structures to earthquake loading (e.g. Park and Ang 1985, Takeda et al. 1970, Bracci et al. 1997, and Ghee et al. 1989), which shows that damage in concrete structures may occur even under small drifts. Effective repair methods for damaged RC structural members have been developed, as verified by recent RC bridge columns tested using ground motion similar to that of the 1994 Northridge earthquake (Vosooghi and Saiidi 2013). However, for proper implementation of repair techniques, it is critical for damage to first be accurately identified, preferably by a nondestructive method.

Often, structural evaluation can only be conducted using nondestructive techniques that require access to only one side of the structure. Donnelly (2012) outlined the accuracy of many nondestructive techniques via the analysis of bridge decks, of which infrared thermography (IT) and impact echo (IE) proved to be the most successful. IT is able to identify less than half of the delaminations present and is highly affected by the depth of the delamination. IE is a common nondestructive testing method that involves generation of compression, shear, and Rayleigh waves using a mechanical

impact at the surface. The waves reflected from internal changes in acoustic impedance or external boundaries are recorded on the surface, where the impact was generated to give information about the structure using signal interpretation techniques normally based on spectral analysis. IE has been shown to be effective in detecting layer interfaces for applications such as thickness determination and inclusion detection. However, testing with this method can be time-intensive and only allows for one signal pair to be sent and received per scan. This lack of signal redundancy associated with a single impact signal causes difficulties when complex geometries are present due to the requirements of the spectral analysis method (Carino 2001). In addition, IE is able to detect top and bottom delaminations, but is not able to detect all cases of damage and in some instances results in false positives. When applied to concrete slabs, IE also proves to be sensitive to the overall dimension and thickness of the slab (Azari et al. 2014).

Shear wave based ultrasound methods have also been tested for crack detection in uniform concrete elements (Godinho et al. 2013). This research also identified the effect of rebar, aggregates, or damaged concrete as a complicating factor that needs to be addressed. Shubert and Kohler also found that the presence of aggregate and air voids creates scattering and attenuation of ultrasound signals (Schubert and Koehler 2001). Additionally, one-sided nondestructive ultrasound techniques have had difficulty in detecting damage behind dense reinforcement in concrete structures (Choi and Popovics 2015).

These methods are able to detect some cases of damage, but the limitations of their applicability highlight the need for a more quantitative nondestructive testing

method, especially for thick reinforced concrete elements with one-sided access. To this end, evaluation techniques and hardware such as air coupled impact echo have multiple measurement pairs and allow for more productive measurement acquisition (Popovics et al. 2012). Highly productive and repeatable measurements are needed to ensure measurement accuracy. To attain this reliability, dry point contact transducers have also been utilized. Dry point contact transducers allow for diagnostics up to 36 in. (914 mm) deep. This device uses low frequency (~50 kHz) stress waves to assess various types of structural systems, including reinforced concrete members (Choi and Popovics 2015).

While this high productivity allows for more reliable measurements, the analysis methods involved often require qualitative interpretation. To provide quantitative interpretation, Impact Echo Signature Analysis (IESA) has been proposed. IESA compares one-dimensional (1D) impact-echo signals with a reference signal in either the time or frequency domain. For time domain analysis, Pearson's correlation equation has been used for comparison of 1D impact-echo signals and is shown in Equation 16 (Schubert and Koehler 2008):

$$C_{XY}^{j} = \frac{Cov[X, Y^{j}]}{\sqrt{Var[X]Var[Y^{j}]}} = \frac{\sum_{i=1}^{N}(x_i - x_{mean})(y_i^{j} - y_{mean}^{j})}{\sum_{i=1}^{N}(x_i - x_{mean})^2 \sum_{i=1}^{N}(y_i^{j} - y_{mean}^{j})^2} \quad (16)$$

Where j is the j-th signal, i is the i-th value within a signal, X and Y_j are the intensity amplitude vectors of the reference and j-th IE scans, respectively; Cov and Var stand for the covariance and variance; x_i is the i-th intensity value within the reference signal and y_i is the i-th intensity value within the current signal, respectively; x_{mean} and y^j_{mean} are the

mean intensity of the reference signal and current signal, respectively; N is the number of intensity values in each signal being compared; and C^{j}_{XY} is Pearson's correlation coefficient, which measures the strength of the linear dependence between IE intensity measurements X and Y_j. Thus, no correlation would result in a C^{j}_{XY} value of 0, while a linear relationship between signals would have a C^{j}_{XY} value of 1.0. This quantification of similarity via referencing a signal representative of a "damage-free" position allows for qualitative analysis. The implementation of array technology further improves the nondestructive testing previously outlined by incorporating redundancy and measurement accuracy (Schubert et al. 2003).

The IESA method was generalized for two-dimensional reconstructions to allow for use with ultrasonic linear array technology. The resulting two-dimensional ultrasound tomography signature analysis (2D-UTSA) method has been applied for identification of plain concrete degradation under the surface (Hoegh et al. 2012).

This paper presents a modification of the 2D-UTSA method in order to monitor damage progression of a heavily reinforced concrete member and applied for evaluation of full-scale reinforced concrete moment frame columns that were tested by extreme earthquake loading protocols. These tests are part of a research project sponsored by George E. Brown, Jr. Network for Earthquake Engineering Simulation (NEES) of the National Science Foundation (NSF). Details of this experimental investigation have been reported by Nojavan et al. (2015).

Preliminary findings on the nondestructive evaluation of a reinforced concrete column are presented. In collaboration with the University of Texas at Arlington,

columns were tested at the University of Minnesota's Multi-Axial Subassemblage Testing (MAST) Laboratory under simulated earthquake loading. This provided an opportunity to gain insight on the internal behavior of the system before external damage was present through nondestructive evaluation.

3.2 Experimental Investigation

Full-scale reinforced concrete (RC) columns were constructed and tested under distinct earthquake loading protocols. These specimens were cast at the University of Texas at Arlington and tested at the Multi-Axial Sub-assemblage Testing (MAST) lab at the University of Minnesota. The columns are representative of a portion of a column bent in double-curvature at the ground floor of a 20-story modern high-rise moment frame building. The specimens had a clear height of 106 in. (2693 mm) between the footing (bottom) and the loading (top) blocks, and were designed in accordance with Chapter 21 of ACI 318-11 (ACI 2011). A Perimeter-Frame (PF) column was utilized for the nondestructive ultrasonic array testing described in this paper and had (16) #9 longitudinal bars with a cross-sectional dimension of 36x28 in. (914x711 mm). The column represents a ground level column of a 20-story perimeter moment frame used in modern RC buildings with interior post-tensioned flat slab system. Longitudinal bars were tied with #5 hoops and ties placed at 5 in. (127 mm) spacing. Figure 6 shows the reinforcement details and the dimensions of the columns.

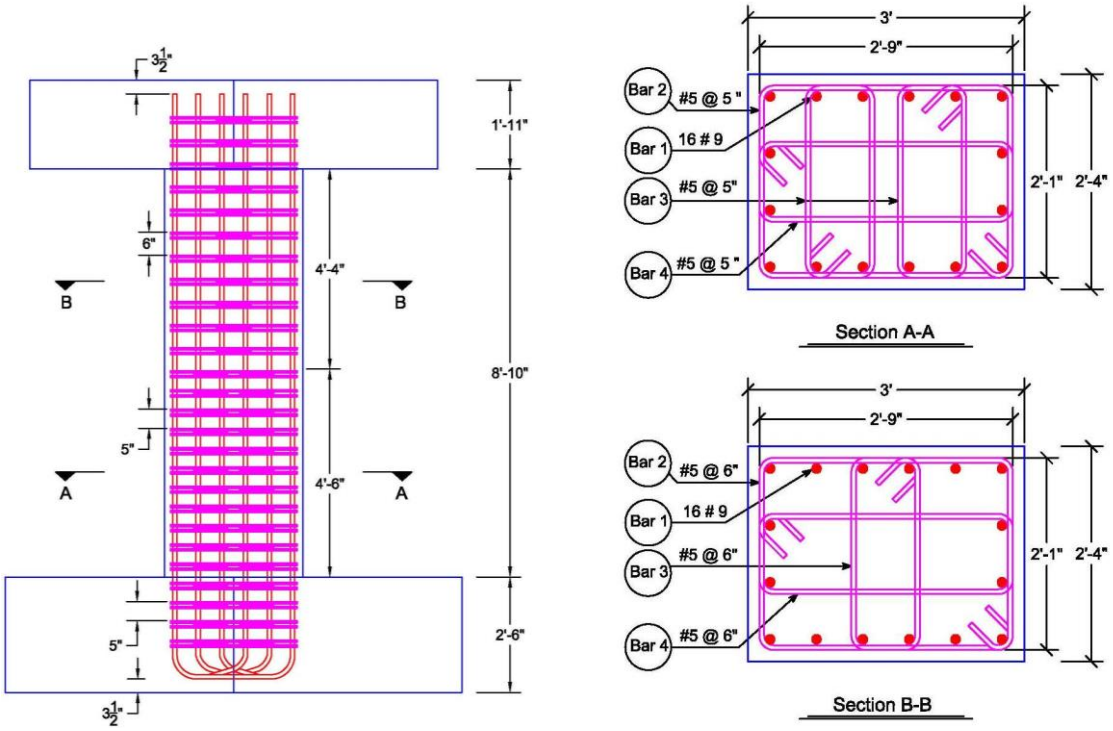

Figure 6. Column specimen assembly and detailing.

3.2.1 Instrumentation and Loading

The specimens were instrumented to measure deflection, rotation, and strains. Linear variable differential transformers (LVDTs) were installed vertically on opposite faces of the specimen in order to measure curvature along the height of the column. Horizontal LVDTs were also used to measure horizontal deflections. String potentiometers were installed to measure transverse displacement and shear deformations. In addition, strain gages were used to measure longitudinal and transverse steel and concrete core strains at locations along the columns. The specimen was placed on top of a three-piece spacer block and connected to the MAST strong floor and the loading crosshead (Figure 7). The columns were then loaded to simulate earthquake activity via a drift history

representative of multiple cycles of reversed motion with increasing amplitude. Figure 8 shows the near-collapse loading protocol in terms of the column drift ratios, while Figure 9 shows the lateral load vs. drift ratio hysteresis loops where drift ratio is defined as the lateral displacement at the inflection point of the column (96 in. (2438mm) above the column base) divided by the distance from the column base to the inflection point (96 in., 2438 mm). Testing was truncated once the strength of the column was reduced to 20% of its maximum capacity, as determined by the reduction in peak lateral load resisted by the system in a given cycle. Further details regarding experimental program can be found elsewhere (Nojava et al. 2015, Nojavan et al. 2014).

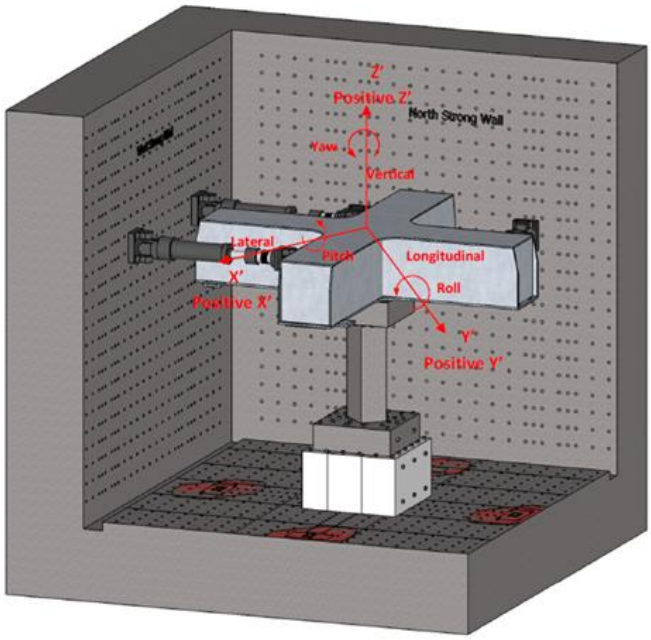

Figure 7. Assembly of the specimen under the loading crosshead at the MAST Lab (Nojavan et al. 2015).

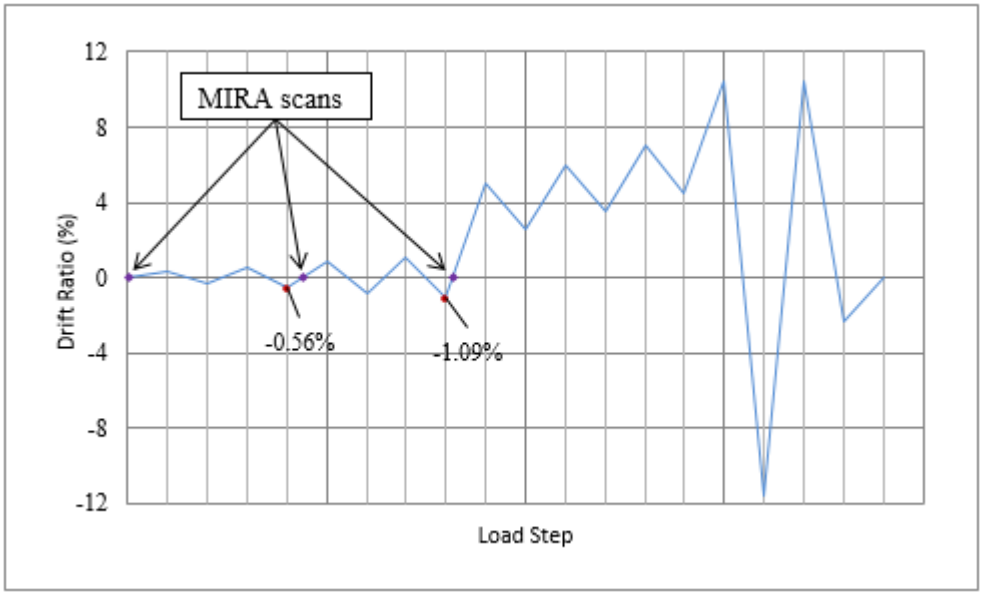

Figure 8. Near-collapse loading protocol in terms of column drift ratios (MIRA scans were conducted at the points shown after returning from the labelled peak drift locations).

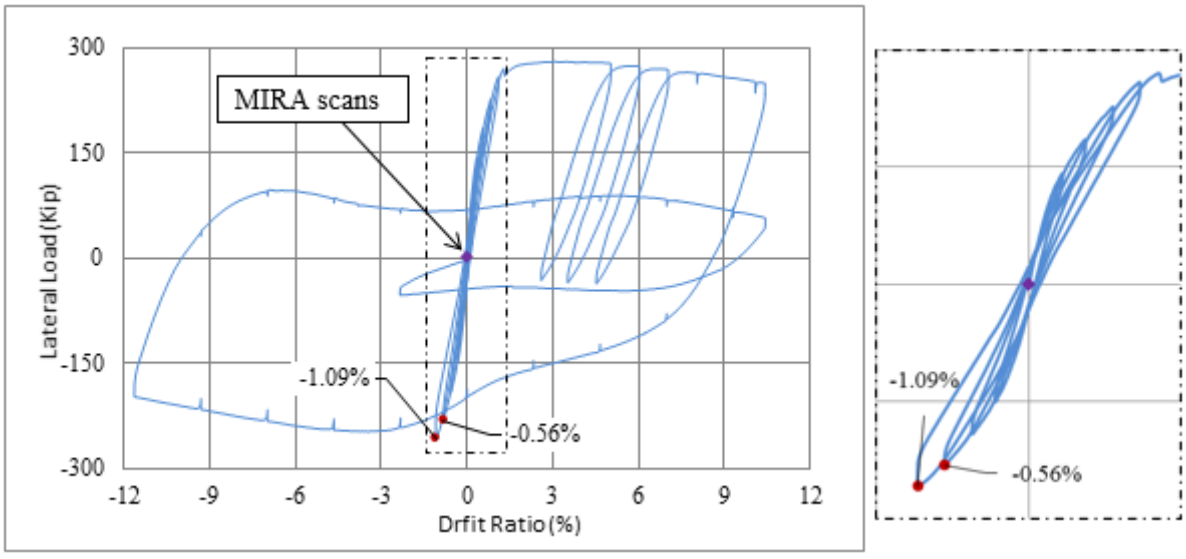

Figure 9. (left) Lateral load vs. drift ratio response and (right) enlarged cycles of interest (MIRA scans were conducted at the points shown after returning from the labelled peak drift locations).

3.2.2 Nondestructive Testing

While the specimen was being tested for earthquake loading, scans were obtained

incrementally using the ultrasonic tomography device MIRA (Shevaldykin et al. 2002).

MIRA incorporates 10 channels, with each channel composed of four transmitting and receiving transducers, as seen in Figure 10. This linear array allows for 45 time-of-flight measurements in less than three seconds. The change in acoustic impedance causes reflection of the waves traveling from one medium to another (i.e. from concrete to rebar or concrete to air). The recorded wave reflections at the surface from the transducers are processed using the Synthetic Aperture Focusing Technique (SAFT, discussed later) to yield a visual representation of the cross section that was measured. The results can then be analyzed to help gain insight into the inner structure (Hoegh et al. 2012, Hoegh et al. 2013, Hoegh and Khazanovich 2012). For example, pavement applications have shown the device to be capable of detecting inclusions and internal flaws (Hoegh et al. 2012, Hoegh et al. 2013, Hoegh and Khazanovich 2012, Hoegh et al. 2011).

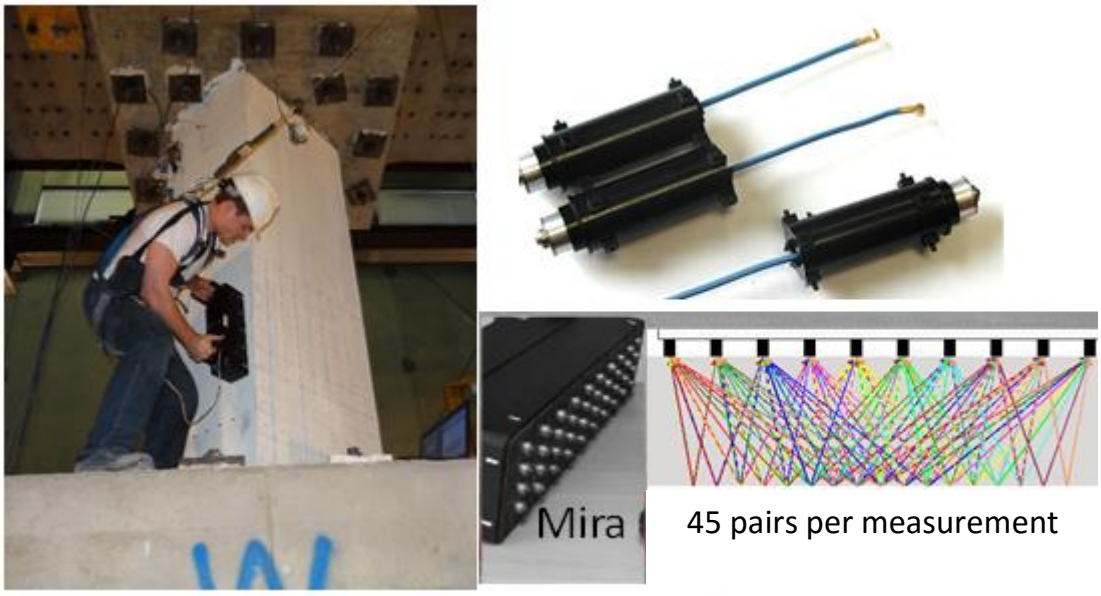

Figure 10. MIRA ultrasonic linear array device

In this study, ultrasonic array measurements were taken at three discrete times during testing in which the column was brought back to its neutral position (zero drift)

for safety reasons. Measurements were taken prior to any loading, once zero drift was attained after loading resulting in 0.5% drift level, and after achieving 1% drift level. These drift levels were selected based upon the observed damage progression of previous rounds of testing. The loading corresponding to these locations was detailed in Figure 8 and Figure 9, with dots designating when testing took place and the point of maximum drift achieved prior to measurement acquisition. A total of 60 ultrasound readings were taken, organized in sets of 6 progressing from left to right with approximately 4 in. (102 mm) between sequential readings. This spacing resulted in 12 in. (305 mm) of overlap from scan to scan due to the 16 in. (406 mm) width of the testing device. Figure 11 shows the state of the column when the 2nd set of measurements was taken, while Figure 12 shows the condition of the column when the 3rd set of measurements was taken. As can be seen in the first set of images, there were no external signs of damage when the 2nd set of measurements was taken, but the 3rd set of measurements were taken when external damage was present.

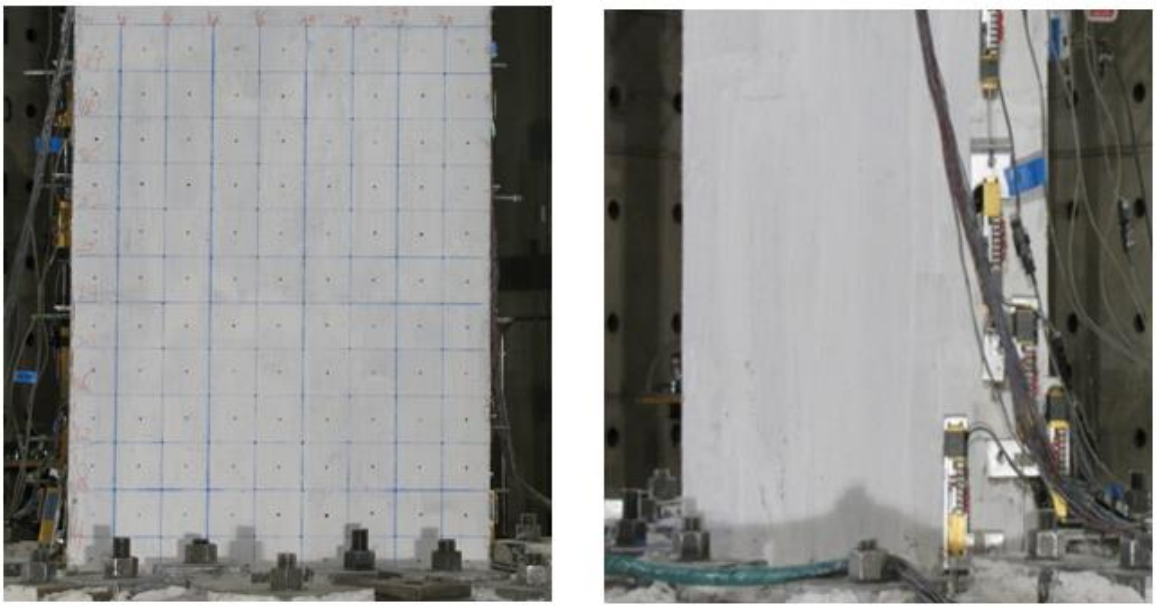

Figure 11. Column condition for 2nd set of MIRA measurements (after 0.5% drift ratio was attained).

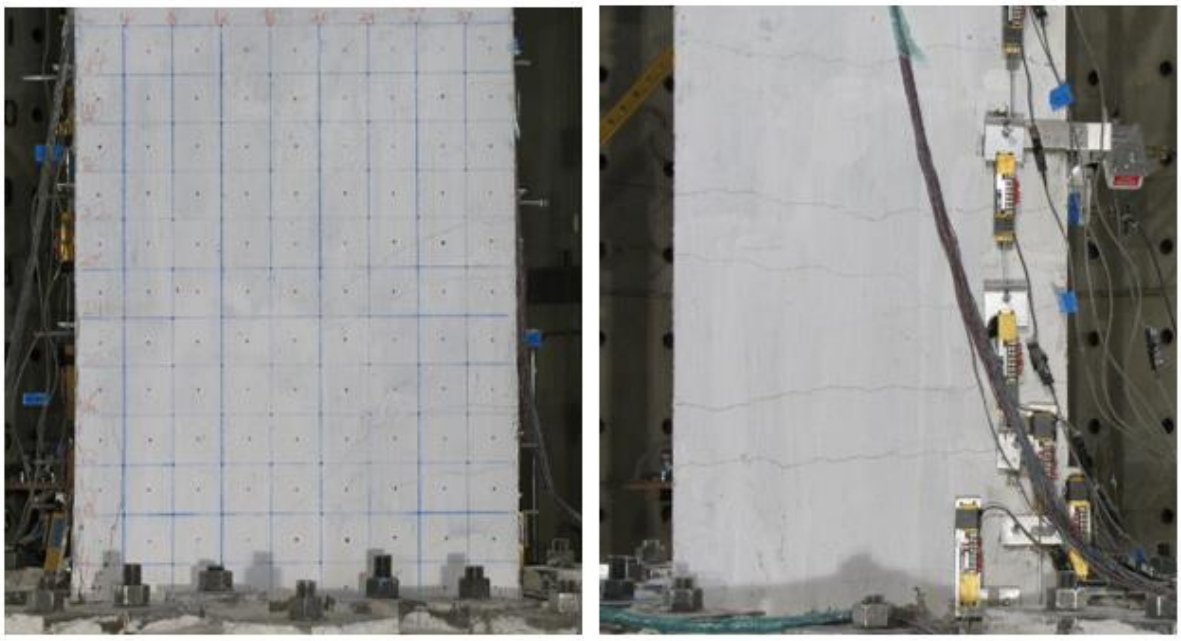

Figure 12. Column condition for 3rd set of MIRA measurements (after 1% drift ratio was attained).

3.3 Analytical investigation

A signature quantitative analysis method was utilized to collect data at different damage levels. SAFT is an ultrasonic imaging technique that allows for back-propagating of a set of impulse time-histories to achieve reconstructions with improved resolution. In addition, this technique allows for improvements in signal to noise by reducing the backscattering effects of the concrete material through the natural deconvolution characteristics of the algorithm (Langenberg et al. 2012). The following equation allows for the formulation of reconstructed images at a point via integration.

$$\widehat{\boldsymbol{o}}(x,z) = \int_{x'_{min}}^{x'_{max}} \alpha\left(x', x, z\right) s\left(x', \frac{2}{c}\sqrt{z^2 + (x\text{-}x')^2}\right) dx' \tag{17}$$

where α(x',x,z) is the apodization factor that is typically a function of the distance traveled, divergence of the wave propagation, and incident angle of reflecting interface at each reflection point location with respect to the emitted/received signal (Lingvall et al. 2003), x'min and x'max are the interval in which the signals are measured, c is the sound velocity, x and z are the horizontal and vertical positions in the region of interest (ROI), x' is the transducer location, and *s* is the received impulse.

3.3.1 Qualitative Analysis

SAFT reconstructions at pre-loading, after 0.5% drift ratio, and after 1% drift ratio are shown in Figure 13 and Figure 14. Figure 13 shows an example of readings that indicate little change in relative reflectivity, while Figure 14 shows an example location that exhibits a large change in relative reflectivity. Lighter (white) areas correspond to areas of high reflectivity, indicating the presence of changes in acoustic impedance. For example, presence of reinforcement, flaws, or layer boundaries cause an increase in

reflectivity. In this case, the lighter regions were roughly 2 in. (51 mm) deep and are representative of the #5 transverse bars. These figures show only the first 12 in. (305 mm) due to the limited accuracy at large depths of individual scans. In order to address this and other limitations, as well as utilize the overlapping scans that were captured during data collection, panoramic images were of interest.

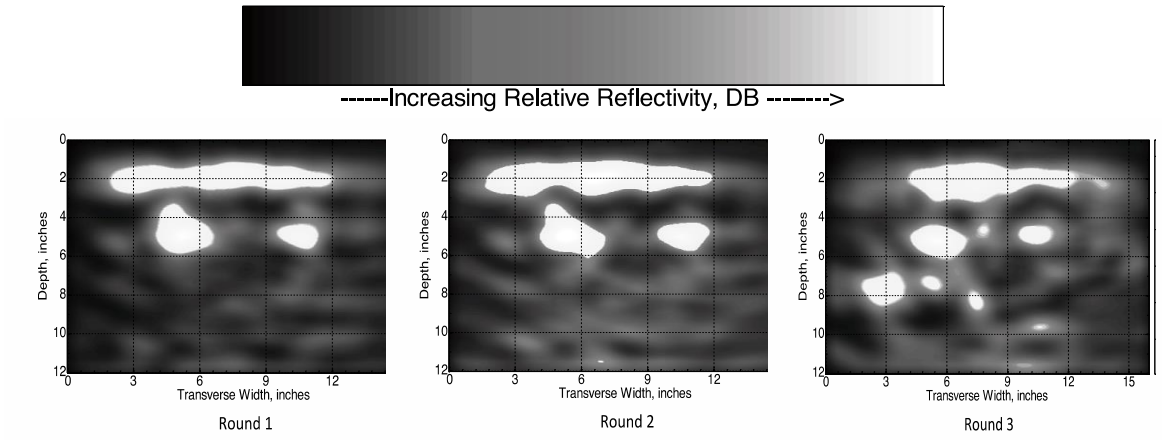

Figure 13. MIRA Reconstructions for 1st round (left) and 2nd round (middle), and 3rd round (right) for a location with relatively low level of damage with loading.

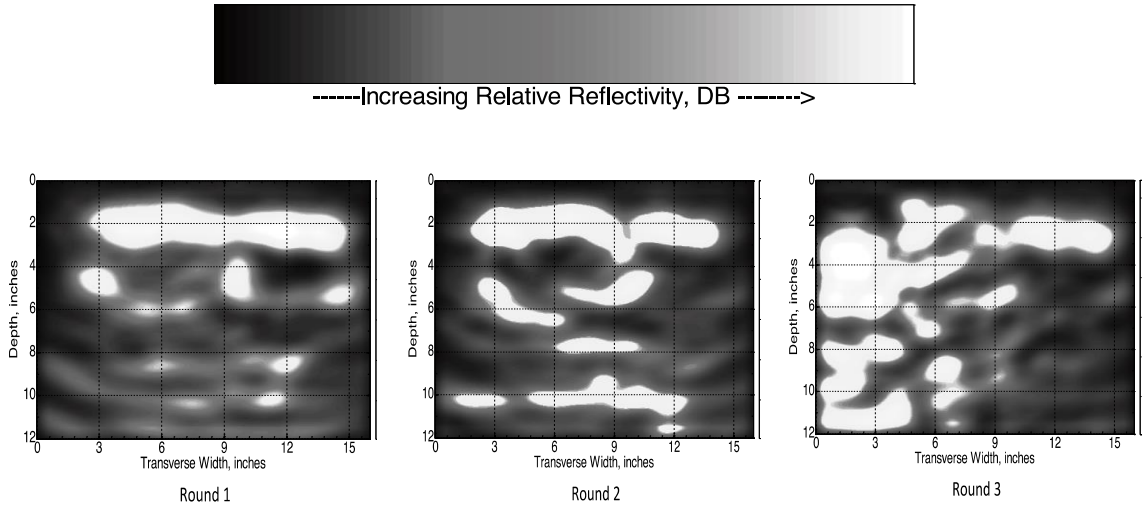

Figure 14. MIRA Reconstructions for 1st round (left) and 2nd round (middle), and 3rd round (right) for a location with relatively high level of damage with loading.

Because there is limited coverage at the edges of individual scans due to the presence of fewer overlapping transducers, panoramic reconstructions allow for a more accurate and redundant form of analysis. This also mitigates the limited aperture effect, allowing for quantitative comparisons of relative reflectivity within a wider region of SAFT panoramic reconstructions (Hoegh and Khazanovich 2015). Because the region of interest (the entire cross-section of the column) is larger than the individual SAFT reconstructions, multiple sets of reconstructions can be combined to add redundancy and create a large panoramic cross-section with high resolution. To achieve this, individual scans are combined in a string formation in which each SAFT scan overlaps with the next to create an encompassing region of interest, or ROI_{PAN}. For those regions in which the SAFT scans overlap one another, the larger value is selected for the panoramic image.

To formulate these panoramic images, each SAFT scan, $\widehat{\boldsymbol{O}}_I^m$, where m is the index of the current SAFT scan and I denotes that it is an individual scan, is combined in the following manner to form the new ROI_{PAN}. The ROI_{PAN}^m has the same vertical dimension, z, as all of the individual SAFT scans, while the horizontal dimension spans from 0 to x_{PAN}^m. Each individual scan has a horizontal dimension of x_I^m. In this case, ROI_{PAN} has a width of 36 in. (914 mm) and a depth of 30 in. (762 mm), while individual SAFT scans had a width of only 16 in. (406 mm). SAFT scans are merged, with each individual SAFT scan starting a distance D from the global origin (0, 0). The SAFT scans, $\widehat{\boldsymbol{O}}_{x,z}^m$, are combined according to the following expression for all values of x and z:

$$\widehat{\boldsymbol{O}}_{PAN}^{m}(x,z)=\begin{cases}\widehat{\boldsymbol{O}}_{PAN}^{m-1}(x,z), & if\ x<D\\ \max\left(\widehat{\boldsymbol{O}}_{PAN}^{m-1}(x,z),\widehat{\boldsymbol{O}}_{I}^{m}\ (\mathrm{x,z})\right), & \text{if D}<\mathrm{x}<x_{PAN}^{m-1}\\ \widehat{\boldsymbol{O}}_{I}^{m}\ (\mathrm{x,z}), & if\ x>x_{I}^{m}\end{cases} \tag{18}$$

For each panoramic reconstruction in this study, six individual SAFT scans were merged, as shown in the schematic in Figure 15. The first SAFT scan covers surface areas A-D, the second scan covers areas B-E, and so on with the sixth SAFT scan covering the areas F-I.

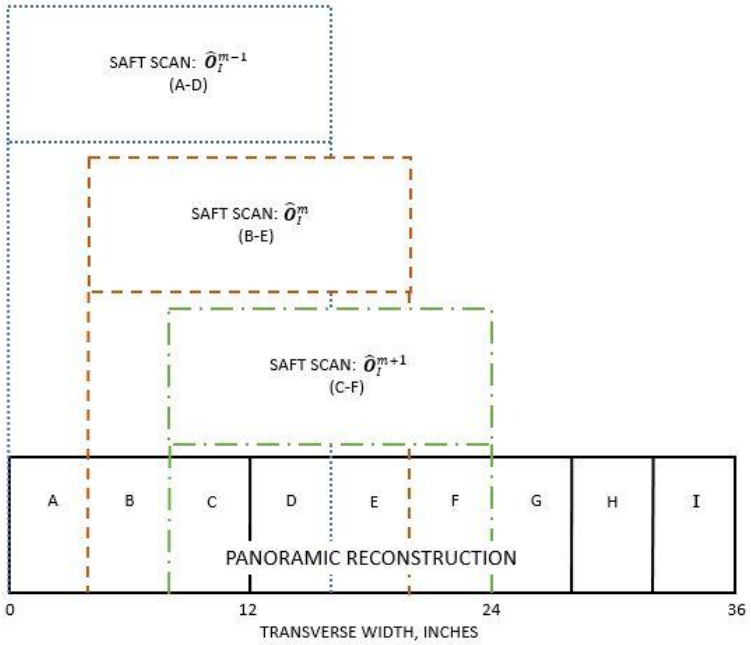

Figure 15. Schematic outlining the merging of 6 individual SAFT scans to create one panoramic reconstruction.

Figure 16 gives an illustrative example cross-section comparing the ultrasound panoramic reconstruction to the designed features along the width of the column at a height of 9 in. (229 mm) from the base. Figure 16(a) shows the example panoramic created using Equation 18 at that location. Figure 16(b) shows the corresponding designed cross-section. It can be observed that increases in reflectivity occur at the

shallower reinforcement locations, as well as the depth of the column along the evaluated cross-section. Even though there is significant attenuation of the wavefront at 28 in. of depth, the change in acoustic impedance at the layer boundary from concrete to air is significant enough to show up in the reconstruction. This is only true if there is not significant enough damage to cause additional scattering of the wavefront. Figure 16 shows the location of the #9 reinforcing bars, as well as the presence of the backwall.

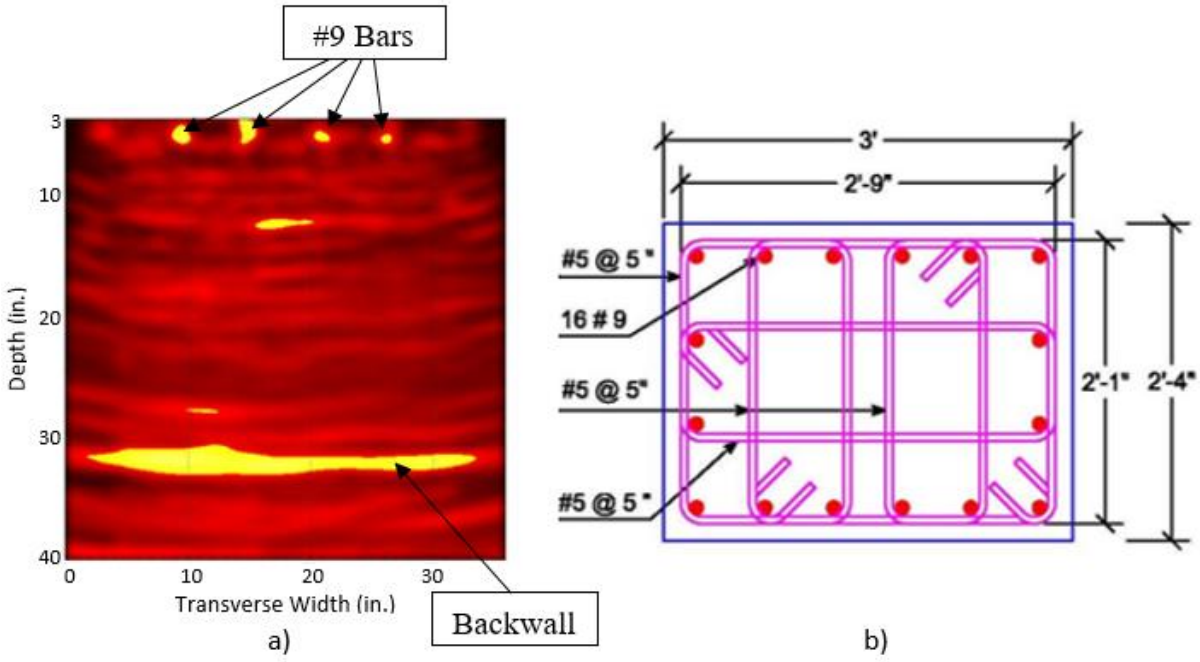

Figure 16. (a) Panoramic reconstructions for 1st measurement showing location of reinforcement and back wall presence, and (b) corresponding design schematic.

A series of panoramic reconstructions can be seen in Figure 17**.** This figure shows the scans for all three rounds of testing at a location near the base of the column, highlighting the damage progression and subsequent shadowing of the backwall captured by the scans. It can be observed from Figure 16(a) that the backwall reflection is strong for the evaluated width of the reconstruction indicating no significant damage. Scattering,

referring to any deviation in wave propagation from that which is expected for a homogenous body, can be used as an indicator of the damage level. The backwall on the left side of the reconstruction is not present after the 2nd round of loading, indicating increased scattering of the wavefront toward the left. The backwall is not present after the 3rd round of testing, indicating significant scattering of the wavefront. The increase in scattering (shadowing of the wavefront) indicates the presence of increased damage at a shallower depth (Schickert et al. 2003). However, since this analysis is qualitative in nature, signature analysis is presented in the following section to quantify the damage caused by loading.

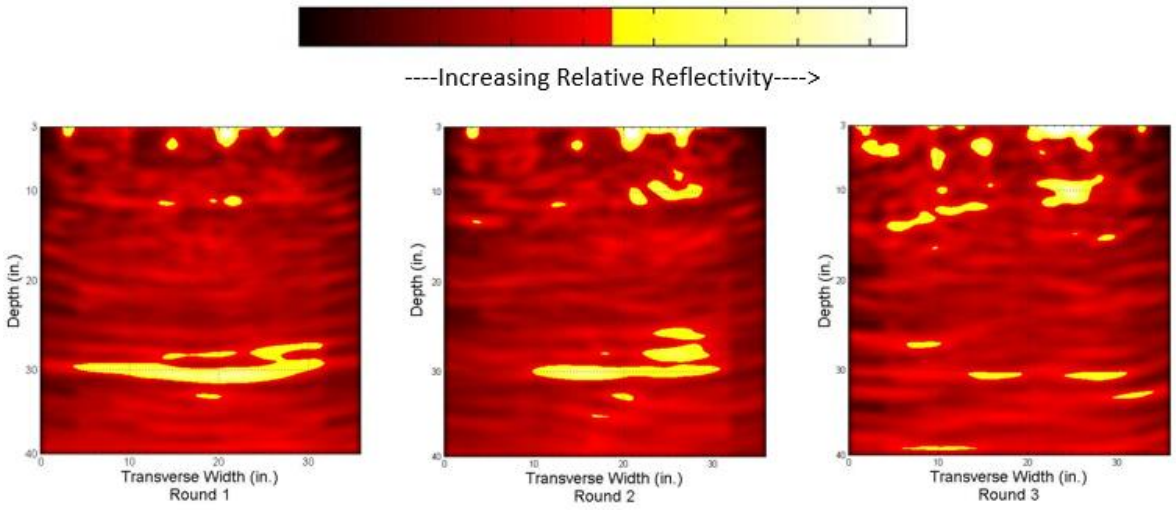

Figure 17. Panoramic reconstructions for 1st measurement (left), 2nd measurement (middle), and 3rd measurement (right) for a location on the bottom of the column.

3.3.2 Quantitative Analysis

While this change in reflectivity can be qualitatively observed via panoramic images, and indicates increased damage of the concrete around the reinforcement as shown in Figure 10, these types of interpretations require significant engineering judgment and time.

Because of this, an ultrasonic tomography signature analysis (2D-UTSA) method has been adapted to quantify the level of damage by comparing each scan to the corresponding undamaged condition. It has been shown in previous studies that Pearson's correlation is a good indicator of linear dependence, and thus damage, in comparing IE and ultrasound measurements (Schubert and Koehler 2008, Hoegh and Khazanovich 2012). Pearson's correlation coefficient is adapted for comparison of reconstructed intensity matrices from testing conducted before and after loading as follows using the SAFT variables shown below in Equation 19:

$$C^{IA,m} = \frac{Cov\left[\left[\widehat{\boldsymbol{o}}\right]^{IA,ref},\left[\widehat{\boldsymbol{o}}\right]^{IA,m}\right]}{\sqrt{Var\left[\left[\widehat{\boldsymbol{o}}\right]^{IA,ref}\right]Var\left[\left[\widehat{\boldsymbol{o}}\right]^{IA,m}\right]}} = \frac{\sum_{i=1}^{W}\sum_{k=1}^{D}\left(\hat{\boldsymbol{o}}_{i,k}^{IA,ref} - \hat{\boldsymbol{o}}_{mean}^{IA,ref}\right)\left(\hat{\boldsymbol{o}}_{i,k}^{IA,m} - \hat{\boldsymbol{o}}_{mean}^{IA,m}\right)}{\sum_{i=1}^{W}\sum_{k=1}^{D}\left(\hat{\boldsymbol{o}}_{i,k}^{IA,ref} - \hat{\boldsymbol{o}}_{mean}^{IA,ref}\right)^2 \sum_{i=1}^{W}\sum_{k=1}^{D}\left(\hat{\boldsymbol{o}}_{i,k}^{IA} - \hat{\boldsymbol{o}}_{mean}^{IA}\right)^2} \quad (19)$$

where $\left[\widehat{\boldsymbol{O}}\right]^{IA,ref}$ and $\left[\widehat{\boldsymbol{O}}\right]^{IA,m}$ are the matrices of reflection intensity for the reference SAFT scan for the preloading condition and SAFT scan taken after loading and damage occurred, respectively; $\widehat{\boldsymbol{o}}_{i,k}^{IA,ref}$ and $\widehat{\boldsymbol{o}}_{i,k}^{IA}$ are the single intensity values of the reference signal and damaged reconstruction, respectively, with depth increasing with k and the horizontal location of the scan increasing with i; $\widehat{\boldsymbol{o}}_{mean}^{IA,ref}$ and $\widehat{\boldsymbol{o}}_{mean}^{IA}$ are the mean intensities of the reference scan and damaged scan, respectively; W and D are the number of width and depth intensity values in the depth and device aperture direction, respectively; and $C^{IA,m}$ is Pearson's correlation coefficient, which measures the strength of the linear dependence between $\left[\widehat{\boldsymbol{O}}\right]^{IA,ref}$ and $\left[\widehat{\boldsymbol{O}}\right]^{IA,m}$.

In this study, the unloaded scan condition was used as the reference scan (i.e. the left image in Figure 16). This quantitative analysis method makes the technique more feasible for routine implementation due to the reduced interpretation time. Thus, flawed concrete locations can be identified due to the similar scan locations of the reference and damaged scan conditions. On the extremes, a $C^{IA,m}$ value of 0 would indicate no correlation and a $C^{IA,m}$ value of 1.0 would indicate that the two SAFT scans are related linearly. Therefore, a higher $C^{IA,m}$ would indicate that the SAFT scan was taken on sound concrete, and a significant decrease in the correlation coefficient would indicate non-uniform SAFT scans, or damaged concrete, especially if observed in a group of adjacent scans. This type of analysis will be referred to as the 2D-UTSA method. Lower UTSA values indicate an increase in damage as compared to the original condition.

To demonstrate the ability of UTSA values to characterize damage, consider an example analysis using a reconstruction from round 1 experimental data serving as a clean condition, and a scan containing random noise, as shown below in Figure 18.

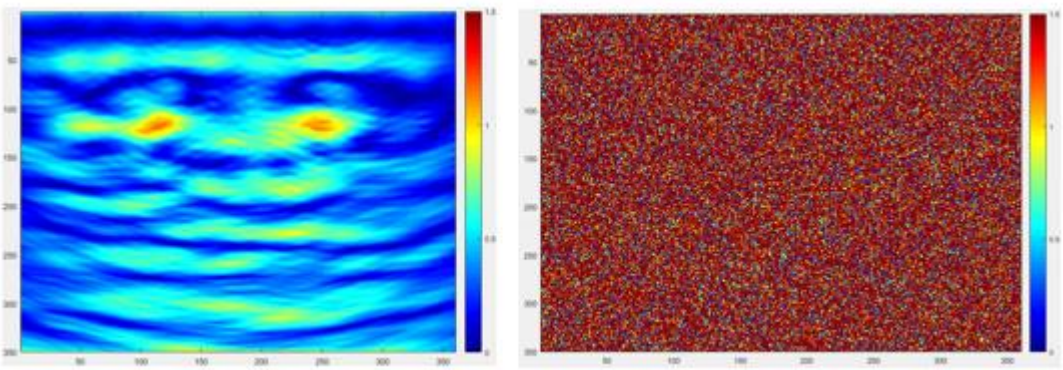

Figure 18. Experimental reconstruction from round 1 of testing (left), and fabricated reconstruction containing noise (right).

Multiple artificial reconstructions can be generated as detailed in Equation 20:

$$[\hat{O}]_i = [\hat{O}]^{IA,ref} + \alpha_i [\hat{O}]^{IA,noise} \quad (20)$$

where $[\hat{O}]_i$ is the new matrix, $[\hat{O}]^{IA,ref}$ is the reference matrix of reflection intensity for the clean case, as shown in Figure 13 (left), $[\hat{O}]^{IA,noise}$ is the matrix of reflection intensity containing random noise, as shown in Figure 13 (right), α is the coefficient of noise intensity for all i cases considered for analysis. If the coefficient α is small, the reconstruction should be similar to the original reference reconstruction, while an increase in α leads to an increase in noise that is often associated with damage.

A sample analysis was performed in which α values of 0.01, 0.05, 0.1, and 0.25 were used to create artificial reconstructions. Each of these artificial matrices were compared with the reference case (Figure 18, left) and Pearson's correlation coefficients were computed using Equation 19. The effect of these α values on the resulting Pearson's correlation coefficient is shown in Figure 19. It can be observed that for very small α values, the Pearson's correlation coefficient approaches one, while increasing α leads to very low correlation.

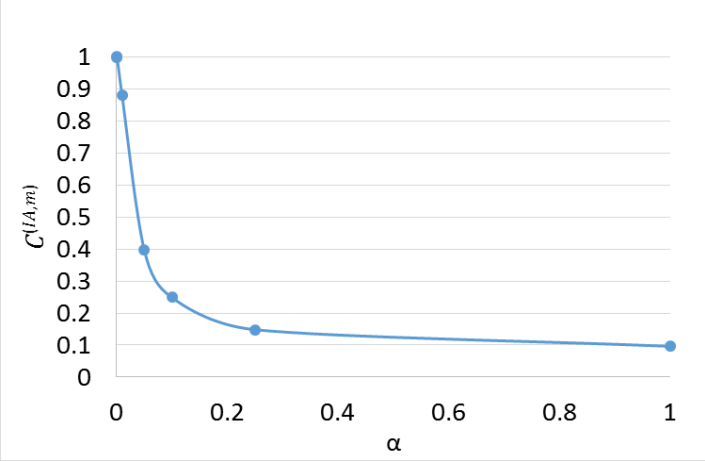

Figure 19. Effect of changes in α on the Pearson's correlation coefficient value.

This analysis can be confirmed by visual comparison of the corresponding reconstructions shown in Figure 20. As can be seen, reconstructions with high Pearson's correlation coefficient values appeared similar to the reference case, whereas reconstructions with low values show significant deviation from the base case. This same principal holds for the analysis of subsequent rounds of experimental data, and the results of this analysis are shown in the following section.

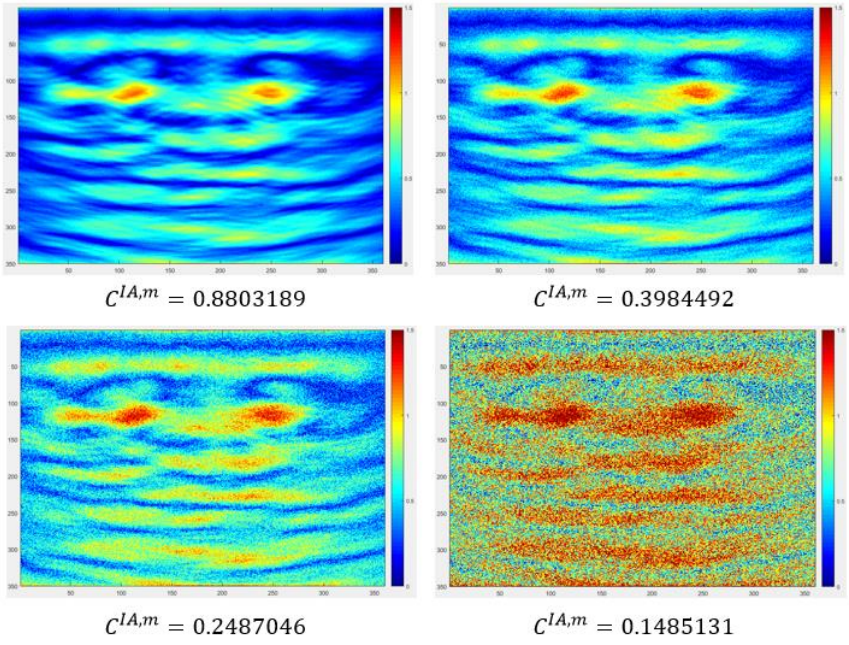

Figure 20. Reconstruction for α of 0.01 (top left), 0.05 (top right), 0.1 (bottom left), and 0.25 (bottom right).

3.4 Experimental Results and Discussion

The analysis presented in this study is based on analysis of shear horizontal waves (SH waves) where a portion travels along the surface and a portion reflects from within the medium. Since the 50 kHz shear waves correspond to a wavelength of approximately 2 inches (51 mm), the reconstructions of the first two inches below the surface need to

account for both wave paths. Below this point, the surface path of the signal can be ignored. Because damage detection below the surface is of interest in this study, the surface path is not included in this analysis

Figure 21 and Figure 22 show a representation of the 2D-UTSA results comparing the original panoramic scans to those after 0.5% and 1% drift ratios, respectively. For each tested location, the $C^{IA,m}$ value was plotted on a scale with 0 indicated by dark shading and 1 indicated by white, with intermediate values shown in lighter shading. In this case, darker locations (lower $C^{IA,m}$ values) indicate an increase in subsurface damage from the original condition, while light locations (higher $C^{IA,m}$ values) indicate little change from the original condition. As can be seen from these figures, ultrasonic array testing can identify levels of degradation before there are external signs of failure. When analyzing these two figures, a general trend of higher damage intensity (dark coloring) can be seen in the left and lower left portion of the images. This area corresponds to the portion of the column that exhibited external damage first, as seen in Figure 12.

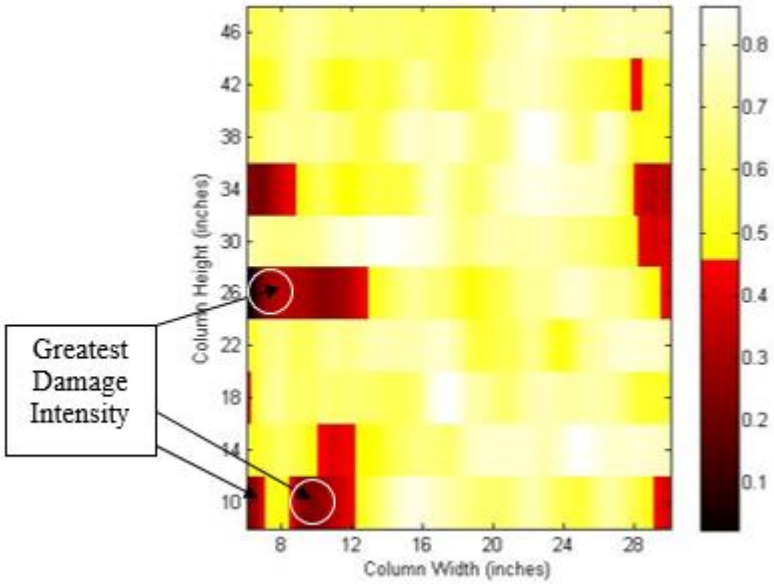

Figure 21. MIRA gradient results after 0.5% drift ratio.

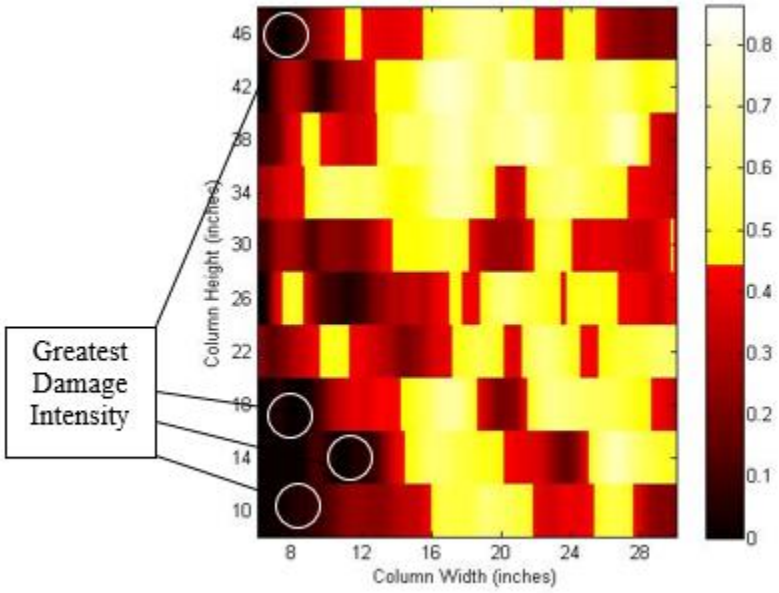

Figure 22. MIRA gradient results after 1% drift ratio.

3.5 Conclusions

Advancements in elastic wave methods have allowed for productive and accurate quantitative analysis which was previously lacking. In this study, ultrasonic array measurements coupled with a modified signature analysis method were implemented.

The full-scale testing of a heavily reinforced concrete column subjected to simulated earthquake loading demonstrated the ability to detect internal damages and defects prior to appearance on the surface using one-sided access. This meets an important infrastructure health monitoring goal of identifying damage development beneath the surface nondestructively before visual failure occurs. Shadowing analysis of the ultrasonic imaging reconstructions indicated damage below the surface caused by scattering of the ultrasonic wavefronts. The shadowing and other indicators of damage were quantified through the use of correlation coefficient signature analysis. The results of signature analysis showed increased subsurface damage in the areas that failed first after further loading. This demonstrates the ability of ultrasonic array testing and signature analysis to aid in detecting not only damage below the surface, but also to indicate which area of the column will show signs of failure first. It should be noted that the current analysis presented in this chapter requires measurements of the undamaged state of the specimen to evaluate the relative damage progression. As such, the techniques can be employed in actual cases if monitoring of structural health begins before damage has occurred. Further work will be done in the future by the authors, in fusion with alternative nondestructive testing methods, to increase the applicability of the current findings for implementation on structures which have not been analyzed in an undamaged state.

The applicability of ultrasonic methods presented in this paper is promising in the field of health monitoring due to its nondestructive nature and its ability to detect issues that are not visible on the surface at the time of testing. This type of subsurface

characterization provides a practical input for improved assessment of the safety and remaining service life of structures since the methods presented in this paper require only one-sided access for data collection and provide quantitative early detection of subsurface conditions.

CHAPTER 4: EARLY AGE DAMAGE

The second phase of the experimental investigation of load-induced damage involved the assessment of early age damage in concrete. The premise of the experiments described in this chapter involved the simulation of early opening to traffic on concrete pavements. This was achieved via the pouring of a large sample of concrete test beams in the laboratory. The incremental loading of these small flexure beams (6 x 6 x 24 inches) was performed in an attempt to create early age damage within the beams, and subsequent nondestructive testing was performed for damage detection purposes.

4.1 Laboratory Beam Iterations

Four total rounds of laboratory beam tests were performed; a summary of the rounds of testing is shown in Table 1. All rounds of testing incorporated shear wave velocity measurements throughout the first 28 days, though differences in curing and loading conditions were incorporated. The first round of beams incorporated air curing conditions and static short-term loads. Beams were loaded to 80% of ultimate strength at early ages ranging from day 1 to day 7, with all beams being broken via standard ASTM flexural testing (C78) on day 28. The beam loading protocol for Round 1 can be seen in Table 2.

Table 1. Laboratory testing summary

Round	Date	Number of Specimens	Curing Condition	Loading Protocol
1	4/1/14	20 beams	Air Curing	Beams were loaded to 80% of the Day 1 strength
2	7/14/14	22 beams	Water Curing	Beams were loaded to 80% of the Day 1 strength
3	8/25/14	25 beams	Water Curing	Beams were loaded to 80% of the strength on loading day- loading increased each day

4	3/2/15	12 beams	Curing Compound	Beams were loaded cyclically from 65-80% of the strength on the day of loading- loading increased each day to reflect strength gain

Table 2. Round 1 loading summary

Beam	Day 1	Day 2	Day 3	Day 7	Day 28
101	Load to 80% of beam 119 Strength				
102		Load to 80% of beam 119	Load to 80% of beam 119	Load to 80% of beam 119	**Break**
103					
104		Load to 80% of beam 119 Strength	Load to 80% of beam 119 Strength	Load to 80% of beam 119 Strength	**Break to Determine 28 Day Strength**
105					
106					
107					
108					
109					
110					
111					
112					
113					
114					
115					
116	Extra Beam				
117	Extra Beam				
118	Load to 80% of beam 119	Load to 80% of beam 119	Load to 80% of beam 119	Load to 80% of beam 119	**Break**
119	**Break to Determine Day 1 Strength**				
120	Extra Beam				

Analysis of the preliminary results from round 1 showed trends indicating that beams which had been loaded at early ages had lower ultimate strengths than those that were never loaded, as shown in Figure 23. The results of this first round of testing

seemed to indicate that the beams which were loaded at early ages were damaged sufficiently to affect ultimate strength.

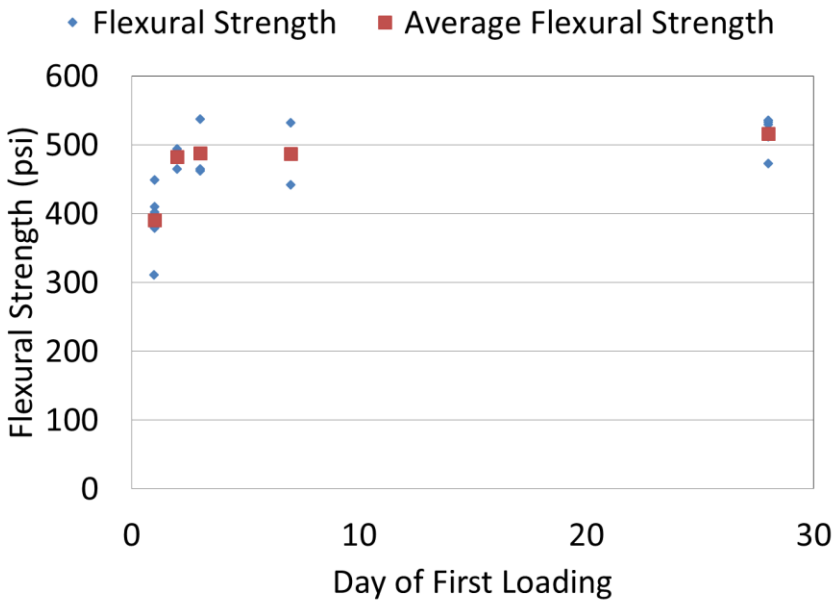

Figure 23. Ultimate strength vs. day of first loading for round 1.

In an attempt to validate these results, a second round of testing was performed utilizing water curing conditions, attained via submersion in a curing tank, and the same loading scenarios as the first round. The loading summary for round 2 is shown in Table 3. Inconclusive results were seen, so a third round of testing was performed as detailed in Table 4. For this iteration, loading was increased with time to account for the strength gain achieved due to water curing.

Table 3. Round 2 loading summary

<table>
<tr><th>Beam</th><th>Day 1</th><th>Day 2</th><th>Day 3</th><th>Day 7</th><th>Day 28</th></tr>
<tr><td>201</td><td rowspan="3">Load to 80% of beams 220-222 Avg. Strength</td><td rowspan="6">Load to 80% of beams 220-222 Average Strength</td><td rowspan="9">Load to 80% of beams 220-222 Average Strength</td><td rowspan="12">Load to 80% of beams 220-222 Average Strength</td><td rowspan="14">Break for 28 Day Strength</td></tr>
<tr><td>202</td></tr>
<tr><td>203</td></tr>
<tr><td>204</td><td></td></tr>
<tr><td>205</td><td></td></tr>
<tr><td>206</td><td></td></tr>
<tr><td>207</td><td></td><td></td></tr>
<tr><td>208</td><td></td><td></td></tr>
<tr><td>209</td><td></td><td></td></tr>
<tr><td>210</td><td></td><td></td><td></td></tr>
<tr><td>211</td><td></td><td></td><td></td></tr>
<tr><td>212</td><td></td><td></td><td></td></tr>
<tr><td>213</td><td></td><td></td><td></td><td></td></tr>
<tr><td>214</td><td></td><td></td><td></td><td></td></tr>
<tr><td>215</td><td></td><td></td><td></td><td></td></tr>
<tr><td>216</td><td></td><td></td><td></td><td rowspan="2">Break to Determine Day 7 Strength</td><td></td></tr>
<tr><td>217</td><td></td><td></td><td></td><td></td></tr>
<tr><td>218</td><td></td><td rowspan="2">Break to Determine Day 2 Strength</td><td></td><td></td><td></td></tr>
<tr><td>219</td><td></td><td></td><td></td><td></td></tr>
<tr><td>220</td><td rowspan="3">Break to Determine Day 1 Strength</td><td></td><td></td><td></td><td></td></tr>
<tr><td>221</td><td></td><td></td><td></td><td></td></tr>
<tr><td>222</td><td></td><td></td><td></td><td></td></tr>
</table>

Table 4. Round 3 loading summary

Beam	Day 1	Day 2	Day 3	Day 7	Day 28
301	Load to 80% of beams 323-325 Avg. Strength	Load to 80% of beams 320-322 Avg. Strength	Load to 80% of beams 318-319 Avg. Strength	Load to 80% of beams 316-317 Avg. Strength	**Break for 28 Day Strength**
302					
303					
304					
305					
306					
307					
308					
309					
310					
311					
312					
313					
314					
315					
316				**Break to Determine Day 7 Strength**	
317					
318			**Break to Determine Day 3 Strength**		
319					
320		**Break to Determine Day 2 Strength**			
321					
322					
323	**Break to Determine Day 1 Strength**				
324					
325					

The flexural strength results for rounds 2 and 3 can be seen in Figure 24. Both rounds of testing provided inconclusive results, as early age loading appeared to have the opposite effect on ultimate strength that was seen for round 1. A final round of testing was thus deemed necessary. The loading protocol for this round of testing can be found in

Table 5. The variables which changed for this round of testing included curing condition and loading type. A curing compound was instead applied to the beams, and cyclic loading was implemented in an attempt to better simulate traffic loading on concrete pavements.

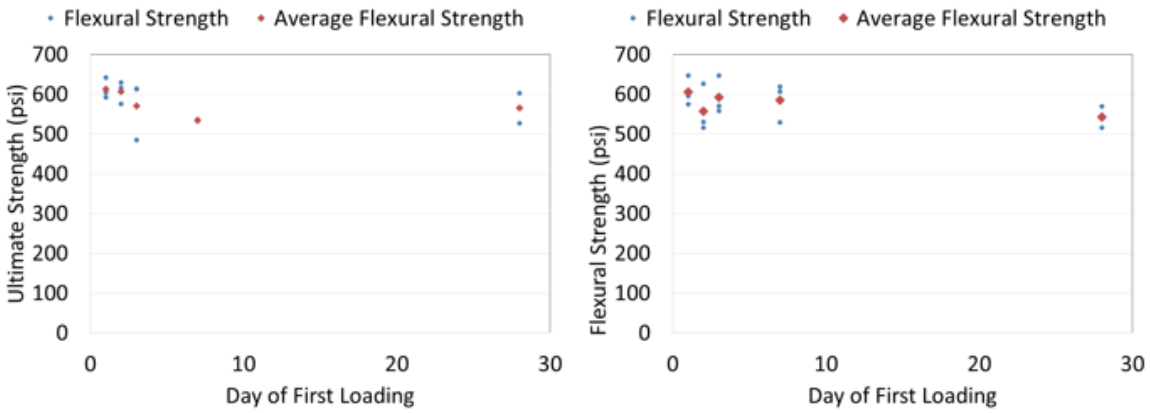

Figure 24. Ultimate strength vs. day of first loading for rounds 2 (left) and 3 (right).

Table 5. Round 4 loading summary

Beam	Day 1	Day 2	Day 3	Day 4	Day 7	Day 8	Day 14
401	Cyclic Load 65-80% of beam 407						
402		Cyclic Load 65-80% of beam 408					**Break for 14 Day Strength**
403			Cyclic Load 65-80% of beam 409				
404					Cyclic Load 65-80% of beam 410		
405				Cyclic Load 65-80% of beam 409			
406							
407	**Break**						
408		**Break**					
409			**Break**				
410					**Break**		
411							**Break**

The break strength results versus day of first loading for the fourth round of testing is shown in Figure 25. As can be seen, the results were again inconclusive and appeared to indicate that loading at early ages had no effect on ultimate strength.

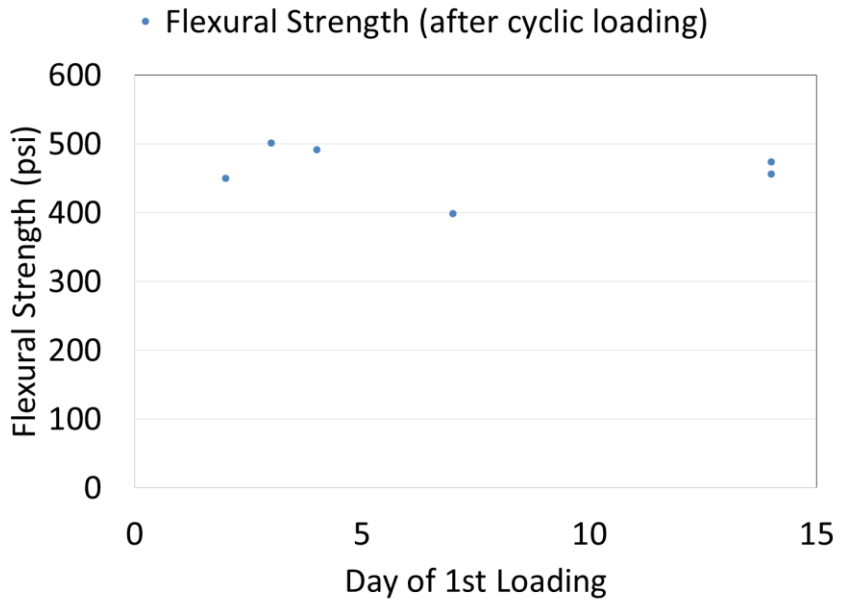

Figure 25. Ultimate strength vs. day of first loading for round 4.

The inconclusive results can be attributed to one, or a combination, of two justifications:

- The beams were not sufficiently damaged during early age loading
- The inherent variability associated with flexural strength testing does not allow for effects on ultimate strength to be seen (ASTM C78: Standard Test Method for Flexural Strength of Concrete allows for differences in flexural strength test results for the same mix to be up to 16% without concern of testing errors)

4.2 Nondestructive Analysis

In order to determine if the beams were actually damaged, the MIRA results were analyzed. Because of the effect of boundary conditions and edges on the reconstructions,

no valuable information can be obtained from this method due to the relatively small size of the beams. As such, shear wave velocity was instead analyzed. The shear wave velocity vs. time data for all rounds of testing provided conclusive results which showed that shear wave velocity increases with time, in a similar shape and trend to that of strength gain. The shear wave velocity curves for all four rounds of testing are shown in Figure 26.

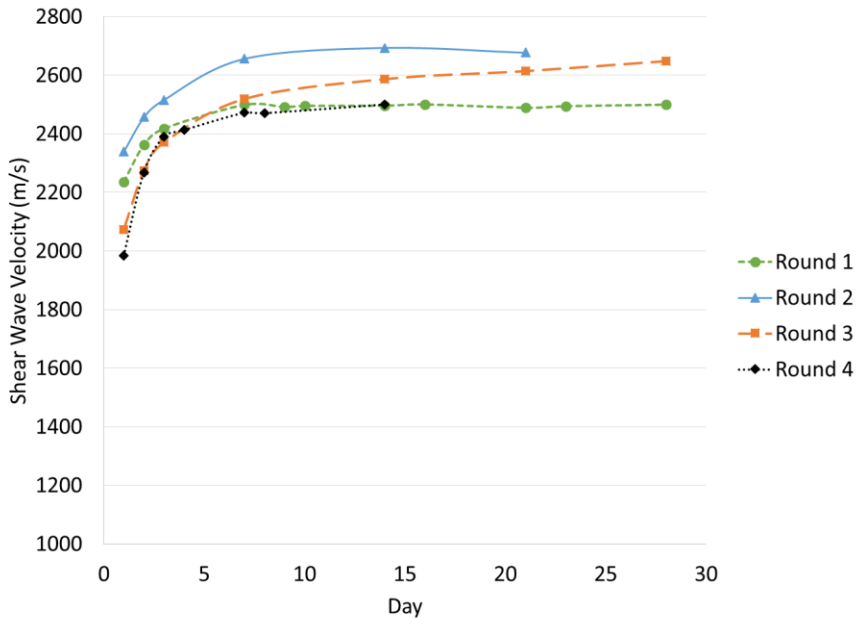

Figure 26. Shear wave velocity gain over time for all rounds of testing.

While the trends in shear wave velocity over time were apparent and showed promise for indirect correlation between strength gain and shear wave velocity gain, there were not conclusive results regarding measured shear wave velocity and break strength. Figure 27 shows this relationship for all four rounds of testing. As can be seen, there is a general positive trend between these two values, but the R^2 values show that shear wave

velocity cannot consistently or accurately reflect break strength. Furthermore, it was seen that shear wave velocities for beams which were loaded did not have consistent trends with respect to the unloaded beams (i.e. it would be expected that the beams which were loaded and experienced damage would have a lower shear wave velocity, which was not the case). As such, the measured shear wave velocities are either not capable of truly detecting damage, as shown by the variability in the obtained values, or the beams were not sufficiently damaged to affect shear wave velocity or ultimate strength.

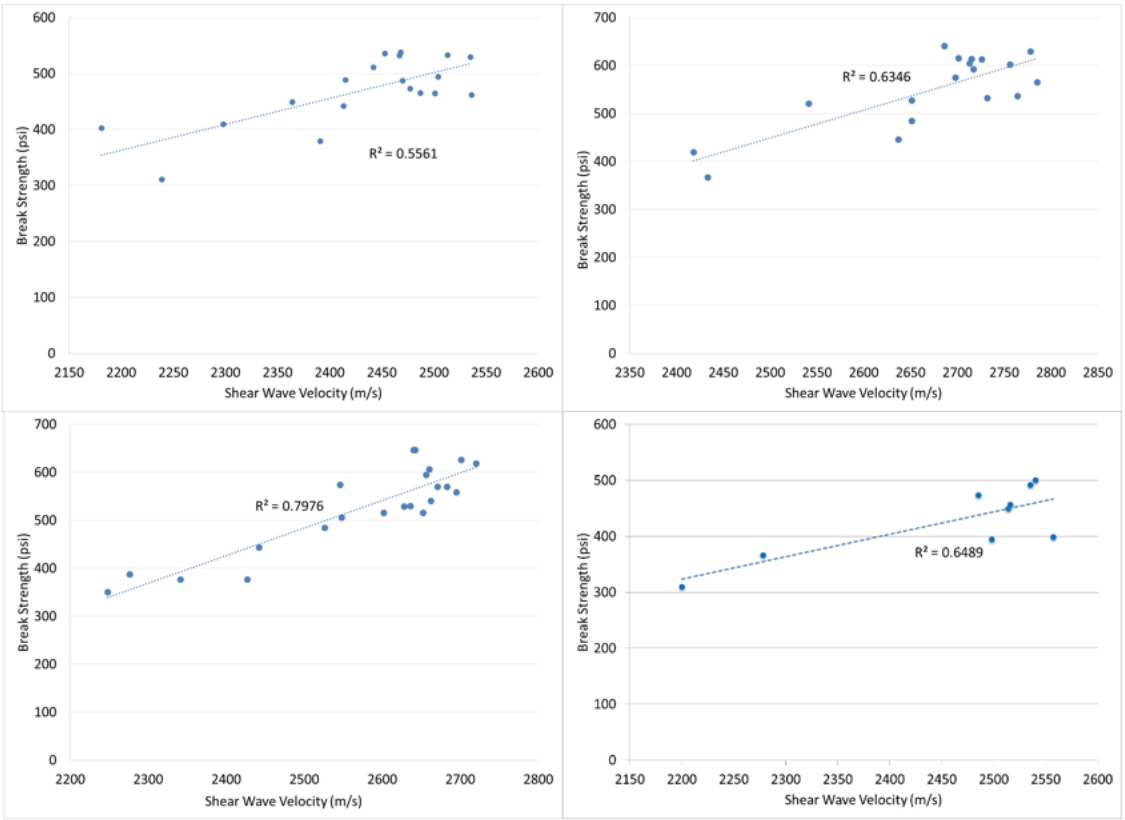

Figure 27. Shear wave velocity vs. break strength for round 1 (top left), round 2 (top right), round 3 (bottom left) and round 4 (bottom right).

4.3 Conclusions

While a multitude of data was gathered via these laboratory beam iterations, no conclusive damage detection findings resulted from the nondestructive testing efforts. However, the shear velocity gain over time data which was obtained was valuable in that it showed similar trends to that of strength gain. On the other hand, the lack of ability to nondestructively detect damage via measured values of shear wave velocity served as the motivation for the development of an indicator of damage, as described in the following chapters.

CHAPTER 5: ENVIRONMENTAL DAMAGE

Environmental damage, as defined by the research included here, includes damage which is caused by standard life-cycle degradation experienced by concrete pavements. The two types of damage investigated here are freeze-thaw and alkali-silica reaction (ASR) damage. Both types of damage are commonly experienced throughout multiple climates and regions across the country, though comprehensively successful methods for the mitigation of this type of damage have yet to be discovered. These two damage types are included in the same chapter due to the similarities in damage manifestations of freezing and thawing and ASR, exhibited by microcracking near the surface of the concrete. The analyses of these two types of environmental damage are described in the following sections. First, the damage detection methods which were implemented for both cases are described, followed by the implementation and results of those methods, broken down by damage type.

5.1 Damage Detection Methods

Two methods were employed for the detection of environmental damage. Those methods include a visual reconstruction analysis, as well as the development of a quantitative indicator of the concrete condition. The method utilized for the visual reconstructions has been discussed previously in both the literature review, and within the reinforced concrete column discussion found in Chapter 3. However, the basis of the visual analysis used for the environmental damage cases is comparative in nature for diagnosing each

individual reconstruction image based upon typical reconstruction characteristics. The methods used for the quantitative indicator analysis are presented here.

5.1.1 Quantitative Indicator Development

A visual investigation of raw signal data from both sound and damaged concrete slabs resulted in several key differences between the two slab conditions to be identified. To illustrate the differences between sound and damaged concrete with respect to the raw signal, two representative normalized signals are shown below in Figure 28. On the left is an example of a signal from a slab in good condition, while the signal on the right shows a signal which was obtained from a slab with damage present. The two key differences between these signals are the shape of the direct arrival impulse (highlighted earlier in the time history), and the increased oscillation which occurs after the direct arrival (highlighted later in the time history). The precise change in direct arrival signal shape is not consistent in all damaged slabs, however the shape is consistently different from the sound condition. In some cases, the signal appears to show a phase change (as shown in this example), which is exhibited by the inversion in signal shape. The increased oscillation occurs after the direct arrival, but this oscillation is not present in the sound concrete condition. These two qualitative differences in signal shape served as the basis for the development of a numerical indicator to diagnose the condition of concrete in a nondestructive manner.

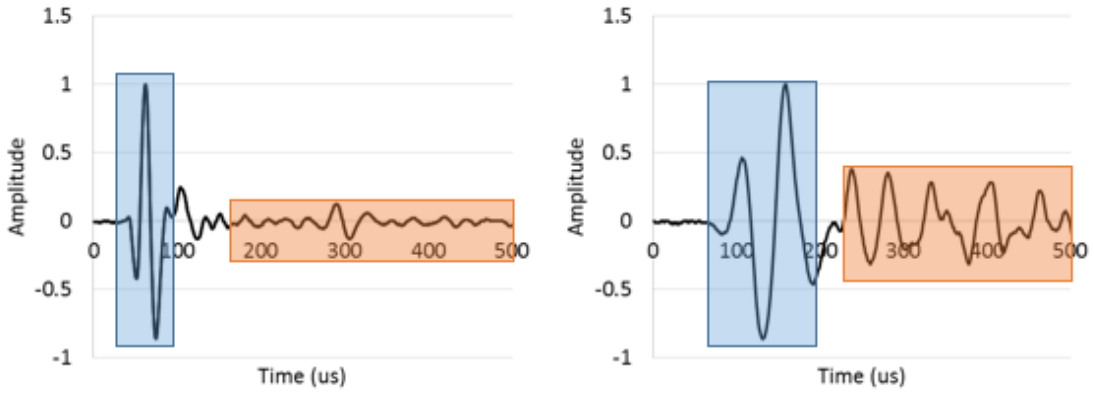

Figure 28. Sample normalized signals for clean concrete (left) and damaged concrete (right) highlighting key differences.

While the above signals have been normalized, it is worth discussing the trends in magnitude of the raw signals. A thorough visual inspection of an extensive data set of both clean and damaged signals revealed that the magnitude of the signal is not an indicator of the condition of the concrete. The magnitude or amplitude is instead dependent upon the contact conditions and pressure applied when using the device. To show the variability in magnitude within each condition level, consider the two graphs shown below in Figure 29. The first graph shows two signals from scans on sound concrete. The first signal has a maximum magnitude of 183, while the second example signal has a magnitude peak of 270. These signals were obtained from the same slab, seconds apart from each other, yet have considerably different magnitudes. The same observations can be made from the two signals obtained from a damaged concrete slab, as shown in the second graph. One signal has a magnitude of 173, while the other peaks at 268. Again, these signals were both obtained from the same slab, in the same time period. While the magnitudes vary greatly, the condition of the concrete remains the

same. As such, magnitude is not an indicator of the condition of concrete and has thus been removed from this analysis, as detailed in the development of the quantitative indicator.

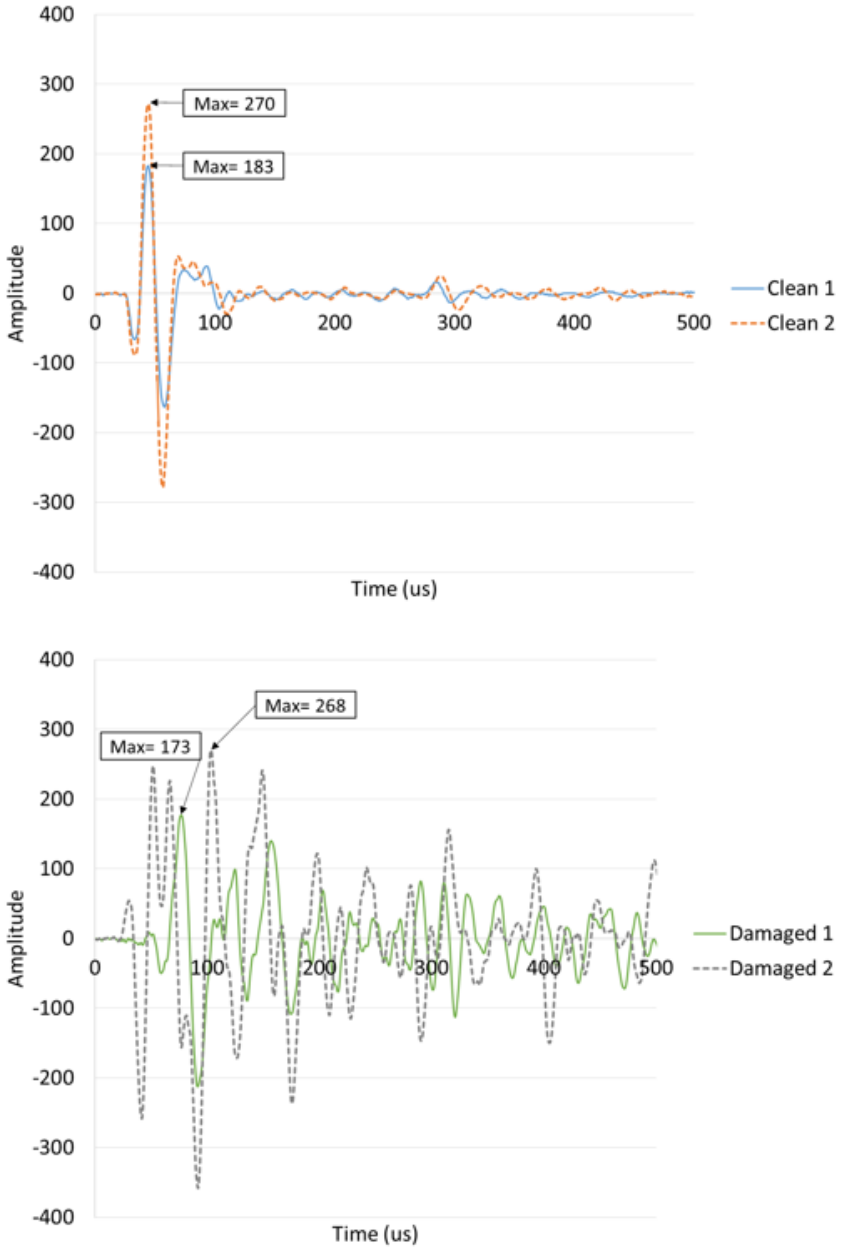

Figure 29. Example raw signals for two clean cases (top) and two damaged cases (bottom).

The numerical indicator which was developed is based upon the instantaneous amplitude envelope that is created using Hilbert transform. Hilbert transform is a common technique in signal data analysis, especially when interested instantaneous attributes of the signal. The Hilbert transform, HT(t) of a certain function, f(x), as calculated by Matlab is commonly defined as:

$$HT(t) = \sqrt{(f(t))^2 + \left(\frac{1}{\pi}\int_{-\infty}^{\infty} \frac{f(\tau)}{t-\tau} dx\right)^2} \tag{21}$$

To illustrate the output of this transformation, consider the example shown below. Shown via dashed line is the raw signal data, and the solid line is the resulting Hilbert transform envelope.

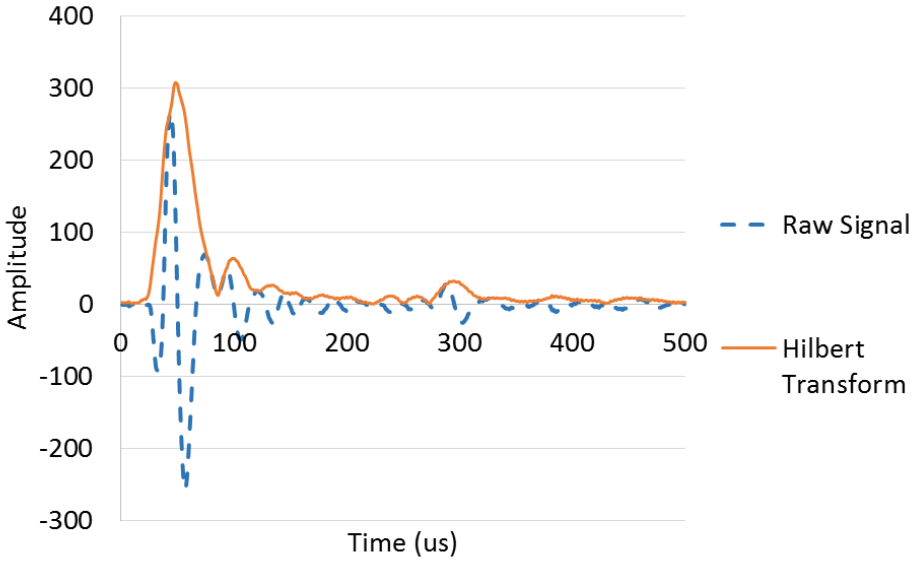

Figure 30. Sample Hilbert transform envelope.

This Hilbert transform envelope served as the basis for the creation of a numerical indicator which captured the increased oscillations which were present in the damaged

signal case. As such, the indicator must be greatly affected by the presence of these oscillations. The following indicator, referred to as the Hilbert Transform Indicator (HTI), was created:

$$HTI = \int_0^{500} \frac{HT(t)}{\max(HT(t))}\, dt \tag{22}$$

This equation considers a time frame of 500 microseconds, chosen in order to both capture the direct arrival impulse, as well as the subsequent oscillations which occur in the damaged case. The Hilbert transform envelope is normalized in order to remove any effect of magnitude on the results.

To illustrate the ability of the HTI in capturing the condition of the concrete, consider two example Hilbert transform envelopes which are graphed below. Shown in a solid line is the clean case, and in dotted line is the damaged case envelope. The HTI for the clean signal was 55, while the HTI for the damaged was 137. One can see the drastic changes in the Hilbert transform envelope for the damaged case, which result from the increased oscillations present. The HTI value captures this difference numerically, as exhibited by a value of over twice that of the clean case. The extensive data set which was analyzed allowed for the creation of typical numerical categories for the HTI values in order to classify the condition of the specimen. Typical HTI values for concrete in sound condition are below 90, usually in the 70s. HTI values for extensively damaged concrete are typically above 120. Those HTI values which fall in-between these categories are beginning to show signs of damage but do not show signs of heavy degradation. The discussion and analysis of HTI values for damaged slabs will be further discussed for each damage application in sections 5.2.3.2 and 5.3.4.

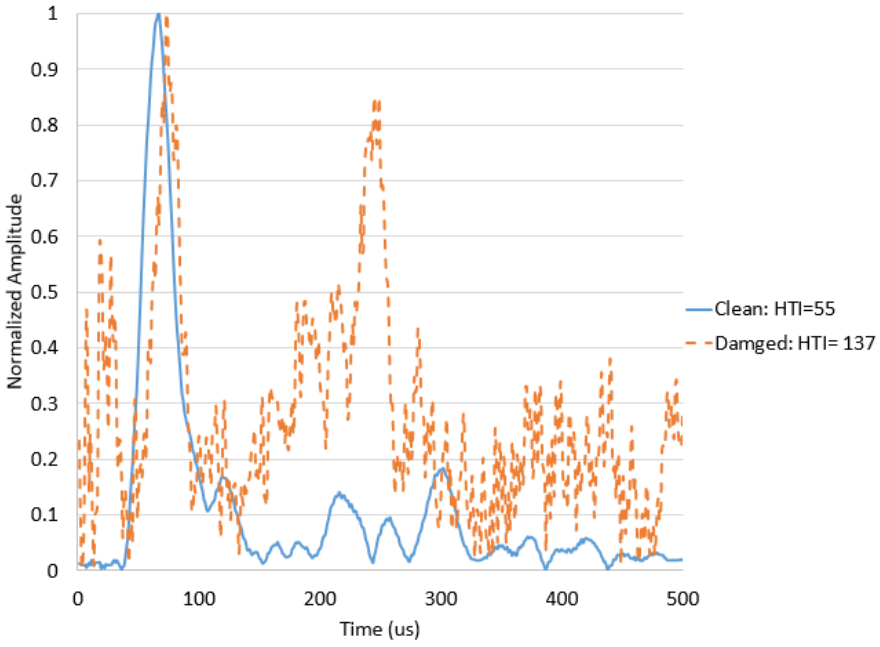

Figure 31. Typical Hilbert transform envelopes for sound and damaged specimens.

To show the repeatability of HTI values, a large data set compiled from past research efforts performed on sound concrete was analyzed, as mentioned above. 45 scans were analyzed, resulting in the calculation of over 2,000 HTI values. Statistical values for this data set are shown below in Table 6. It is also important to note that there are trends in HTI value within each scan. The HTI value increases in magnitude as transducer spacing increases, as would be expected due to greater noise associated with greater distances in wave travel. As such, it is useful to average the HTI values obtained from all 45 transducer pairs to result in one comprehensive indicator value which incorporates redundancy and results in increased measurement confidence. It is this averaged value that is shown in the table.

Table 6. Preliminary HTI values for sound concrete

Number of averaged HTI values	45
Average HTI Value	72.5
Standard Deviation	6.47

A confidence interval based upon the analysis of undamaged concrete signals can also be created, and is shown below in Figure 32. As can be seen, the HTI values increase significantly with transducer spacing, in a repeatable fashion. The 95% confidence interval is reasonable due to the low standard deviations seen. Again, these values are averaged in order to incorporate redundancy while also lessening the complexity of analysis required. This is justified due to the repeatability observed in this sample analysis.

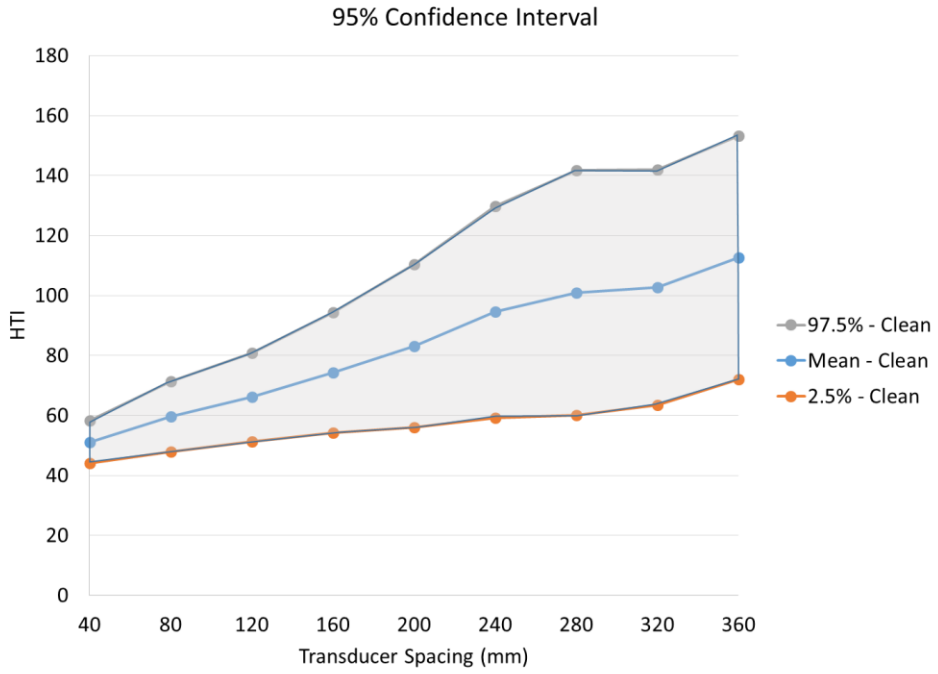

Figure 32. 95% confidence interval for sound concrete.

5.2 Freeze Thaw Damage

[This section is partially adapted from a submission to ASCE Journal of Infrastructure Systems, which is currently under review]

Freeze thaw damage in concrete structures is a serious issue for infrastructure in cold regions. Accurate detection of this type of damage at early stages allows for the selection of optimum strategies for preservation and rehabilitation activities. This section explores the feasibility of utilizing ultrasonic shear wave technology for quantification of damage in concrete slabs, which could be successfully applied for the detection of freeze thaw damage. Four slabs with varying levels of freeze thaw damage were tested and two analysis techniques were developed to characterize the damage present. These methods involve the formulation of reconstructions to analyze the subsurface condition, as well as the creation of a numerical index based upon recorded signal characteristics. The results of both analyses showed agreement both with each other and with the visual survey assessments. However, the methods were able to detect damage in portions of the slab where no visual cracks were observed. These techniques showed promise for an accurate nondestructive quantification of the extent of freeze thaw damage, or similar damage manifestations, in concrete structures.

5.2.1 Previous Methods

Freeze thaw damage in concrete structures continues to be a serious issue for infrastructure in regions which experience temperature swings below freezing (Korhonen 2002), creating the most persistent problems associated with deterioration to concrete infrastructure in cold weather climates (Tanesi and Meininger 2006). As such, significant

research effort has been devoted to this type of damage (Yang 2004, Farnam et al. 2014, Li et al. 2012, Hazaree et al. 2011, Eiras et al. 2015). Freeze thaw damage is caused by expansive pressures resulting from the freezing of excess water present in the concrete microstructure. As a result, microcracking ensues and eventually creates spalling and duress to the concrete system (Yang et al. 2006).

Resistance of concrete mix to freeze thaw damage can be measured via standardized tests (ASTM C666). This testing involves a beam specimen undergoing multiple rounds of freezing and thawing cycles, combined with periodic measurement of the fundamental transverse frequency and calculation of the Relative Dynamic Modulus of Elasticity, which is used to assess the relative damage condition (i.e. lower Relative Dynamic Modulus of Elasticity values occur after a number of freeze thaw cycles have occurred and indicates the presence of damage). While this procedure is beneficial for comparing freeze thaw resistance of concrete mixes via small laboratory specimens (Wang et al. 2008), this an inviable option when considering in-situ conditions and damage detection applications. Additionally, the testing involved in this method does not allow for the location or extent of damage to be determined, and is not effective when considering microcracking which is associated with the early stage of freeze thaw damage.

Accurately detecting damage at its initial stages, and before excessive deterioration occurs, is a goal which has yet to be achieved by nondestructive testing techniques. Many nondestructive testing technologies have been employed for general cracking detection purposes, though freeze thaw damage is of particular interest to this

paper. Wave-based nondestructive evaluation techniques have been employed in the past for the detection of microcracking in cement paste. For instance, using diffuse ultrasound, quantitative measures of dissipation and diffusion coefficients can be found based upon the frequency and microstructure of cement-based materials (Becker et al. 2003). While the results showed promise for gaining insight as to the propagation of ultrasonic waves in cement-based materials, limitations were present due to sensitivity to diffusivity parameter selections.

Seismic tomography has also been utilized to detect cracking. This method differentiates zones based upon variation in the velocity of compression or P-waves. The seismic tomography analysis was successful in locating a major visible tensile crack in the structure. While this technology showed promise for the detection of damage below the surface, the device employed was only successful in detecting major cracks and thus not ideal for microcrack detection (Rivard et al. 2010).

Nonlinear acoustics, however, were seen to detect and track the formation of microcracks at a promising sensitivity level (Boukari et al. 2015). The ultrasonic approach enabled the type of damage to be determined based upon granular swelling assessment in order to designate ASR damage. While the results showed promise, there are limitations to the approaches used including limited applicability for certain ranges of ASR development and difficulty in detecting the reaction at its early stages. Additionally, the nonlinear parameter is extremely sensitive to microcracking. While this is a valuable asset for damage detection, the nonlinear parameter is not only sensitive to the number of cracks but also the features of the crack and the level of heterogeneity of the sample. This

highlights the need for a method which has high measurement efficiency, accuracy, and decreased subjectivity for concrete damage detection applications.

5.2.1.1 Ultrasonic Shear Velocity Array Device

In this study, shear waves were utilized for nondestructive evaluation in order to address the limitations discussed above. The utilization of shear waves allows for an analysis which is independent of moisture conditions. The ultrasonic shear velocity array device used for this research employs dry point contact (DPC) transducers capable of deep diagnostics (Shevaldykin et al. 2002), as described in depth previously.

The array setup accommodates multiple transducer pairs which allow for heightened measurement confidence, as well as incorporating redundancy (Hoegh and Khazanovich 2012, Hoegh and Khazanovich 2012a, Hoegh et al. 2012b, Hoegh et al. 2011). The measurements acquired by this device were used to develop methods for detecting freeze thaw damage in concrete slabs.

5.2.2 Experimental Investigation

The Electric Power Research Institute (EPRI) commissioned the fabrication of four slabs with various levels of freeze thaw damage, with each slab measuring 48 by 36 inches (122 by 91 cm) and 8 inches deep (20 cm). The mix was prepared with a 0.5 w/c ratio with no air entrainment. After fabrication, the four samples were moist cured for 14 days. The control sample was removed from the curing room and maintained at ambient temperature and relative humidity in the laboratory. The remaining samples were placed in an environmental chamber and subjected to cycles of freezing and thawing. The cycles consisted of temperatures in the chamber fluctuating between -20 degrees C and 12

degrees C at a relative humidity of approximately 98%. The duration of each cycle was approximately 45 hrs. A summary of the slabs which were tested is provided here, with corresponding visual survey results shown in Figure 33:

- Slab A: Control slab: no freeze thaw cycles induced, no visible cracking
- Slab B: Partially damaged condition: 72 freeze thaw cycles
- Slab C: Partially damaged condition: 80 freeze thaw cycles
- Slab D: Damaged condition: 114 freeze thaw cycles

Crack widths ranged from hairline cracks to 0.3 mm in width. Figure 34 shows a photo of the condition of slab D, further showing the damage present, as highlighted by chalking.

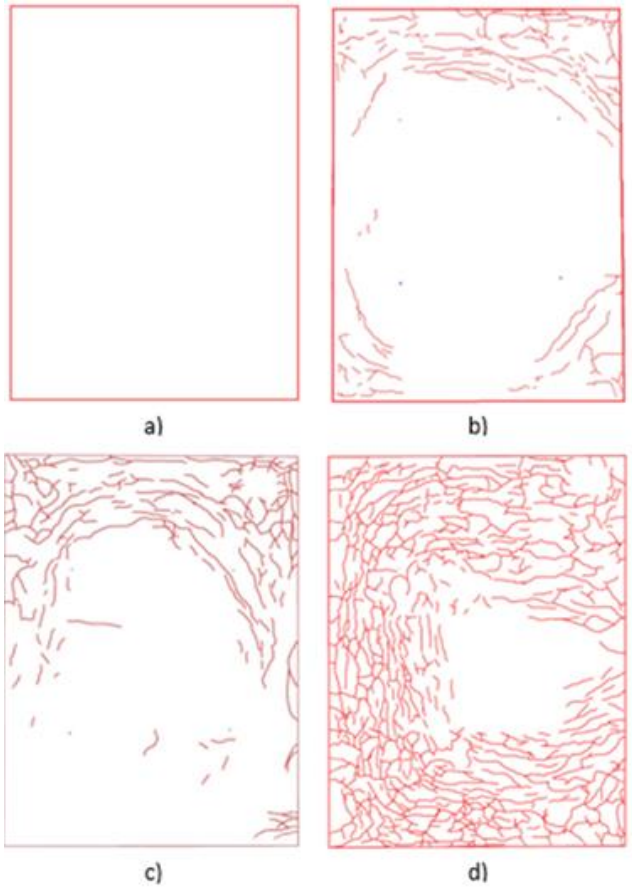

Figure 33. Visual condition surveys of slabs A, B, C and D.

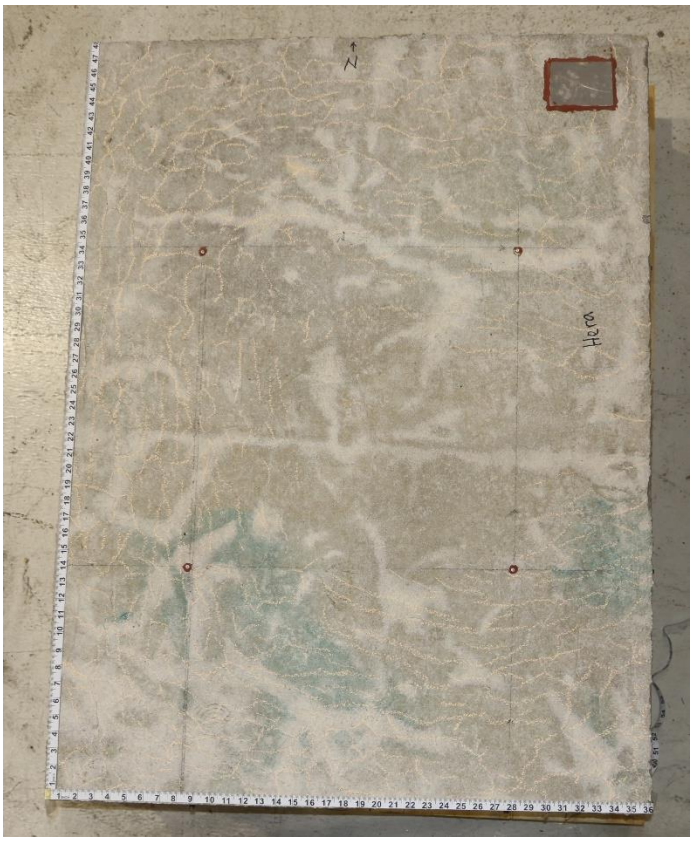

Figure 34. Photograph of condition of slab D.

These four slabs were tested using the ultrasound linear array device MIRA, as shown in Figure 35 (left). This device yields 45 individual time histories per individual scan. A total of 66 scans were obtained for each slab, using a frequency of 50 kHz. Because of the multiple transducer pairs, an expansive data set containing over 10,000 impulse time histories was obtained from this analysis. The 36-cm wide scans were taken in sets of 11 positions with a 5 cm step size (allowing for 35 cm of overlap from the previous scan), moving from north to south of each slab. This set of 11 scans was then taken in 6 different locations with a 12.5 cm step size moving east to west, as shown in

Figure 35 (right). As a result, the entire surface of the slab was analyzed and redundancy was incorporated via the overlapping nature of the measurement acquisition process.

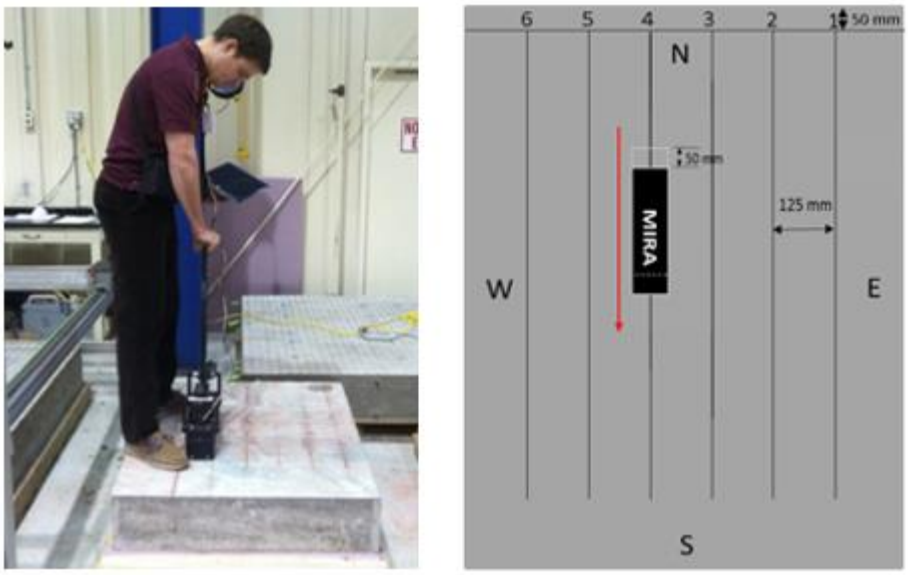

Figure 35. Experimental investigation setup (left), and schematic of measurement locations (right).

5.2.3 Ultrasound Evaluation Techniques

The ultrasound signals collected via the experimental investigation were analyzed to determine the condition of the concrete slabs. When the surface of the slab is excited by one of the transducers, the wave propagates through the specimen and a portion of the wave will reflect back when they encounter changes in properties, such as inclusions or layer boundaries. Each individual scan which is obtained results in the acquisition of 45 unique raw signals. The ultrasound signals collected via the experimental investigation were analyzed using two methods: one which focused upon the portion of the signal caused by the wave traveling along the surface, and another which utilized the subsurface reflection portion of the signal. These methods are described in the following sections,

and the respective results are compared both with each other and with the visual survey results.

5.2.3.1 Panoramic Reconstructions

The experimental investigation yielded 6 rows of 11 overlapping MIRA scans per slab. The measurements from each row of scans were used to create panoramic reconstructions, as detailed previously in section 3.2.2.1. Reconstructions provide focused images which show the presence of damage or inclusions, or in undamaged cases, the presence of only the backwall. Combining these individual SAFT reconstructions into one comprehensive panoramic reconstruction allows for analysis of the entire cross section and reduce signal to noise effects caused by the heterogeneous nature of concrete (Langenberg et al. 2012). For each panoramic reconstruction in this study, eleven individual SAFT scans were merged in this manner, as shown in Figure 36, yielding 6 panoramic reconstructions for each slab.

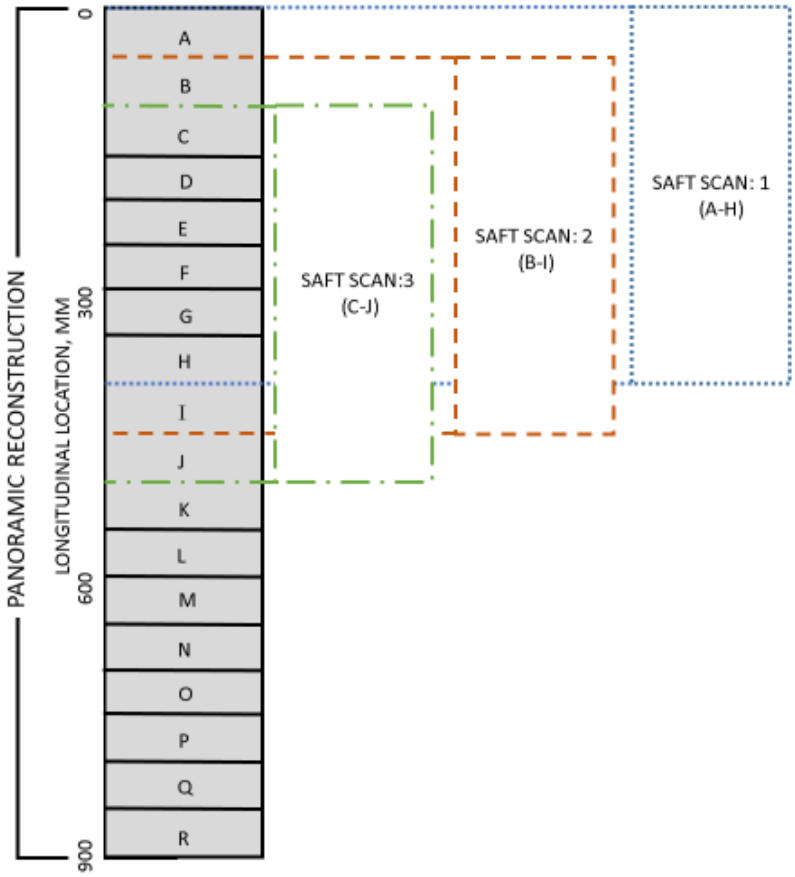

Figure 36. Panoramic reconstruction compilation schematic.

Visual analysis of the panoramics showed differences in the slab condition, most prominently through the presence of the backwall reflection (or the reflection caused by the bottom surface of the slab). This backwall presence is expected due to the sound condition of the concrete and lack of relative reflection prior to this depth. A typical scan on sound concrete (Slab A) is shown below in Figure 37. The backwall presence (at a depth of ~200 mm) is consistently strong, indicating strong relative reflection at the thickness interface as compared to its shallower features when evaluating the SAFT panoramic reconstructions. In other words, there is no damage present.

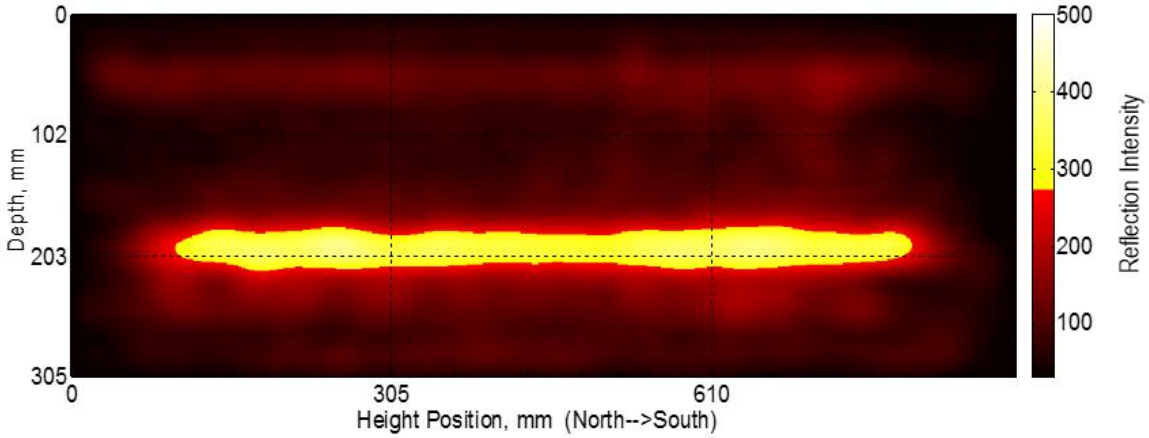

Figure 37. Reconstruction in the middle of slab A indicating sound concrete condition.

With conditions such as those shown in Figure 37 serving as the clean or reference case, categories could be created based upon deviations from this case. The following three categories were observed: 1) sound: reconstructions showing a strong and continuous relative reflectivity at the backwall; 2) partial damage: reconstructions exhibiting a strong backwall reflection at selected locations along with features indicating the presence of damage such as a discontinuity in the backwall reflection; 3) damaged: reconstructions showing no presence of a backwall reflection. Since this initial categorization is very general, it allows for reconstructions that are visually different to fit in the same category. To show the variation of reconstructions within a category and give a background in the indications used to categorize the sections, two examples of the partially damaged and fully damaged conditions are given below along with a description.

Figure 38 and Figure 39 show example reconstructions indicating a slightly damaged concrete condition. Figure 38 was taken on the West side of slab B (5th SAFT-

Pan). It shows a mostly sound concrete condition with a continuous and uniform backwall reflection in the middle and right side of the reconstruction. However, the lack of a backwall reflection on the leftmost (North) portion and a shift deeper in the backwall reflection on the left indicates the presence of damage. In this case, attenuation from damage could have shadowed the backwall in the former observation and increased the travel path in the latter. Figure 39 was taken in the middle of slab B (3rd and 4th SAFT-Pans). While both scans showed a shift in the backwall reflection deeper in the center, the scan taken at the 3rd SAFT-Pan (top) also shows direct reflections at a shallower depth, both indicating damaged concrete. However, these scans were still categorized as only slightly damaged, since portions on the left and right showed a strong backwall reflection.

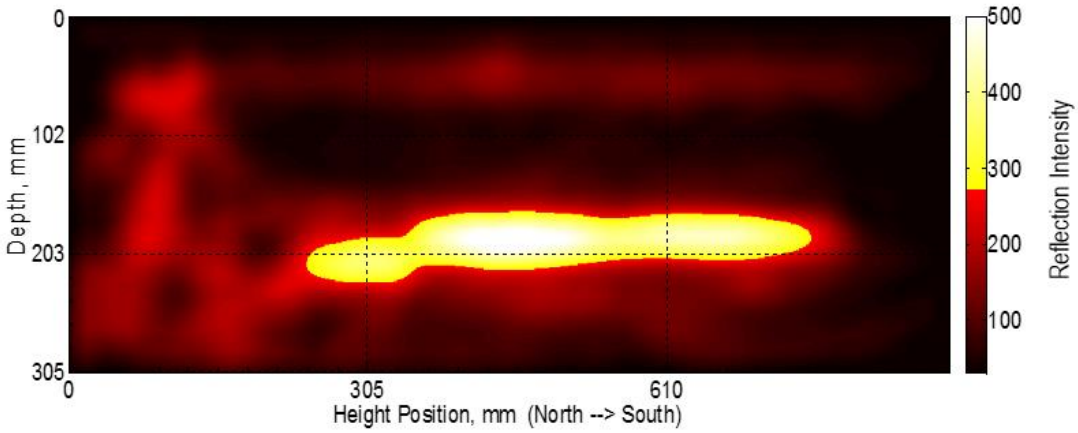

Figure 38. Reconstruction on the west side of slab B, indicating partially damaged concrete.

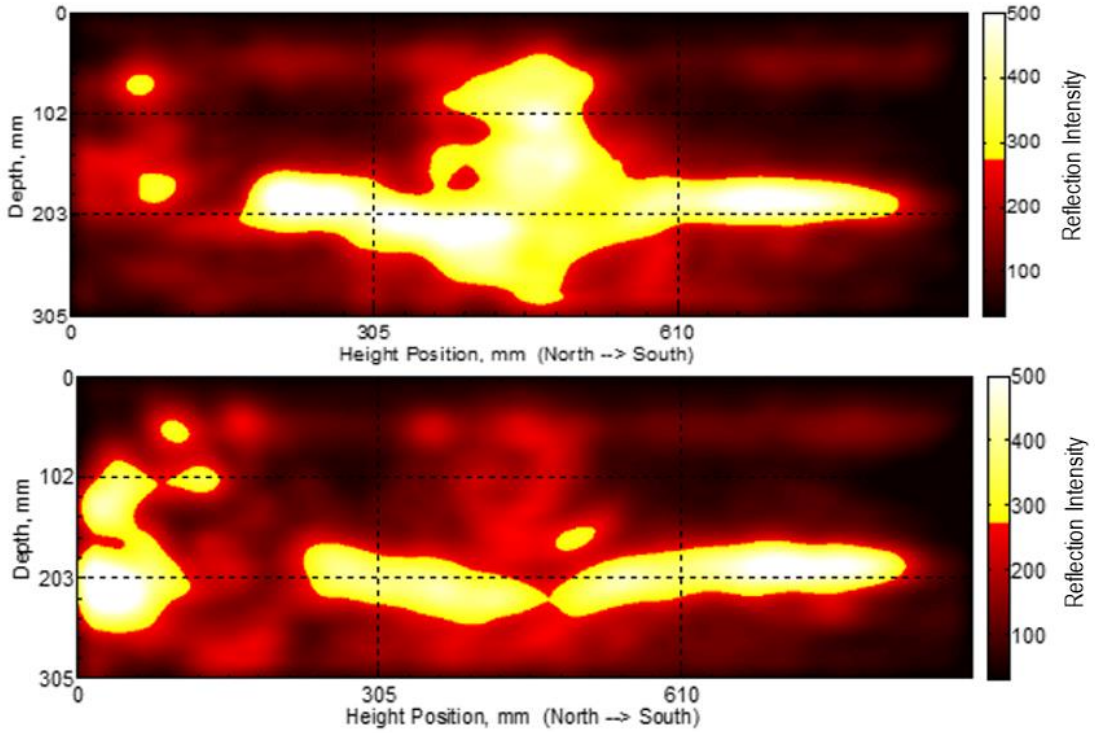

Figure 39. Reconstructions in the middle of slab C indicating partially damaged concrete condition.

Figure 40 and Figure 41 show example reconstructions indicating a damaged concrete condition. Figure 40 shows a scan taken in the middle of slab D (3rd SAFT-Pan). It shows a high reflectivity throughout the reconstruction and absence of a backwall reflection indicating the presence of damage. Figure 41 shows a scan taken on the west side of slab D (5th SAFT-Pan). Both scans showed a lack of a backwall reflection, either due to prohibitive noise at shallow depths or attenuation of the signal prior to arrival at the concrete depth interface, indicating damaged concrete. It is also worth noting that if regions of the upper layer of the concrete are severely damaged, then zones exhibiting significantly lower stiffness are present. This may cause multiple secondary reflections which can appear on the SAFT reconstruction as irregular damage zones, not necessarily corresponding to the boundaries of the damaged area. This

illustrates that SAFT techniques which are intuitive for planar defects and inclusions parallel to the surface (Hoegh and Khazanovich 2015) may lead to misinterpretation if applied to specimens with irregular damage present near the surface.

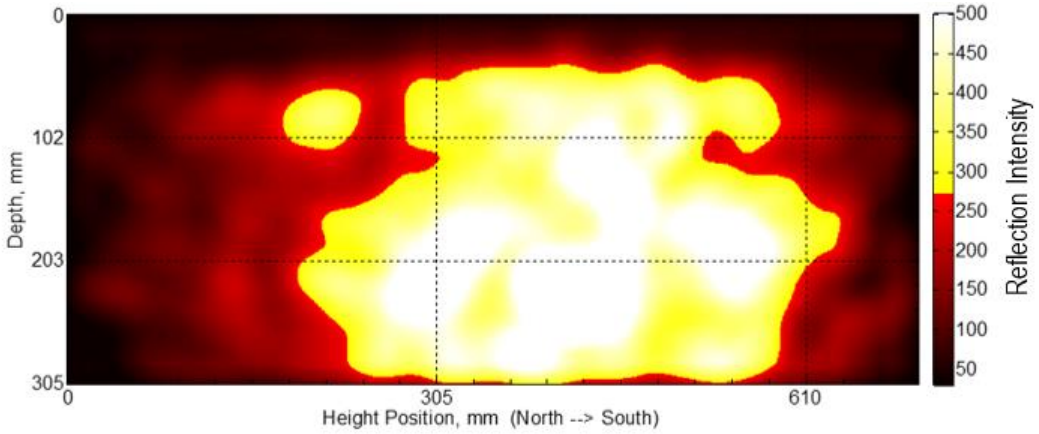

Figure 40. Reconstruction in the middle of slab D indicating damaged concrete condition.

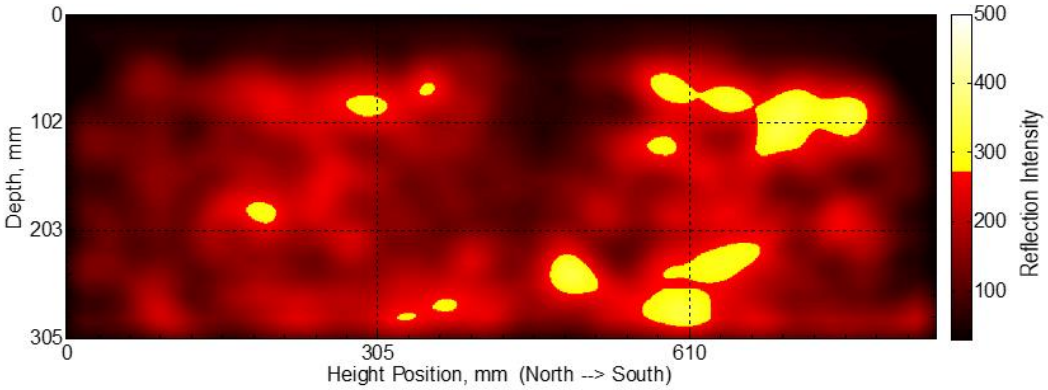

Figure 41. Reconstruction from the west side of slab D indicating damaged concrete condition.

5.2.3.2 Quantitative Analysis

While the panoramic reconstructions provide valuable qualitative information regarding the condition of the concrete, a quantitative analysis is desirable due to the objectiveness and efficiency of the results. The qualitative analysis requires subjective decisions, such as threshold selection and visual inspection, but the quantitative method suggested here is completely objective and utilized identical analytic variables for all scans.

The same impulse time histories which were implemented in the reconstruction analysis were utilized for the subsequent numerical analysis. As previously described, the linear array system which was used for testing creates an output of 45 unique impulse time histories. This raw data was used in order to perform a signal analysis, as detailed previously in section 5.1.1.

In order to incorporate redundancy and provide increased measurement confidence, the HTI values which are provided here are the result of averaging all 45 values to provide one more accurate designation per scan. These averaged HTI values are shown below in Figure 42 for all cases, with the clean data resulting from previous research efforts, as outlined previously. The median and quartile bars allow for the variability in values to be seen. The results from the clean and slab A data are very similar, showing that slab A is in sound condition, as was thought.

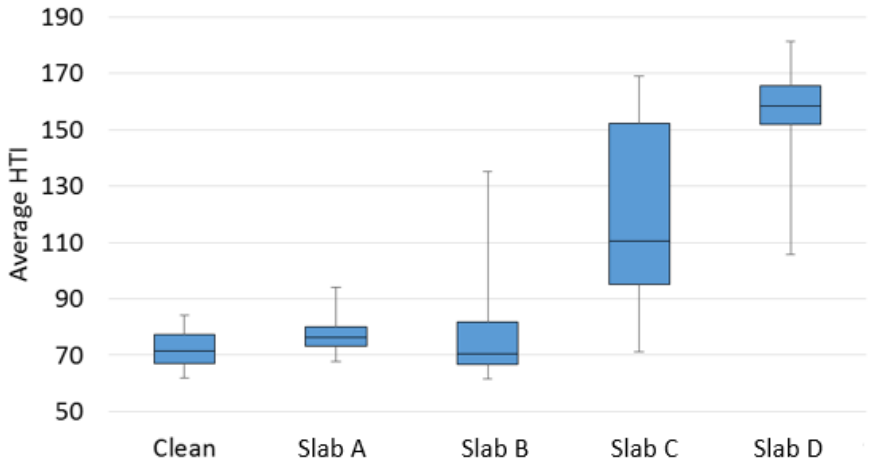

Figure 42. Average HTI values for five cases.

It is also worth discussing the variability in HTI values for the partially damaged and damaged slabs. This variability in indicator value stems from the variation in concrete condition throughout the slab. This is expected, as not all areas of the slab would be expected to be damaged to the same extent. Some regions still exhibit concrete in sound condition, as highlighted by the presence of low HTI values for slabs B and C. This is indicative of the partially damaged designations, as not all HTI values indicated damaged concrete. While variability is still present in slab D, the values all exceed 100 and thus all areas exhibit some signs of degradation, unlike the partially damaged slabs. The variability seen in all the cases shows the ability of the HTI values in properly diagnosing the progression of degradation present, regardless of extent of damage.

To further illustrate the statistical differences between the sample sets, a t-test and F-test were performed to compare the various cases. A summary of these results can be seen in Table 7. The results are as would be expected regarding the F-test conclusion, such that the partially damaged and damaged slabs had unequal variances with respect to

the control slab. The t-test results for the comparison of slab A to slabs C and D resulted in the rejection of the null hypothesis, meaning their means are unequal. The same conclusion was drawn from the Clean vs. slab A comparison, which is somewhat surprising. The cause of this result is the larger mean associated with slab A. Possibly the most surprising result is the P value for the slab A vs. slab B comparison. This high P value results in accepting the null hypothesis, indicating that the two data sets are statistically similar. This result stems from the fact that the means of the two samples are extremely similar (77.16 and 77.76 for slab A and B, respectively). However, the variation present in the values for slab B is not sufficiently accounted for in this result.

Table 7. Statistical results for concrete slab data

Cases Compared	t-test results: P value	F-test results	F-test Conclusion
Clean vs. Slab A	0.00013	F= 1.45, F_{crit}= 1.56	Variances are not unequal
Slab A vs. Slab B	0.7798	F= 9.50, F_{crit}= 1.51	Variances are unequal
Slab A vs. Slab C	$1.0157X10^{-16}$	F= 32.48, F_{crit}= 1.51	Variances are unequal
Slab A vs. Slab D	$4.925X10^{-55}$	F= 9.50, F_{crit}= 1.51	Variances are unequal

The variations present in the HTI values prove to be valuable when considering the scan locations. The HTI values for all scan locations from the freeze thaw slabs are shown in Figure 43. The color maps shown utilize a gradient in which white is indicative of the lowest HTI value seen (in this case, 62) and darker shades are indicative of the highest HTI value seen (in this case, 182). In other words, white or very light sections are representative of concrete in sound condition, while darker shades would indicate damaged concrete. In general, an HTI value less than 90 is indicative of concrete which is

in good condition. This threshold was determined based upon an extensive analysis of undamaged data from prior projects and is independent of mix design or other variables. As can be seen, the HTI values seem to capture the presence of damage accurately. Slab A, the undamaged slab, is the lightest in color and contains HTI values of 94 or less. Slab D, the most damaged slab, is the darkest in color with a minimum HTI value of 106 and a maximum value of 182. Slabs B and C have conditions ranging from sound to damaged, as would be expected, with slab C in a more damaged state than slab B.

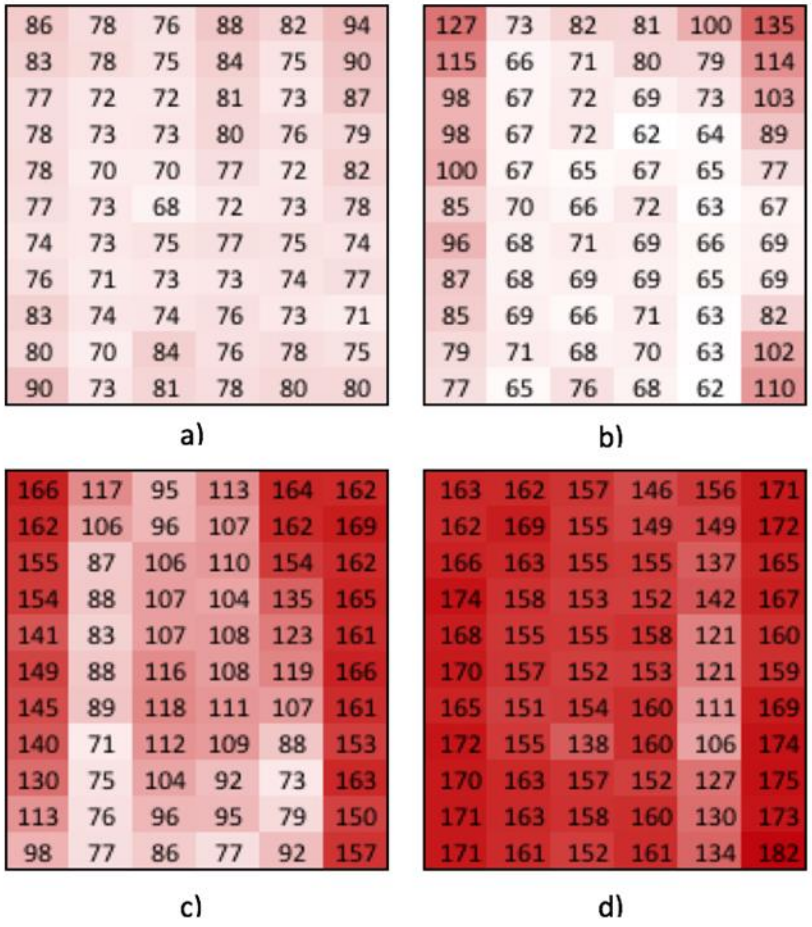

Figure 43. HTI color maps for: slab A, clean slab; slab B, partially damaged; slab C, partially damaged; and slab D, damaged.

While the progression of damage level in the slab data set is apparent, there are other trends that can be seen. In general, the greatest HTI values are those which are in the corners or edges of the slab. This can be explained via two rationales. The first of which involves the effects of edges on the ultrasound measurements. Because of the presence of edges and the proximity to walls, there can be additional distortion of the signal due to bouncing off of the boundaries. This can create slightly increased HTI values, though not significant. The greater justification for these increased values is the behavior of freeze-thaw damage. Water is most quickly absorbed via joints and edges due to their increased surface area and water penetration capabilities. As a result, freeze-thaw damage generally initiates at the edges or at pavement joints and moves inward, thus confirming the trend of greater HTI values present along the perimeter.

5.2.4 Results

Both methods described above produced categorized damage results for the slabs in a nondestructive manner. To compare the results of both analyses, the panoramic reconstructions are presented in conjunction with the HTI values which resulted from the numerical analysis. The results for this comparison are shown for slab B in Figure 44 and slab C in Figure 45. These figures show the six panoramic reconstructions on the left, with the HTI values for the same slab location shown both numerically and graphically on the right. The horizontal axis of the panoramic reconstructions, “Height Position”, corresponds to the actual location along the surface of the slab from north to south. The horizontal axis of the HTI graphs corresponds to the scan number from 1 to 11. These axes are essentially the same, as the scans were taken in numerical order from north to

south, aligning with the height position. Again, HTI values with dark shades indicate damaged concrete, while lighter shades indicate sound concrete.

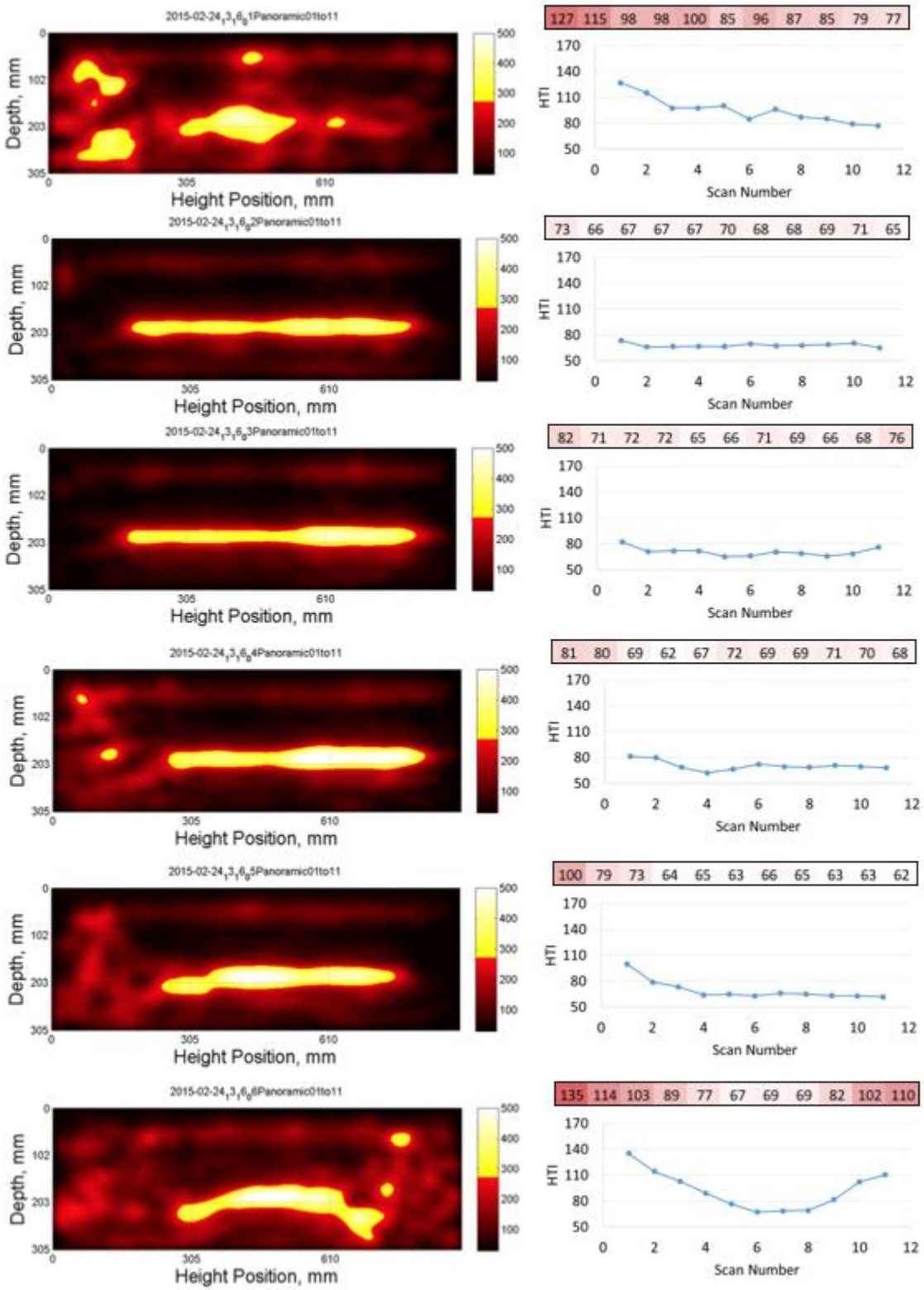

Figure 44. Comparison of panoramic reconstructions (left) and HTI index (right) analyses for slab B.

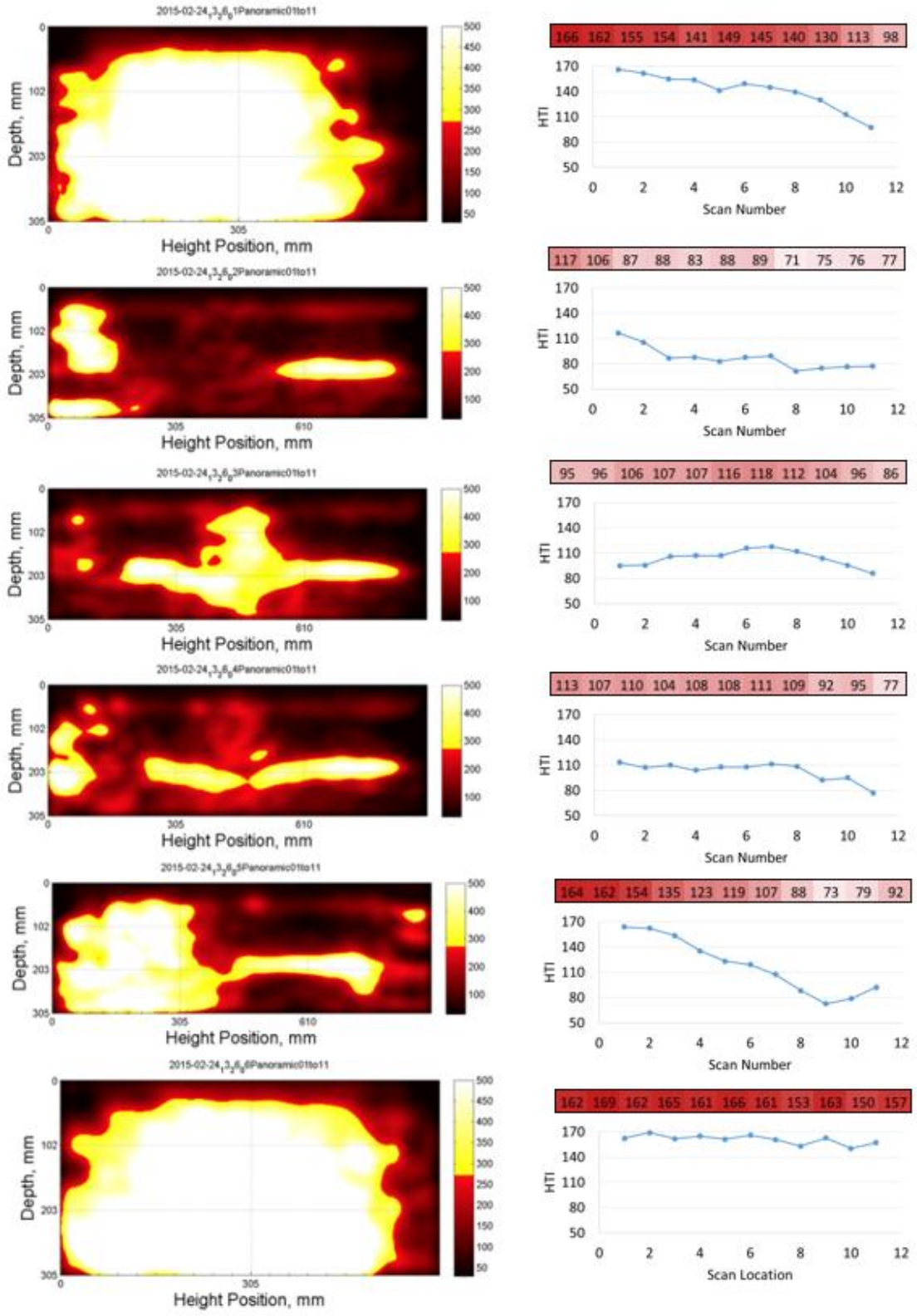

Figure 45. Comparison of panoramic reconstructions (left) and HTI index (right) analyses of sab C.

As can be seen from these figures, the HTI values show the same damage trends that can be deduced via the backwall presence in the reconstructions. For example, the bottom (sixth) panoramic reconstruction in Figure 44 shows that the backwall was not as apparent on the north and south regions, but was present in the center of the slab. The HTI results for the same scans show higher HTI values (over 100) for these same outer regions, while HTI values indicated sound concrete in the center (values in the 60s and 70s). As such, both methods showed that concrete was in sound condition in the center of the slab, but damage was present in the north and south regions. Conversely, the second and third panoramic and HTI results shown in Figure 44 indicate sound concrete throughout the entirety of that portion of the slab, as indicated by a strong backwall presence and consistently low HTI values. To summarize the condition of slab B, the 2nd and 3rd panoramics and HTI values showed sound concrete, while the remaining four sections showed signs of partially damaged concrete.

The same similarities can be seen in the results for slab C. The most damaged panoramics shown in Figure 45 are the first and sixth reconstructions. These scans also resulted in high HTI values, as indicated by the dark shading of the HTI color maps shown. Additionally, the fifth panoramic showed considerable damage on the left (north) side of the slab, with concrete in good condition on the right (south). These same trends are seen in the HTI color map and graph. The results for both slab D and slab A also showed very good agreement. These cases are not shown here for simplicity, as the scans were either all damaged or all sound. Instead, the intricacies of the intermediate partially damaged slabs were shown to highlight the robustness of the analyses presented.

As a result of the visual interpretation of all 24 panoramic reconstructions (6 panoramics per slab, each consisting of 11 individual scans), the condition of the slabs could be qualitatively determined via the diagnosis procedure discussed previously. All six panoramics for slab A had strong backwall presence and were deemed sound. Slab B had two reconstructions showing sound concrete and 4 reconstructions showing partially damaged conditions. Slab C had 2 reconstructions indicating partially damaged concrete and four reconstructions indicating damaged concrete. Finally, all six panoramic reconstructions of slab D were considered damaged, with no backwall presence. Additionally, more detailed conditions within each slab can be observed via trends in damaged locations. For example, the north side of the slabs generally showed greater damage levels than the south side. These same trends and damage categorizations were seen in the quantitative analysis results as well. The HTI values captured the same damage presence, without requiring visual interpretation.

The results of the qualitative and quantitative analyses can then be compared to the actual crack patterns demonstrated by the sample test slabs to confirm the results. The survey results shown in Figure 33 confirm the results of both analyses. When comparing Figure 43 and Figure 33, the same damage trends can be seen in the slabs, which were further confirmed via the qualitative analysis. Additionally, the trends of increased damage on the northern portion of the slabs was confirmed via the visual surveys. Moreover, the survey of slab D (d) shows that no visible damage was present in the center portion of the slab, while the quantitative analysis indicates that the concrete in

this area is not sound with HTI values of over 100 for the entire slab. This shows promise for detecting damage prior to its appearance at the surface.

5.2.5 Conclusions

The methods presented in this section were implemented in order to categorize the damage level within concrete slabs with varying levels of freeze thaw damage. While the two methods employed vary in their analysis type, they both utilize the same signal data obtained by an ultrasonic shear wave linear array device. Both methods were successful in determining the presence of damage in a noninvasive and efficient manner. The qualitative analysis of the panoramic reconstructions highlighted specific slab areas in which damage was causing shadowing of the backwall, while the quantitative analysis utilized the effect of damage on signal shape in order to numerically indicate the condition of the concrete. Both methods are advantageous from a confidence standpoint as well. The panoramic reconstructions utilize overlapping scans, adding redundant measurements to increase measurement assurance. The quantitative indicator, HTI, is based upon the numerical analysis of all 45 impulse time histories from each scan. As a result, the sample set is large and produces confidence in the indicator. Moreover, the HTI method can be implemented on in-situ pavements for determining real-time concrete condition, without requiring previous measurements for comparative purposes. As a result, the applications of this technique are vast. The results of this study show promise for the implementation of methods which can characterize the condition of concrete in an efficient and nondestructive manner. Further work is necessary in order to determine the

depth of the damage, a limitation which is present in both methods, and can be accomplished in conjunction with simulation efforts.

5.3 Alkali-Silica Reaction Damage

[This section is partially adapted from a submission to Cement and Concrete Research]

Alkali-silica reaction (ASR) causes degradation similar to that of freeze thaw damage but is the result of a different physical mechanism. ASR refers to the chemical reaction which occurs in concrete, caused by the interaction of alkalis present in Portland cement and silica found in aggregates. The result of this process is the formation of a gel, referred to as ASR gel, which creates expansive pressures and microcracks within the material. This cracking results in extensive degradation to the concrete system, a phenomenon which plagues aging infrastructure. Though much research has focused upon the mechanisms of ASR, this type of degradation remains problematic and preventative methods have yet to be successfully determined. Because of this, much research has focused upon the modeling and intensive understanding of ASR (e.g. Bazant 2000, Bazant 2000a, Berra 2010, Giaccio 2008, Multon 2009), including a focus upon the conscious selection of aggregates to mitigate ASR (Berra 1999, Chen 2010, Multon 2010). A review of the current techniques for modeling of ASR was performed by Pan et al. in 2012 and the authors concluded that the models are based upon empirical concepts, while more complex approaches fall short due to shortcomings in the modeling and understanding of microcracks.

5.3.1 Previous Research in ASR Detection

Due to the extent of degradation associated with ASR, this type of damage has been the focus of nondestructive evaluation efforts in recent history. Diffuse ultrasound has been employed Deroo et al. (2010) to quantify microcracking in concrete. This research focused specifically on the diffusivity and dissipation parameters, noting that diffusivity decreased with increased damage, while dissipation saw little change. Increased scattering caused by microcracks was the cause of the decrease in diffusivity which occurred.

Methods incorporating the nonlinear evaluation of concrete have also been utilized in the past. One such method, Nonlinear Impact Resonance Acoustic Spectroscopy (NIRAS) was used to measure the nonlinearity in a specimen caused by microcracks (Lesnicki 2013). The results of this analysis showed that the method could identify microstructural damage, however the samples utilized were small in size and required laboratory implementation with a mechanical impact. Further nonlinear analysis has been performed using ultrasonic waves and an associated acoustic nonlinearity parameter to assess ASR damage (Qu 2015). An initial investigation of the wave speed and wave attenuation showed a lack of sensitivity to ASR damage, however the nonlinearity parameter had increased performance with respect to ASR damage levels. This method again used mortar bars in the laboratory, creating applicability issues including aggregates and in-situ concrete specimens.

The methods described above have obvious limitations with respect to ASR damage detection. While the above method showed some initial success and promise in detecting ASR gel, no work was done on in-situ or full-scale samples. Additionally, these

methods were unable to successfully detect all damage levels. To address these limitations, an ultrasonic linear array device was utilized for this research.

5.3.2 Materials and Methods

To test the applicability of the nondestructive evaluation of concrete slabs with ASR damage using an ultrasonic linear array device, an experimental investigation was performed on sample slabs and a subsequent data analysis was performed. The methods employed by these analyses are described in the following sections.

5.3.2.1 Experimental Procedure

The Electric Power Research Institute (EPRI) commissioned the fabrication of four slabs with various levels of alkali-silica reaction, with each slab surface measuring 48 by 36 inches (122 by 91 cm) by 8 inches (20 cm) thick. The following four slabs were tested:

- Slab 0: Unreactive aggregates; no damage (control specimen)
- Slab 1: Highly reactive aggregates: Partially damaged condition
- Slab 2: Highly reactive aggregates: Partially damaged condition
- Slab 3: Highly reactive aggregates: Low damage condition

The reactive aggregates which were used came from Wells, Maine (ASR-AC1), Bernalillo, New Mexico (ASR-AC2), and El Paso, Texas (ASR-FA). Additionally, a high equivalent alkali content Type I Portland cement was used for the ASR slabs. Sodium hydroxide was added to the mixtures in order to obtain an equivalent alkali content of 1.25%. The mix design used for the construction of the slabs is shown below in Table 8, with a w/cm ratio of 0.50 used for all mixes.

Table 8. Mix design for concrete slabs

Component	Control- Slab 0 kg/m^3 (lb/yd^3)	ASR- Slabs 1, 2 and 3 kg/m^3 (lb/yd^3)
Cement – Type I	-	420 (708)
Cement – Type II	420 (780)	-
Water	210 (354)	210 (354)
ASR-CA1*	-	429 (723)
ASR-CA2*	-	429 (723)
CA*	1095 (1845)	-
ASR-FA*	-	818 (1379)
FA*	639 (1077)	-

* Oven Dry

To induce ASR in the reactive slabs, temperature and relative humidity in the environmental chamber were maintained at 27°C (80.6°F) and 65%. Temperature within the chamber was increased to 32°C (89.6°F) on day 93 to speed up the ASR damage. Slabs were draped with wet burlap and wrapped in plastic once per week to maintain a supply of sufficient moisture. The non-reactive control slab remained in the concrete laboratory at a constant 23°C (73°F) and was draped in wet burlap once weekly.

The ultrasonic linear array device described previously was utilized to obtain scans on the slabs on day 103 (January 25th), as shown below in Figure 46. The entire surface of the slab was tested, using overlapping scans in the orientation and sequences shown in Figure 46 (b). The scans were taken along 6 rows from east to west, with 12.5 cm step sizes utilized. Within each row of scans, overlapping measurements were obtained with a step size of 5 cm moving north to south. As a result, 66 scans were obtained for each slab, allowing for the formulation of 6 panoramic reconstructions.

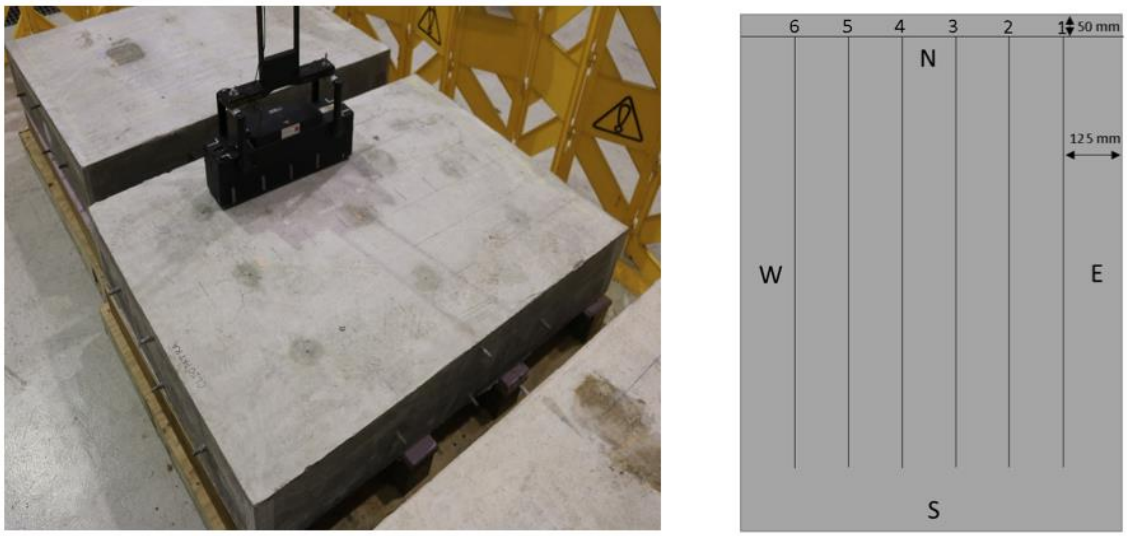

Figure 46. Ultrasonic device positioned on slab 2 (a) and readings location schematic (b).

This scan data was utilized for a similar analysis to that which was performed for the slabs with freeze thaw damage, however, an additional velocity analysis was performed. The results of these analyses are shown in Table 9. The HTI values given in this table are the result of averaging the 45 individual HTI values from all 11 scans within the panoramic locations. The same holds true for the velocity values given in this table. The column labeled "Concrete Condition" refers to the result of the visual panoramic reconstruction analysis, performed in the same fashion as that which was outlined in section 3.2.2.5. The results presented in this table again show that the trends in HTI values correspond well with the concrete condition designation resulting from the panoramic reconstructions. Further exploration of the HTI and velocity values is given in section 5.3.4.

Table 9. Summary of results for all panoramics.

Slab	Panoramic Location	HTI	Velocity (m/ms)	Concrete Condition
Slab 0	1	74.95	2.349	Sound
	2	68.26	2.407	Sound
	3	69.49	2.417	Sound
	4	66.95	2.412	Sound
	5	72.67	2.297	Sound
	6	71.42	2.451	Sound
Slab 1	1	108.03	2.096	Partial Damage
	2	97.01	2.148	Partial Damage
	3	105.97	2.130	Partial Damage
	4	108.31	2.102	Partial Damage
	5	105.31	2.129	Partial Damage
	6	109.50	2.100	Partial Damage
Slab 2	1	104.31	2.118	Partial Damage
	2	106.87	2.142	Partial Damage
	3	110.11	2.144	Partial Damage
	4	101.71	2.157	Partial Damage
	5	107.23	2.162	Partial Damage
	6	105.39	2.124	Partial Damage
Slab 3	1	90.98	2.128	Partial Damage
	2	83.91	2.122	Sound
	3	79.67	2.131	Sound
	4	81.08	2.133	Sound
	5	85.96	2.133	Sound
	6	88.82	2.146	Partial Damage

5.3.3 Panoramic Reconstructions

Since the initial categorization of concrete condition is very general, reconstructions that are slightly different can fit in the same category. A few examples with commentary will be shown in this section. It is also worth noting that as no reconstruction achieved the third categorization level (damaged), there are only examples of the first two categories. Figure 47 and Figure 48, shown below, are both taken from slab 0 and are representative of the sound concrete condition seen for all panoramics taken from this slab. Figure 47 is

a reconstruction taken in the middle of slab 0 (3rd SAFT-Pan). While this scan shows a sound concrete condition with a continuous backwall reflection spanning the width of the reconstruction, slightly more attenuation of the backwall reflection was observed around the 300 mm marking. This may indicate the presence of a developing stress or poor concrete consolidation being reflected above the backwall. The same happens to panoramic 5 taken on slab 0 (Figure 48). Figure 48 is still representative of sound concrete, but a weaker reflection after the middle of the reconstruction (400 mm marking) is present. This indicates a more sound concrete in the north region of the specimen than in the south.

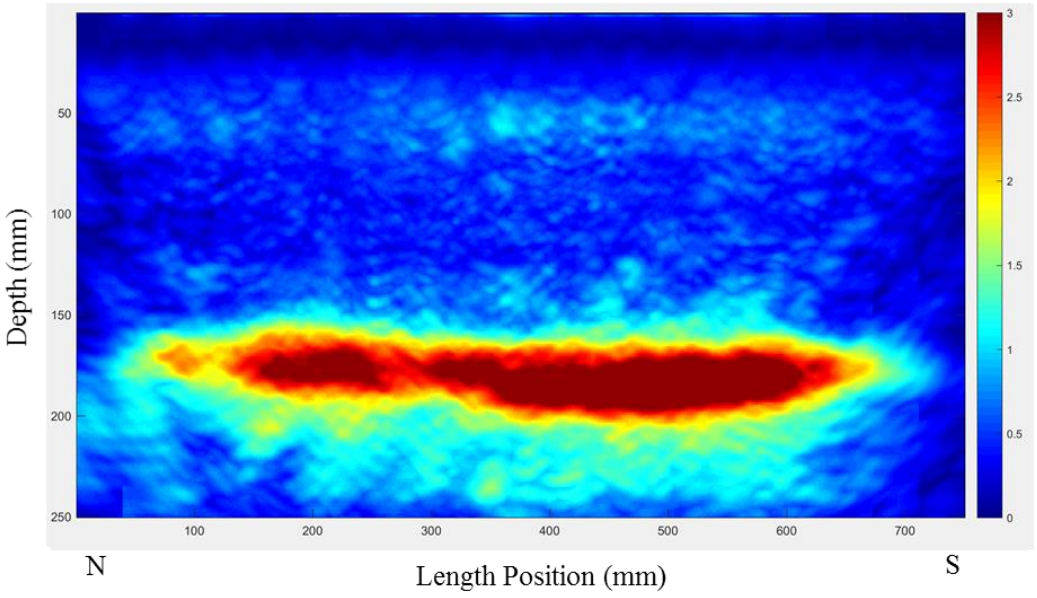

Figure 47. SAFT-Pan Reconstruction of specimen Slab 0, panoramic 3

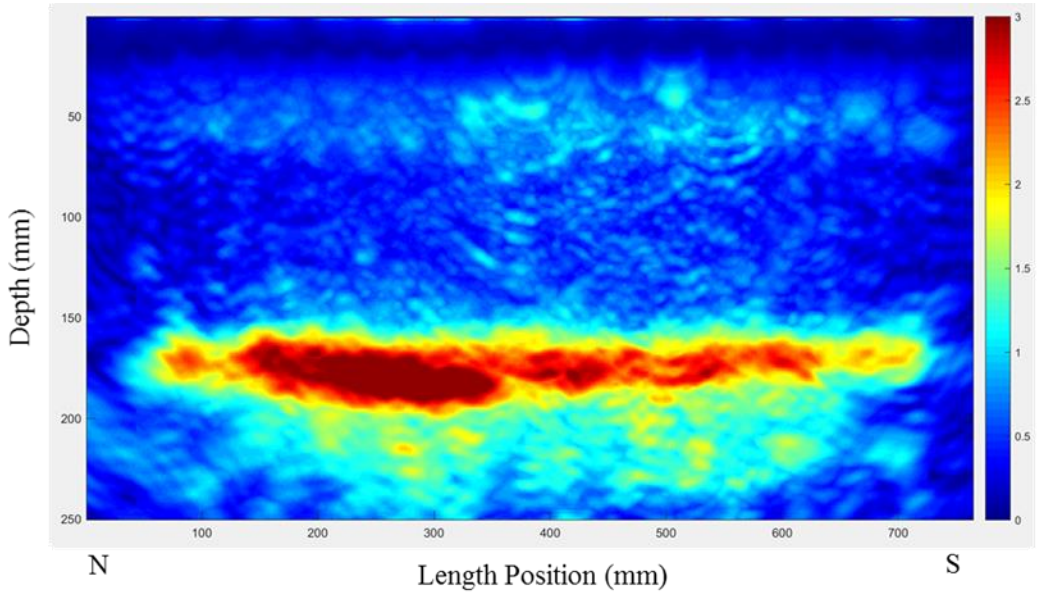

Figure 48. SAFT-Pan Reconstruction of specimen Slab 0, panoramic 5

Slab 3 presents both characterizations “sound” and “partial damage”. Reconstructions of these conditions are shown in Figure 49. Figure 49a displays the middle of slab 3 (4th SAFT-Pan) showing a clear sound concrete condition with a continuous and uniform backwall reflection throughout the width of the reconstruction. On the other hand, Figure 49b (6th SAFT-Pan) presents more attenuation at shallower depths, indicating the existence of partial damage.

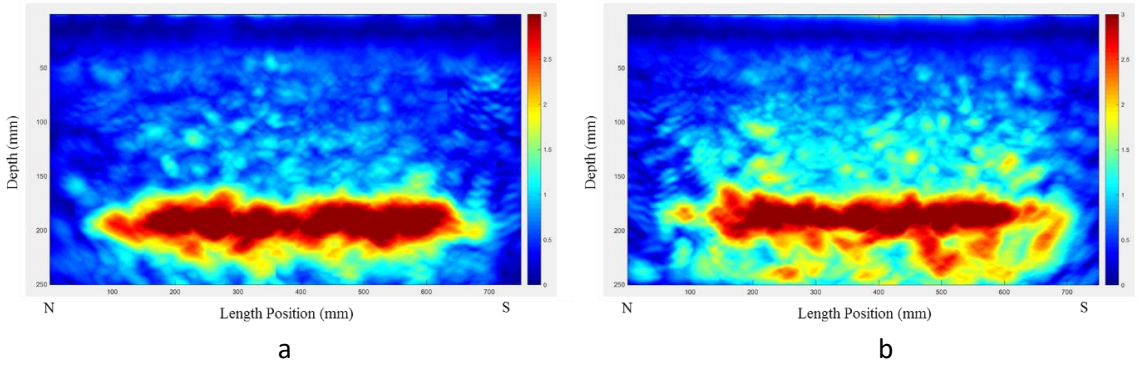

Figure 49. SAFT-Pan Reconstructions of specimen slab 3, (a) panoramic 4 and (b) panoramic 6

Figure 50, Figure 51, and Figure 52 show reconstructions which serve as examples that indicate a slightly damaged concrete condition (or partially damaged). Figure 50 was taken on the west side of slab 2 (5th SAFT-Pan). It shows a mostly sound concrete condition with a continuous and uniform backwall reflection in the middle of the reconstruction. However, the breaks in backwall continuity at the edges of the reconstructions, in conjunction with more attenuate reflections near the backwall, indicates the damage presence. Figure 51 shows a reconstruction for slab 1(1st SAFT-Pan) with more strong reflections and a clear break in the backwall at the end of the reconstruction (south area). In both cases, attenuation from damage could have shadowed the backwall in some parts of the reconstruction.

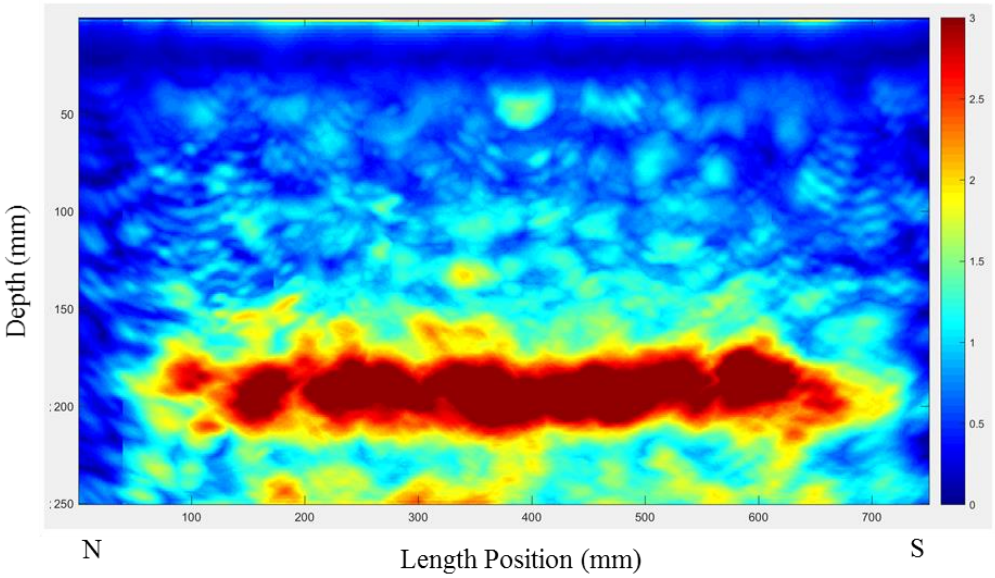

Figure 50. SAFT-Pan Reconstruction of slab 2, panoramic 5

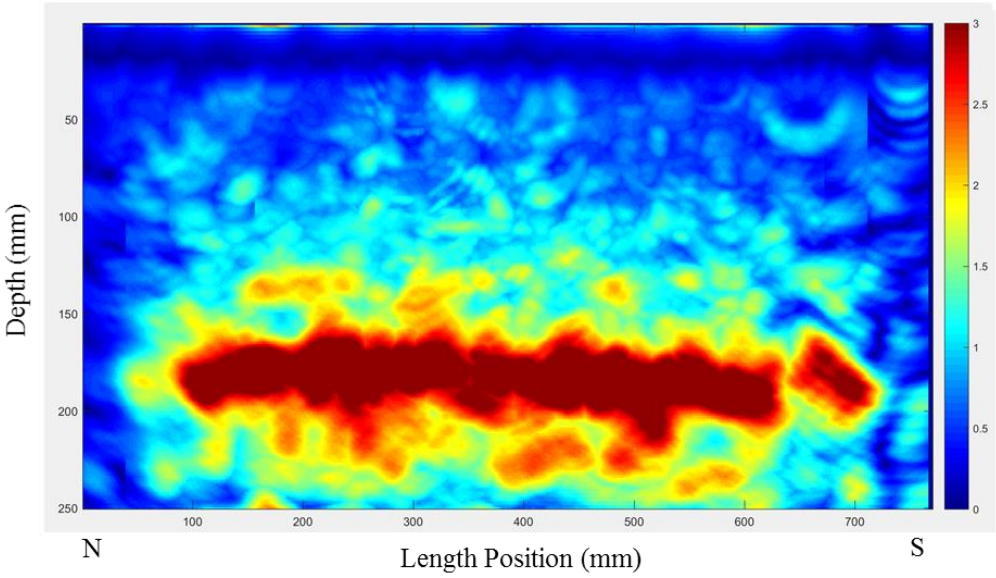

Figure 51. SAFT-Pan Reconstruction of slab 1, panoramic 1

Figure 52 was taken from the east side of slab 2 (1st SAFT-Pan). The reconstruction shows a possible distress in the middle of the specimen (dark reflection above the backwall). This reflection has a shadowing effect on the backwall right before and after the reflection position. Also, the north part of the specimen presents a weaker backwall than the south part, indicating a more damaged condition associated with the north region. It is again worth noting that these panoramic reconstructions show partial damage conditions, or the early onset of degradation, with no panoramic reconstructions showing characteristics associated with the presence of severe damage.

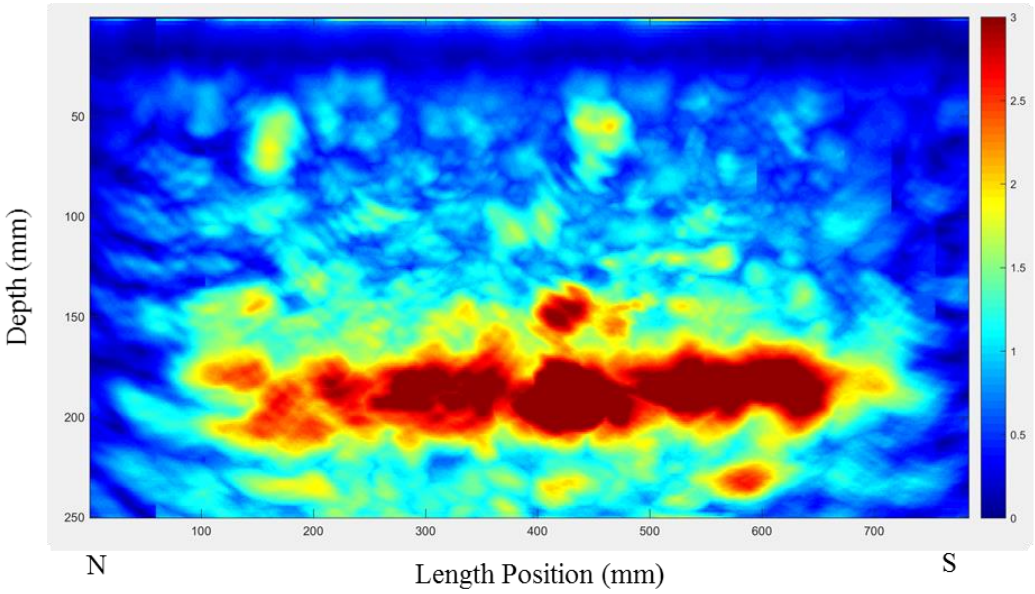

Figure 52. SAFT-Pan Reconstruction of specimen slab 2, panoramic 1

5.3.4 Quantitative Analysis

The same quantitative analysis involving the HTI index was performed on the ASR slabs. Additionally, the shear wave velocity was calculated, as described in section 2.2.1, for each scan location. This data was previously presented in Table 9. To compare the results of the HTI and shear velocity analysis, Figure 53 was created to show the relation between the HTI and the shear wave velocity. As can be seen, the control specimen (slab 0) presents HTI values consistently below 80, while the shear wave velocity varies greatly. The most damaged specimens (slabs 1 and 2) show most scans with HTI values above 100 and low velocity. Slab 3 shows what can be interpreted as the first stages of damage. Only three scans presented HTI values above 100, with the remaining values averaging around 85. The specimen has reactive aggregate but still presents concrete in mostly sound conditions, as shown by the majority of low HTI

values throughout the slab. These results confirm the lack of accuracy associated with shear wave velocity measurements in detecting damage that was seen for in the laboratory beam tests. The Hilbert Transform Indicator was much more successful in characterizing the concrete condition, and moreover was able to distinguish between varying levels of distress.

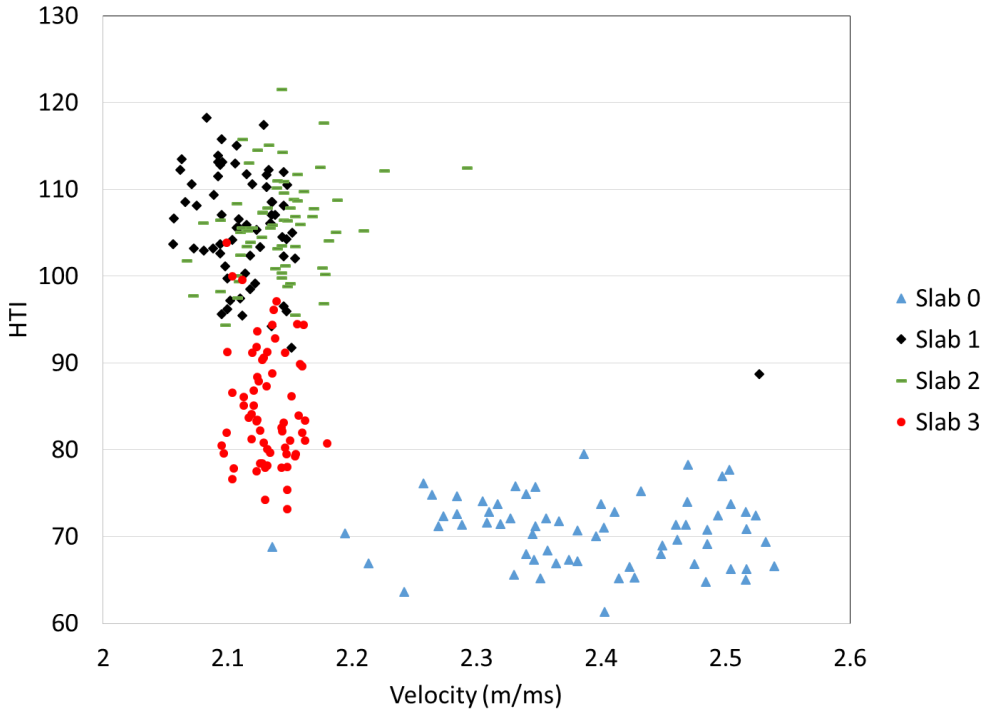

Figure 53. HTI versus shear wave velocity

The ability of the HTI values in distinguishing between areas of damaged concrete is exhibited by the color map results shown in Figure 54. Again, darker shading indicates a higher HTI value, or a more damaged area. The maps show that he control specimen, Slab 0, was in good condition, while slabs 1 and 2 exhibited higher levels of damage as indicated by the HTI values. It should be noted that extreme damage conditions were not present in any of the slabs, as would be indicated by very dark

shading not seen here. In other words, even the darkest shade seen in Figure 54 is not indicative of severe damage, only signs of partially damaged concrete. Slab 3 has both damaged and sound concrete conditions, as also shown by the concrete condition diagnosis resulting from the visual analysis of the reconstructions, indicating the early stages of damage progression.

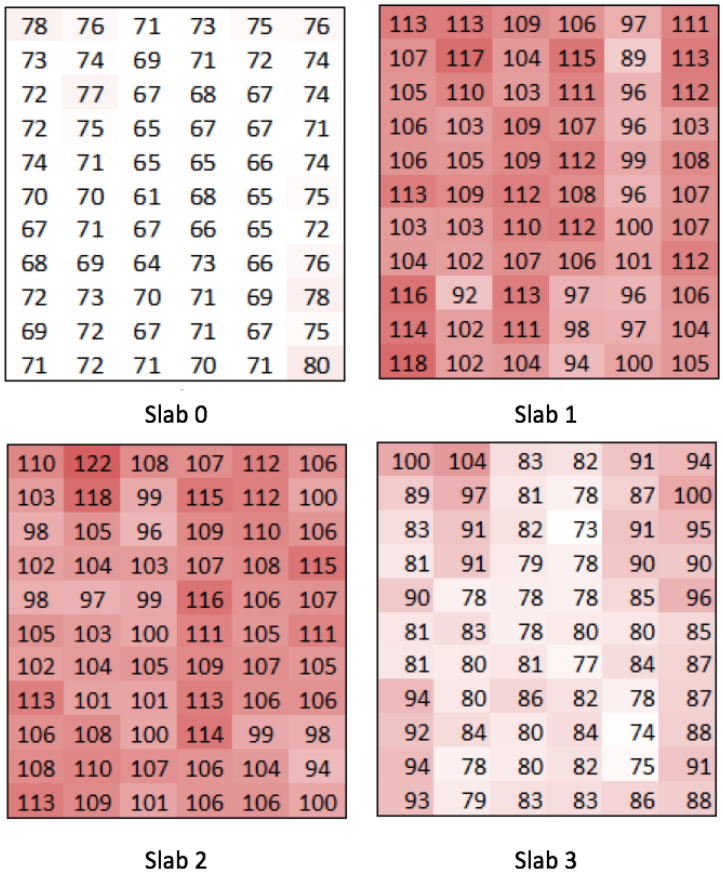

Figure 54. HTI color map for specimens slab 0-3.

5.3.5 Results

To confirm the results shown by the HTI and reconstruction analyses, visual cracking patterns were obtained from EPRI. Examination of surface cracking in all specimens confirms the damage presence on slabs 1 and 2, as shown in Figure 55, with cracks

highlighted for greater ease of identification. The rectangle on Figure 55 (top) shows an enlarged section of the specimen in order for cracks to be more easily visible. Slabs 0 and 3 did not have any visible surface cracks.

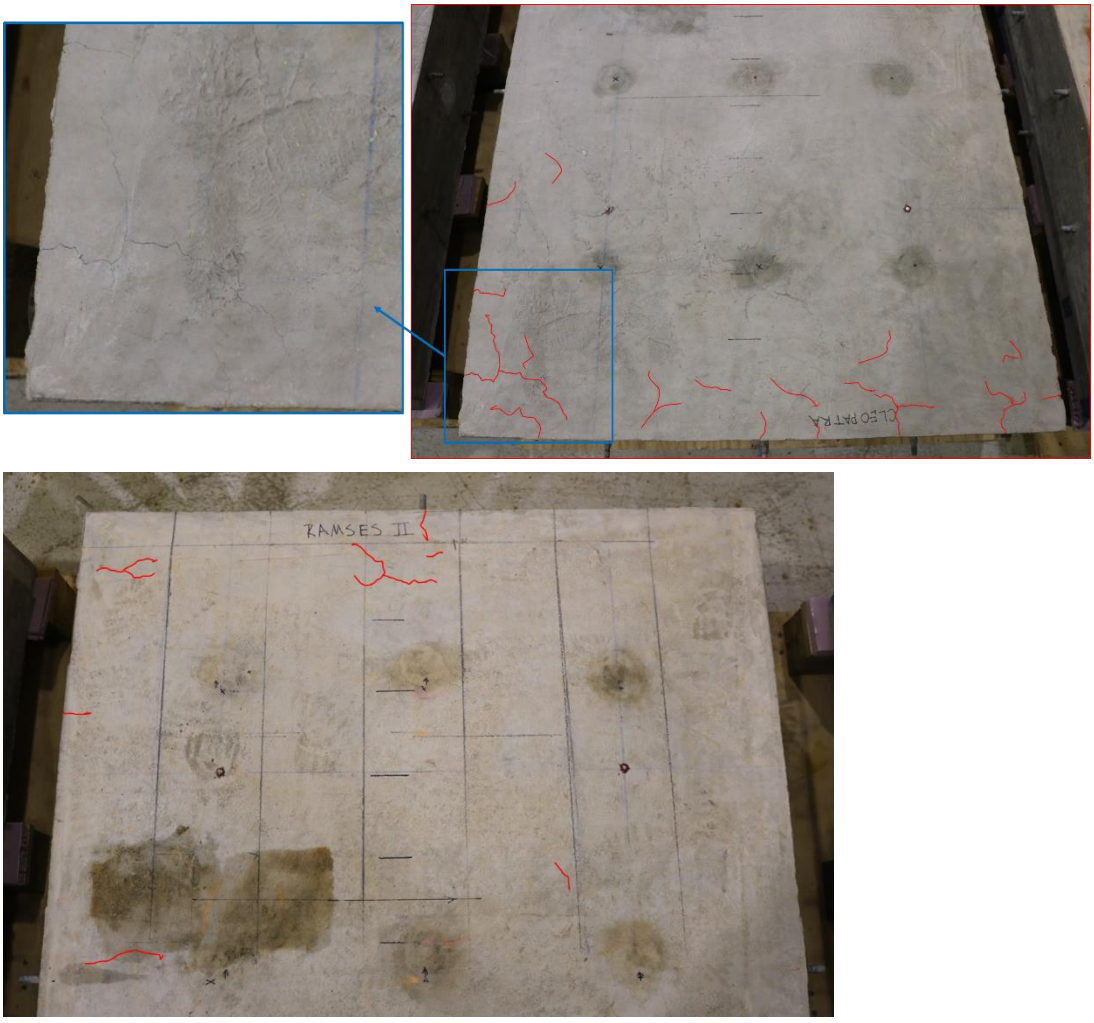

Figure 55. Visible cracking in south portion of slab 2 (top) and north portion of slab 1 (bottom).

Additional data regarding the condition of the slabs was gathered by EPRI via the utilization of DEMEC discs (Demountable Mechanical strain gauges) to obtain expansion data. The expansion values for each slab are shown in Table 3 for two different dates: firstly at 45 days, right before the specimens were shipped to EPRI (Klenke and Giaanni,

2015), and at 215 days of age, 20 days before the MIRA testing. Expansion for the latter data was obtained through personal communication with EPRI engineer Salvador Villalobos. Table 3 also brings the average HTI values for each slab. Again, these average HTI values are the result of the averaging of all 66 scan values, with each individual scan containing 45 individual HTI values as a result of the transducer pair interaction. As can be seen, there is good agreement between the expansion and HTI values. It is also worth noting that the standard deviation of the HTI values is quite low, further validating the accuracy of this method.

Table 10. Expansion and HTI values for all four slabs.

Slab	Expansion (45 days)	Expansion (215 days)	Average HTI	HTI (Std)
Slab 0	-0.012%	-0.0278%	70.6	2.70
Slab 1	0.087%	0.179%	105.7	4.13
Slab 2	0.046%	0.141%	105.9	2.61
Slab 3	0.057%	0.091%	85.1	4.00

5.3.6 Conclusions

The investigation of ASR damage in concrete slabs resulted in similar results to those seen for the freeze thaw analysis. The visual comparison of reconstruction images again provided concrete condition information via the presence, or lack thereof, of the backwall. However, none of the slabs were severely damaged, therefore those observations for a heavily damaged freeze thaw slab were not able to be confirmed via this investigation. The HTI results were promising and seemed to also adequately capture the presence of ASR damage. Moreover, the control slab (slab 0) added further to the sound data inventory and confirmed previous trends in that regard, despite differing mix

designs and concrete location. This further proves that the implementation of the HTI analysis is possible on a widespread basis due to its lack of dependence on these variables. The ASR slabs also involved an analysis of shear wave velocity with respect to damage detection capabilities. The variation in shear wave velocity that was seen was similar to those found in the laboratory beam trials. As such, this method does not accurately detect the presence of damage due to its observed inconsistencies.

5.4 Environmental Damage Detection Conclusions

Through the investigative efforts presented in the previous sections, the applicability of visual reconstructions and a quantitative indicator were successfully determined. Both were able to accurately detect the presence of damage from that of freeze-thaw and ASR. The creation of panoramic reconstructions allowed for the characteristics of sound concrete to be determined, and deviations from that condition allowed for the detection of damage. This was most prominently evident through the presence of the backwall in the reconstructions. The HTI analysis was successful in determining both the presence and the severity of environmental damage as well. The variations in HTI values provided this insight and the results aligned well with the survey results. Moreover, this type of analysis does not require any previous structural history to make condition assessments and is thus highly desirable for field implementation.

CHAPTER 6: NUMERICAL SIMULATION

In order to both verify the results that were seen in the aforementioned experimental investigations, and to gain further understanding regarding the wave propagation involved with this technique, a signal simulation software was developed and refined. This simulation program aims to predict the signal outcomes obtained using MIRA. The refinement of this program allows for trial cases to be ran, and their corresponding outcomes to be analyzed in order to gain more understanding as to why the impulse time histories have specific characteristics.

6.1 Simulation Development

As discussed previously in the literature review, the simulation utilized for this research relies upon EFIT for its efficiency in handling heterogeneous materials, a trait essential for the analysis of concrete. The simulation program, developed at the University of Minnesota, allows for flexibility in boundary conditions, including free, fixed and absorbing boundaries. The model is also capable of both 2D and 3D domains, with further personalization incorporated by both elastic and viscoelastic computational capabilities. The application of EFIT to the discretized partial differential equations is done using a subprocess written in FORTRAN 90/95. The FORTRAN 90/95 code accepts a simple input text file, with the results processed using MATLAB image processing. The results of the EFIT analysis are in the same format as the output from MIRA, and thus the same image processing can be utilized for both.

To simulate the output of MIRA, the transmitting signal had to be determined. The central frequency of this signal is 30 kHz in the current state of the program and is as shown in Figure 56. For the purposes of the research presented here, horizontal shear waves were simulated using anti-plane deformation and viscoelastic material properties were utilized. This was selected both for accuracy and computational efficiency purposes. Additionally, no reinforcement was utilized in the case studies presented here, though that is an option within the simulation code. An absorbing boundary was utilized for the left and right boundaries, with the bottom surface modeled as a free boundary.

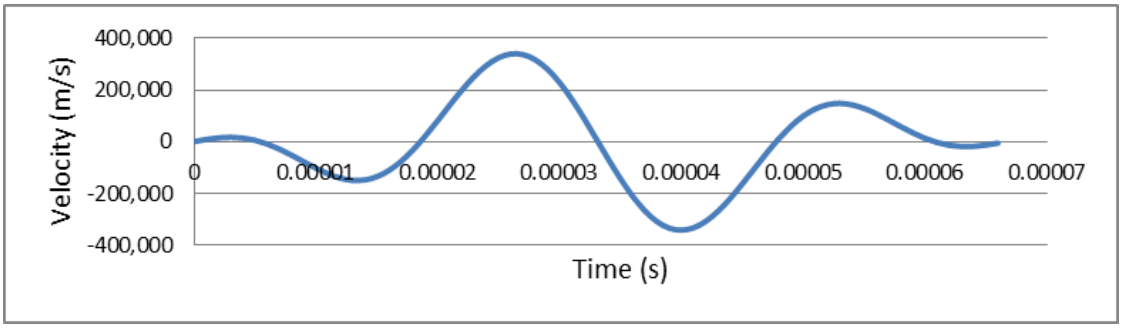

Figure 56. Transmitting signal for simulation.

Refinement of the program was facilitated by comparisons with experimental data in order to properly capture the signals captured by MIRA. To show the similarity in simulated impulse time histories performed with the aforementioned properties and experimental data, an example comparison of an unreinforced concrete slab with no damage is shown in Figure 57. The simulated impulse time history from transducer 1 to 2 is shown via the solid line, while an average of all pairs with 40 mm transducer spacing from experimental data is shown via data points. The simulation matches the experimental data well when viscoelastic material properties are utilized.

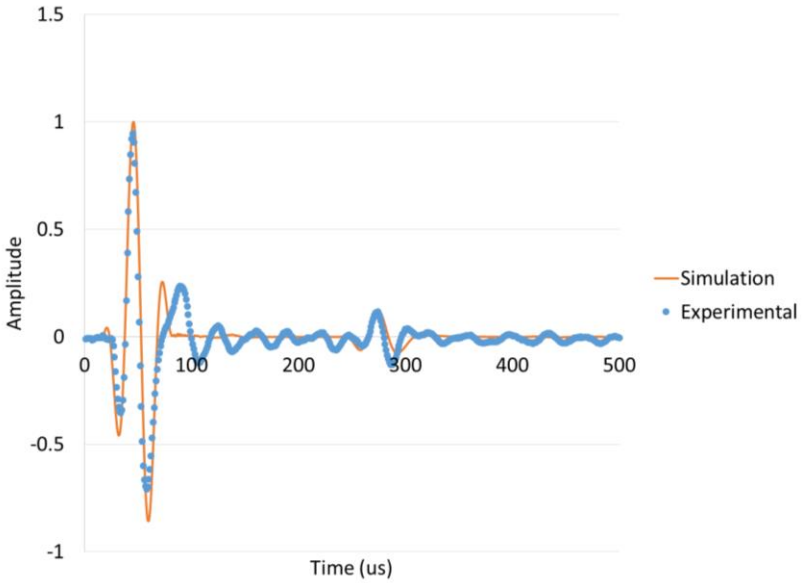

Figure 57. Comparison of simulation signal data to experimental data.

The simulation also allows for the creation of multiple layers with varying material properties, as well as any number of delaminations designated by coordinate boundaries. The delaminated region is modeled such that the density and shear velocity of that region are much lower than that of the sound concrete. These variables are also inputs that can be changed depending upon the type of degradation that is being modeled. The output of the program for the purposes of this research fall under two categories:

1. Wave propagation for each time step
    - Used for visualizing the wave traveling through the specimen and encountering inclusions, boundaries, etc.
2. Impulse time history data for all 45 sensor pairs
    - Used for the quantitative HTI analysis, as well as the creation of reconstructions

6.2 Simulation Trials

To illustrate the capabilities of this simulation, a number of trial analyses were performed. Schematics of the cases which were considered are shown in Figure 58. For all cases, the cross section was an unreinforced concrete slab with a depth of 0.20 m and a width of 0.5 m, with the MIRA device placed 0.1 m from the leftmost edge (as shown in case I, the control case). The damaged cases incorporated two, four, six or eight cracks of 0.05 m depth and either 0.005 m (cases II, III, and IV) or 0.01 m (cases V and VI) width. All simulation inputs stayed constant other than these inclusion coordinates. It is worth noting that these damage scenarios do not align with the manifestations of damage seen in ASR and freeze thaw-damaged specimens, but they serve well as an example of the effect of general degradation on the linear array output.

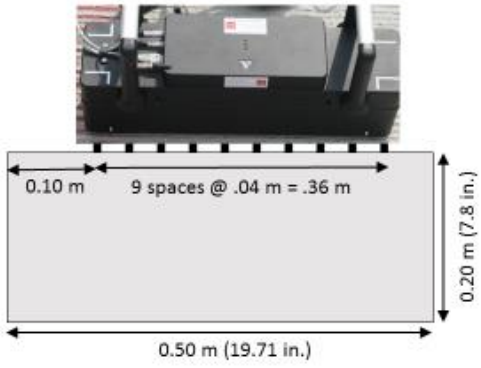

Case I

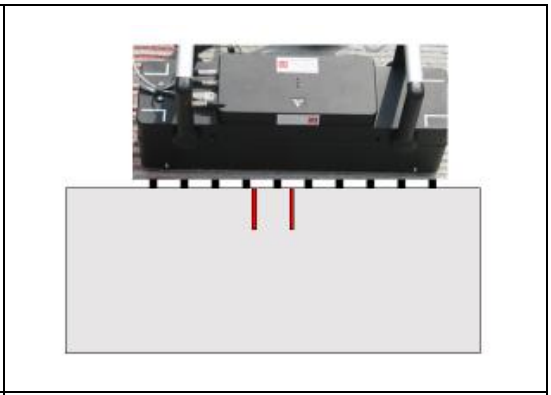

Case II

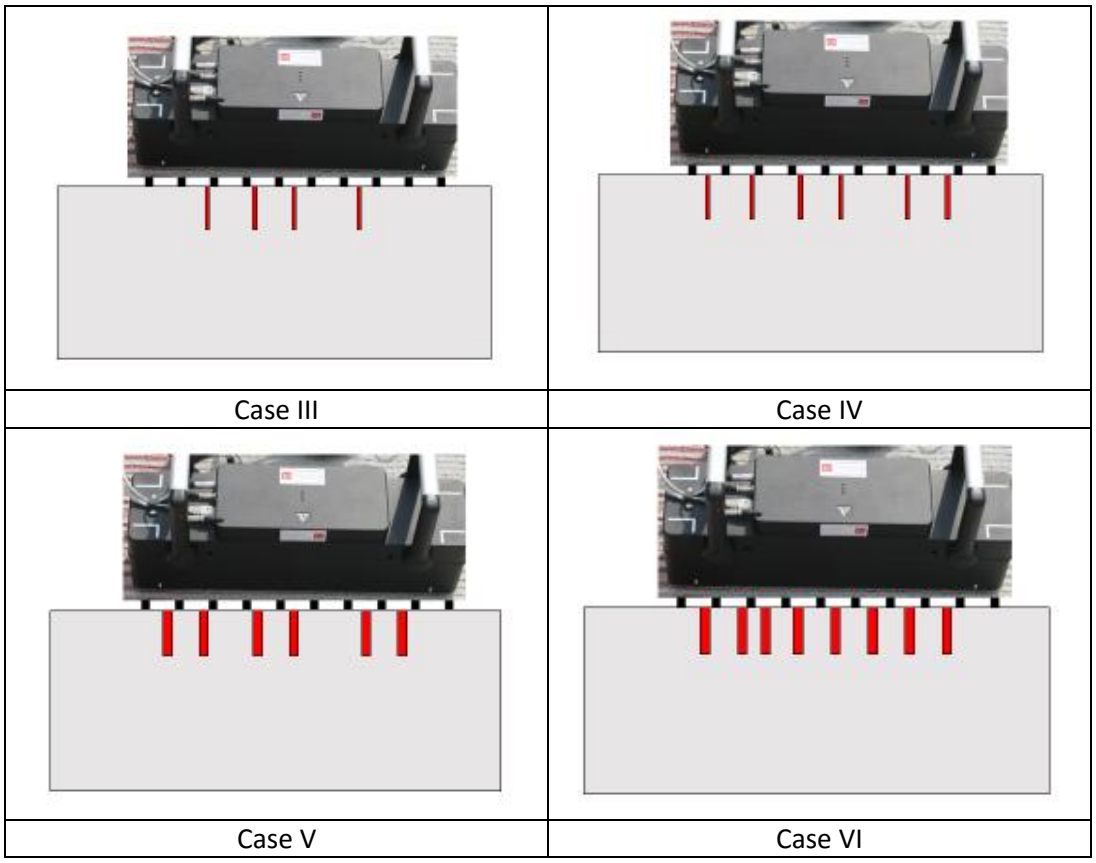

Figure 58. Cross sections used for simulation case studies.

6.2.1 Simulated Wave Propagation

As mentioned previously, the simulation creates a visualization of the wave propagation for each case. The wave propagation paths were visualized in order to better understand the altered wave paths caused by the presence of changes in acoustic impedance such as cracks and inclusions. An example time set of the wave propagation seen for sound concrete (case I) is shown in Figure 59. A time step of 0.00002 seconds was used between frames. In these images, the wave propagation is shown for the wave emitted from transducer 1. A typical wave path when no inclusions are present can be seen. In contrast, the same images for case IV are shown in Figure 60. As can be seen from these

visualizations, the wave propagation is altered by the presence of the cracks, aptly causing the signal deviations which were seen in the experimental data sets.

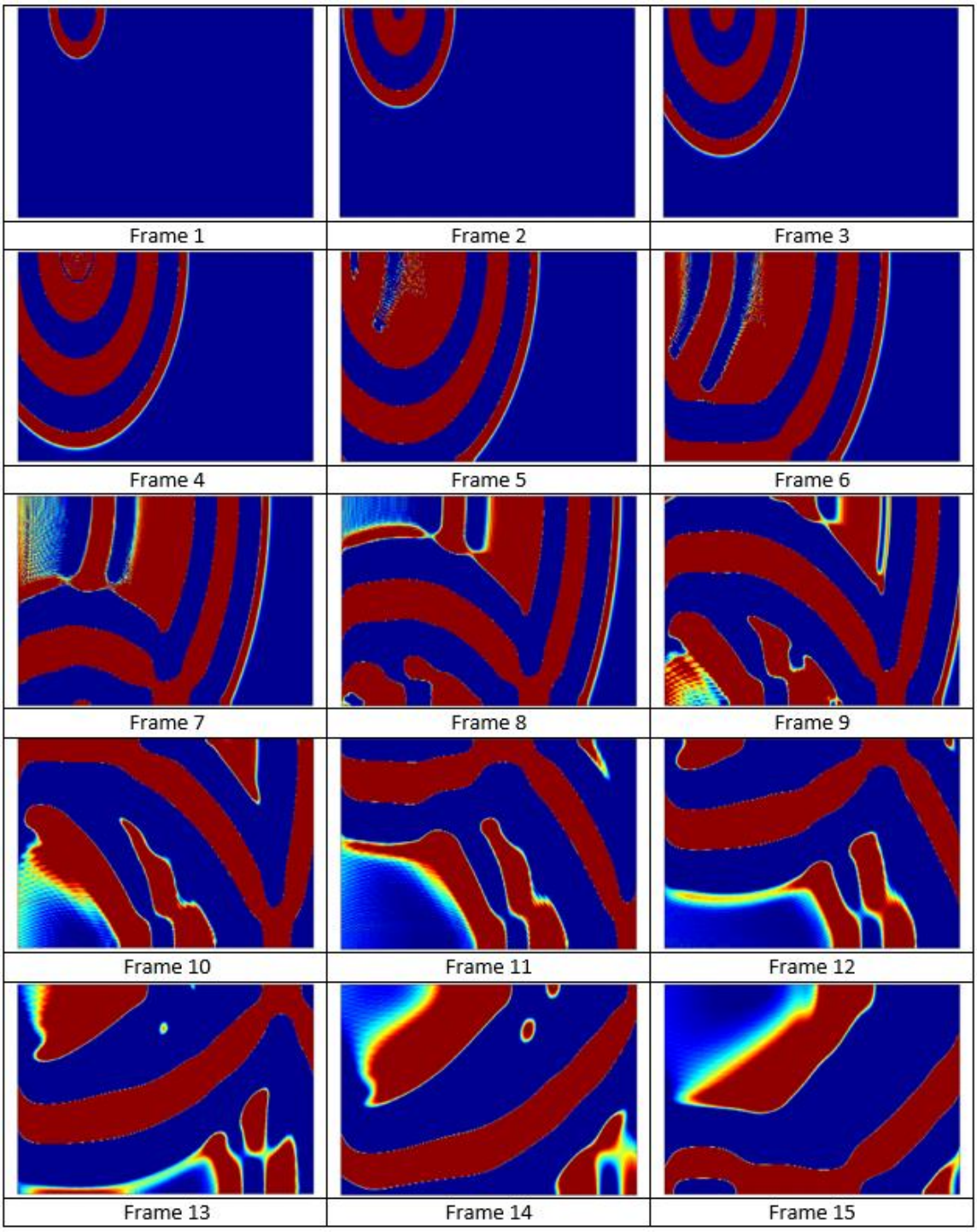

Figure 59. Wave propagation visualization for Case I, no cracks.

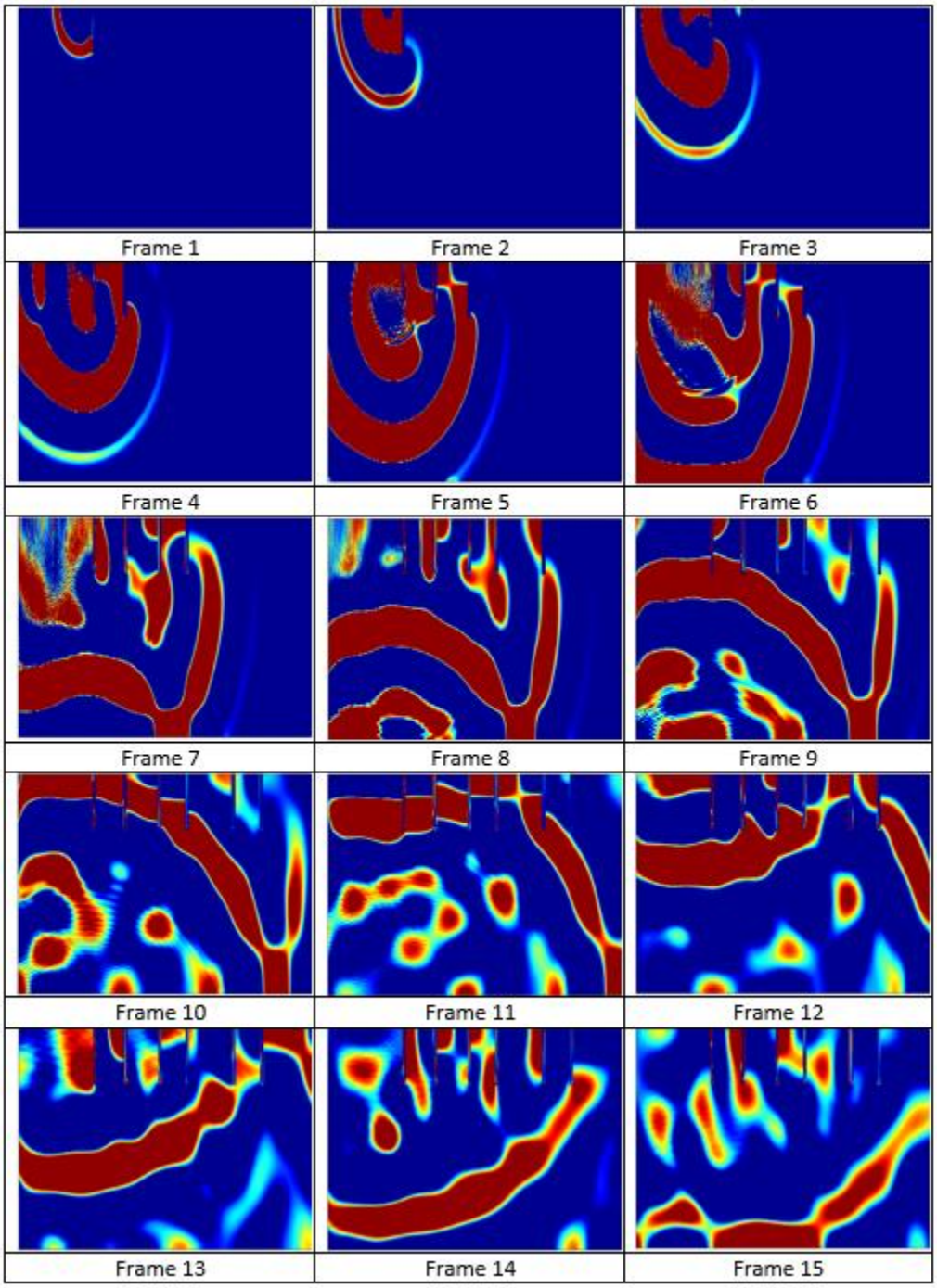

Figure 60. Wave propagation visualization for Case IV, 6 slender cracks.

While these visualizations show that the simulated wave propagation is as would be expected and performing correctly, further verification was achieved via a comparison

of the raw signals for sound and damaged concrete. The raw signals for sensor 2 to 3 for cases I and V are shown in Figure 61. The signal for case I matches the experimental data well, as discussed and shown in Figure 57, and differences occur between the sound and damaged cases. There is a distinct lack of direct arrival impulse of high magnitude as is typically seen, due to the presence of cracks inhibiting this wave path. While it appears that the overall magnitude of the signal for case V is not comparable to case I, this is negligible due to the normalization of the signal in the HTI process. A further analysis of the simulated HTI values is discussed in the following section.

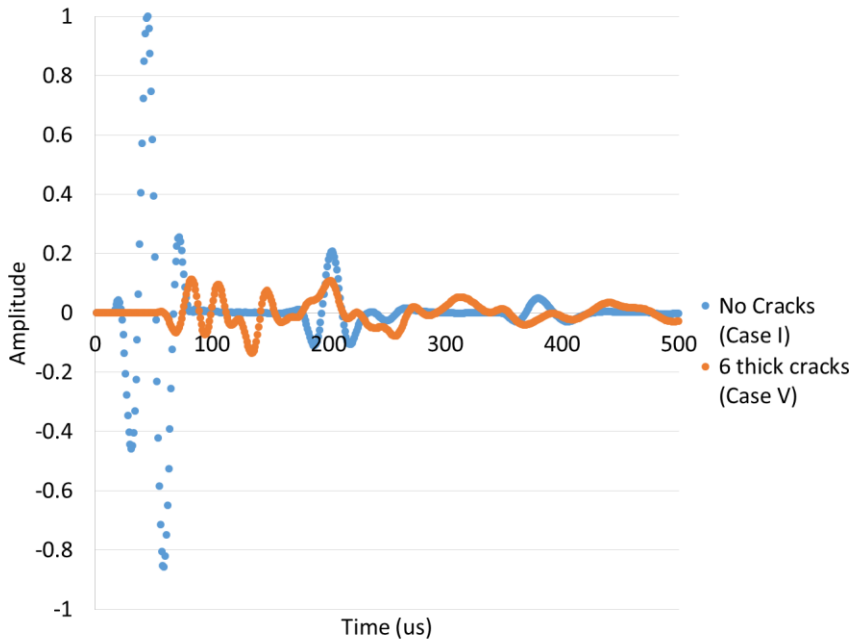

Figure 61. Simulated signal data for sound and damaged concrete cases.

6.2.2 Verification of HTI Results

The results from these six trial cases were then used to calculate the HTI values which resulted from the simulated impulse time history data. The results of the HTI analysis are shown in Table 11. As can be seen, the HTI values increase in a very

systematic and consistent manner as the number and size of the simulated cracks increase. The HTI values associated with the thick cracks in cases V and VI are similar in magnitude for those seen in the medium to severely damaged range, as observed in the freeze thaw investigation (slab D). This suggests that the level of damage present in that experimental slab is on par with the degradation present in the simulation cross sections of case V and VI. This is an important takeaway, as the indicator scaled appropriately in the simulation trials such that the increase in HTI with an increased presence of damage was confirmed. Moreover, the simulated sound cross section had a corresponding HTI value which was consistent with those seen in the experimental investigations of undamaged slabs for both ASR and freeze thaw damage investigations.

Table 11. Simulation trial results

Case	Description	Average HTI
I	No cracks	60.7
II	2 slender cracks	78.9
III	4 slender cracks	99.4
IV	6 slender cracks	108.1
V	6 thick cracks	117.4
VI	8 thick cracks	123.0

6.2.3 Simulated Reconstructions

The simulated impulse time histories were also used to create reconstructions of the trial cross sections. This process revealed that the standard methods implemented for previous research efforts could not be cohesively utilized for the simulated cross sections

containing cracks. This complication arises from the effect of damage on the direct arrival impulse which is used to calculate the shear wave velocity. The shear wave velocity is critical for the creation of reconstructions, as this information yields the locations of increased reflectivity. If calculated incorrectly, the reconstruction is no longer valid and observations as to the condition of the cross section cannot be made.

The complexity associated with the cases considered is the result of the depth of the cracks which were simulated. Because of the relatively large depth, the wave must travel substantially further than expected for other shallow damage or sound concrete scenarios. This situation is illustrated in Figure 62. In this schematic, the shear-horizontal wave is sent from transducer 1 and received by transducer 10, a transducer spacing of 360 mm. However, the wave travels a distance greater than 360 mm, as shown by the dotted line. As such, the transducer spacing which is used in the velocity calculation (360 mm) is inaccurate as the actual travel distance is much greater. This has even more of an effect on closely spaced transducers with damage in between, i.e. transducer pair 4 and 5 in Figure 62, as the direct arrival path is multiple times greater than that of the transducer spacing when a crack is present between them. To overcome this issue for the purposes of simulation validation, the shear wave velocity was manually entered as opposed to calculated based upon direct arrival signal data. This approach is justified in that the shear wave velocity is an input for the simulation and is thus a known and defined value.

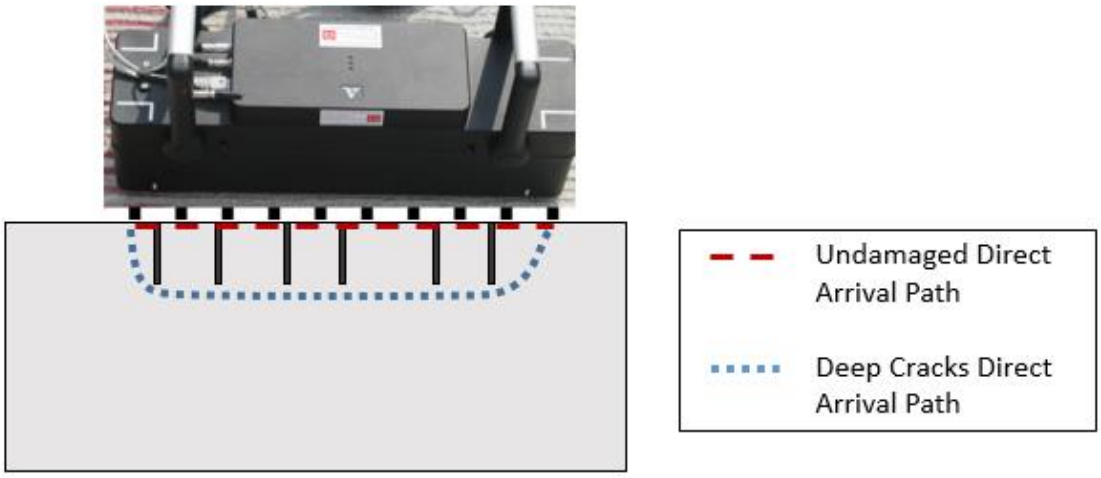

Figure 62. Effect of deep cracks on direct arrival path.

Reconstructions were created using this manual shear wave velocity input approach. The reconstructions for the six cases which were simulated are shown in Figure 63. The reconstruction for case I is consistent with those seen for sound concrete cross sections from the experimental investigation. There is a strong and consistent backwall presence with a lack of increased reflectivity in the remainder of the image. As the number and size of cracks increase for the remaining cases, areas of higher reflectivity are evident, especially for case VI. The reconstruction for case VI was visualized using the same threshold as the other 4 damaged cases, though there are much higher backwall intensities and regions of increased reflectivity throughout. This is indicative of a deviation from the sound condition. For cases II-IV there is a clear change in backwall visualization, as was seen in reconstructions for damaged concrete in both the reinforced concrete column subjected to earthquake loading and the concrete slabs suffering from freeze thaw and ASR damage.

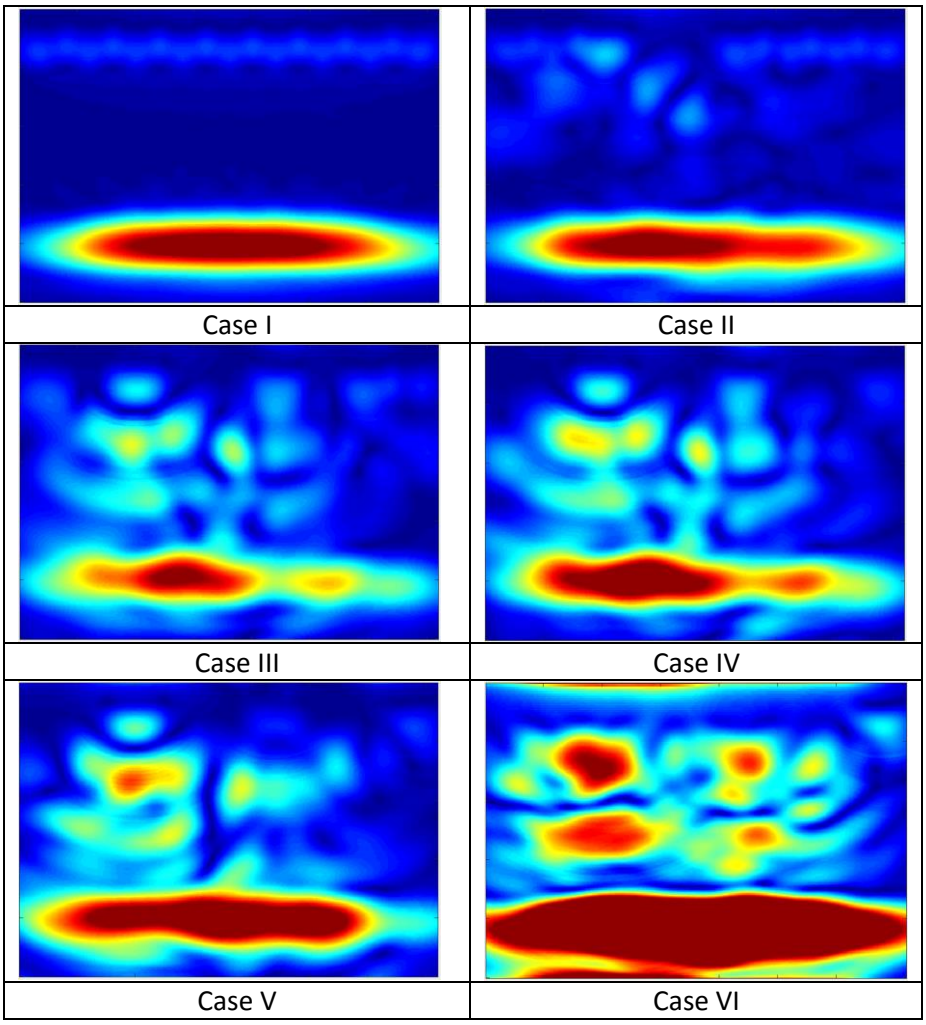

Figure 63. Simulated reconstructions for six cases.

It is worth again noting that the areas of higher reflectivity in the above images are not indicative of the boundaries of the damage present, as was mentioned regarding the environmental damage investigation results. In other words, the reconstructions cannot be used to precisely detect the shape or location of the damage. This is especially true for near surface damage, such as the cracks modeled in this simulation case study. More often, the presence of this damage does not appear as shallow areas of increased reflectivity, but rather as a shadowing of the backwall. This is one of the reasons for the

creation of the HTI analysis in order to address some of the shortcomings of the subjective visual reconstruction analysis.

6.2.4 Conclusions

The successful refinement of the simulation and incorporation of viscoelastic properties allowed for both sound and damaged concrete to be analyzed accurately. The simulation now adequately mirrors the impulse time histories seen in the experimental MIRA data. Moreover, this simulation was able to verify the results that were seen in the experimental investigation regarding the quantitative indicator, the Hilbert Transform Indicator. The trial cases which were performed showed that the HTI values increased systematically with increases in damage. As such, the simulation further confirmed that HTI values are capable of categorizing the condition of concrete in a nondestructive and quantitative manner. The simulation results were also used to create reconstructions, though manual shear wave velocity entry was required due to the effect of deep cracks on the direct arrival impulse.

Deeper understanding was also gained regarding the propagation of shear-horizontal waves in both sound and damaged concrete. This was made possible by the visualization at discrete time steps. This knowledge helps to verify the changes in signal shapes which are captured by the HTI analysis. Further utilization of this simulation will allow for the analysis of a variety of damage mechanisms and thus enable comparative analyses of experimental data from other types of degradation.

CHAPTER 7: SUMMARY

This dissertation reports on the investigation of advancements in nondestructive testing technology using ultrasonic linear array from a damage detection standpoint. This research included two phases of experimental investigation regarding load-induced and environmental damage scenarios. The visual reconstruction analysis was successful in detecting damage in a reinforced concrete column subjected to earthquake loading, and the subsequent quantitative analysis using an adaptation of Pearson's correlation helped to overcome the subjective nature of previous visual reconstruction methods. However, the analysis of load-induced damage in small unreinforced concrete beams revealed the weaknesses in solely utilizing shear wave velocity as a means of damage detection due to accuracy issues.

The panoramic reconstruction analysis and the development of a quantitative indicator of damage, HTI, were successful results of the investigation of environmental damage. The panoramic reconstructions exhibited common characteristics associated with backwall presence and regions of increased reflectivity which allowed for the diagnosis of the condition of the concrete in a visual manner. The HTI analysis revealed that the indicator was capable of detecting damage in an objective and consistent manner, regardless of mix design, climate conditions, and reinforcement presence. This standalone calculation allows for the in-situ diagnosis of concrete condition, without requiring historical data for a comparative analysis. The HTI analysis was successful in detecting both freeze thaw and ASR damage, as were the panoramic reconstructions.

To further understand the signal results that were seen, the development and refinement of a simulation program allowed for verification experimental findings. Furthermore, the simulation allowed for a deeper understanding of shear-horizontal wave propagation. The simulation confirmed the experimental results seen in both the reconstruction and quantitative indicator analyses. The culmination of the experimental and numerical simulation research tasks resulted in the detection and severity of damage in concrete to be determined via nondestructive testing.

7.1 Future Work Recommendations

This thesis presented a variety of applications for damage detection in concrete specimens using an ultrasonic linear array device. However, a multitude of other damage types can be addressed using the same or similar analysis techniques to achieve broader implementation success. One such scenario includes monitoring the structural health of concrete bridge decks, specifically for delamination detection purpose.

Moreover, the techniques developed and presented here could be advanced to determine the depth and/or extent of damage. Accurate knowledge of subsurface degradation could be beneficial for repair and rehabilitation efforts, and could lead to more educated decision making.

While the reconstruction and numerical indicator methods included in this research were successful in detecting the damage types considered, greater achievements could be attained via the fusion of other technologies with these techniques. For instance, it would be difficult, using only the methods presented here, to analyze a scenario in which a specimen contains reinforcement and also has significant subsurface damage and

near surface delaminations. However, if the ultrasonic array technology was combined with magnetic methods, for example, both the reinforcement and the damage present in the structure could be successfully detected. Technological collaborations such as this would allow for greater applicability and enhance the capabilities of the nondestructive evaluation of concrete.

Additionally, automating the methods developed for this thesis could improve efficiency and reduce the analysis time required for condition determinations. Increased automatization would allow for real-time field implementation and diagnosis capabilities. Future work should coninue to improve the productivity of the analysis techniques for future applications.

REFERENCES

ACI Committee 318. (2011). Building Code Requirements for Reinforced Concrete and Commentary (ACI 318-11/ACI 318R-11). American Concrete Institute, Detroit, MI.

Arndt, R. W., Cui, J. and Huston, D. R. (2011). Monitoring Of Reinforced Concrete Corrosion and Deterioration by Periodic Multi-Sensor Non-Destructive Evaluation. AIP Conference Proceedings. 1371.

ASTM C78 / C78M-15a. (2015). Standard Test Method for Flexural Strength of Concrete, ASTM International, West Conshohocken, PA.

Azari, H., Nazarian, S., and Yuan, D. (2014). Assessing sensitivity of impact echo and ultrasonic surface waves methods for nondestructive evaluation of concrete structures. Construction and Building Materials, 71, 384-391.

Bathe, K.J. (1996). Finite element procedures. Prentice Hall.

Bazant, Z.P., Steffens, A. (2000). Mathematical model for kinetics of alkali-silica reaction in concrete, Cement and Concrete Research, 30: 419-428.

Bazant, Z. P., Zi, G., Meyer, C. (2000a). Fracture mechanistic of ASR in concretes with waste glass particles of different sizes, Journal of Engineering Mechanics, 126, No. 3: 226-232.

Benedetto, A., Manacorda, G., Simi, A. and Tosti, F. (2012). Novel perspectives in bridges inspection using GPR. Nondestructive Testing and Evaluation, 27, 239-251.

Borwick, J. (1990). Microphones: technology and technique, Focal Press Oxford.

Berra, M., Mangialardi, T., Paolini, A. E. (1999). Rapid evaluation of the threshold alkali level for alkali reactive siliceous aggregates in concrete, Cement and Concrete Composites, 21: 325–333.

Berra, M., Faggiani, C., Mangialardi, T., Paolini, A.E. (2010). Influence of stress restraint on the expansive behavior of concrete affected by alkali-silica reaction, Cement and Concrete Research, 40: 1403-1409.

Bishko, A. V., Samokrutov, A. A. and Shevaldykin, V. G. (2008). Ultrasonic Echo-Pulse Tomography of Concrete Using Shear Waves Low-Frequency Phased Antenna Arrays. 17th World Conference on Nondestructive Testing, 25-28.

Bracci, J. M., Kunnath, S. K. and Reinhom, A. M. (1997). Seismic Performance and Retrofit Evaluation of Reinforced Concrete Structures, Journal of Structural Engineering 123(1), 3–10.

Buckley, J. and Loertscher, H. (1999). Frequency considerations in air-coupled ultrasonic inspection. Insight, 41, 696-699.

Cao, Y. (2011). Full Waveform Analysis of Ground Penetrating Radar Measurements. University of Minnesota.

Cao, Y., Guzina, B. B. and Labuz, J. F. (2008). Pavement evaluation using ground penetrating radar, Minnesota Department of Transportation, MN/RC 2008-10.

Cao, Y., Labuz, J. and Guzina, B. (2011). Evaluating a Pavement System Based on GPR Full-Waveform Simulation. Transportation Research Board 90th Annual Meeting.

Carino, N. J. (2001). The impact-echo method: an overview. Proceedings of the 2001 Structures Congress and Exposition, May, 2001, 21-23.

Catapano, I., Crocco, L., Morabito, A. F. and Soldovieri, F. (2012). Tomographic imaging of holographic GPR data for non-invasive structural assessment: the Musmeci bridge investigation. Nondestructive Testing and Evaluation, 27, 229-237.

Chen, J., Jayapalan, A.R., Kim, J., Kurtis, K.E., Jacobs, L.J. (2010). Rapid evaluation of alkali–silica reactivity of aggregates using a nonlinear resonance spectroscopy technique, Cement and Concrete Composites, 40: 914–923.

Choi, H. and Popovics, J. S. (2015). NDE application of ultrasonic tomography to a full-scale concrete structure. Ultrasonics, Ferroelectrics, and Frequency Control, IEEE Transactions on, 62(6), 1076-1085.

Clemena, G. G. (1991). Short-pulse radar methods.

Clemeña, G. G., Jackson, D. R. and Crawford, G. C. (1992). Inclusion of rebar corrosion rate measurements in condition surveys of concrete bridge decks. Transportation Research Record.

Deroo, F., Kim, J. Qu, K. Sabra, G. Woodruff, W., and Jacobs, L.J. (2010). Detection of damage in concrete using diffuse ultrasound (L), Journal of Acoustical Society of America, 127, (6): 3315-3318.

Donnelly, J. (2012). “Means and Methods of Evaluating Reinforced Concrete Structures,” ACI Fall 2012 Convention, October 21-24; Toronto, ON.

Economou, N., Vafidis, A., Hamdan, H., Kritikakis, G., Andronikidis, N. and Dimitriadis, K. (2012). Time-varying deconvolution of GPR data in civil engineering. Nondestructive Testing and Evaluation, 27, 285-292.

Fellinger, P. (1991). A Method for the Numerical Solution of Elastic Wave Propagation Problems in the Time Domain by Direct Discretization of the Elastodynamic Governing Equations. PhD Thesis, University of Kassel, Kassel,

Germany.

Freeseman, K., Hoegh, K., Khazanovich, L. (2015). Characterization of Concrete at Various Freeze-Thaw Damage Conditions Using SH-Waves. Proceedings of the 42nd Review of Progress in Quantitative Nondestructive Evaluation (QNDE), 26-31 July, Minneapolis, MN. http://dx.doi.org/10.1063/1.4940463.

Freeseman, K., Khazanovich, L., Hoegh, K., Nojavan, A., Schultz, A. E., Chao, S. (2016). Nondestructive monitoring of subsurface damage progression in concrete columns damaged by earthquake loading. Engineering Structures, Volume 114, 1 May 2016, 148-157.

Ghee, A. B., Priestley, M. J. N., and Paulay, T. (1989). Seismic Shear Strength of Circular Reinforced Concrete Columns. Structural Journal, American Institute of Concrete. 86(1), 45-59.

Giaccio, G., Zerbino, R., Ponce, J.M., Batic, O.R. (2008). Mechanical behavior of concretes damaged by alkali-silica reaction. Cement and Concrete Research, 38: 993-1004.

Godinho, L., Dias-da-Costa, D., Areias, P., Júlio, E., and Soares, D. (2013). Numerical study towards the use of a SH wave ultrasonic-based strategy for crack detection in concrete structures. Engineering Structures, 49, 782-791.

Graveen, Cole. M.S.C.E., Purdue University. (2001). Nondestructive Test Methods To Assess Pavement Quality For Use In A Performance-Related Specification. Major Professor: W. Jason Weiss.

Graves, R.W. (1988). Simulating seismic wave propagation in 3D elastic media using staggered-grid finite differences. Bull. Seismic Soc. Am., 86, 1091–1106.

Griffiths, D. J. and Reed, C. (1999). Introduction to electrodynamics, prentice Hall New Jersey.

Hoegh, Kyle Edward. (2013). Ultrasonic linear array evaluation of concrete pavements. Retrieved from the University of Minnesota Digital Conservancy, http://purl.umn.edu/155823.

Hoegh, K., Khazanovich, L., Maser, K. R. and Tran, N. (2012a). Evaluation of Ultrasonic Technique for Detecting Delamination in Asphalt Pavements. Transportation Research Board 91st Annual Meeting.

Hoegh, K., Worel, B., Yu, H. T., and Khazanovich, L. (2013). Detection of Subsurface Joint Deterioration. Transportation Research Record: Journal of the Transportation Research Board. Volume 2367. Issue 1: 3-12.

Hoegh, K. and Khazanovich, L. (2012b). Correlation Analysis of 2D Tomographic Images for Flaw Detection in Pavements. Journal of Testing and Evaluation.

American Society for Testing and Materials 40(2): 247-255.

Hoegh, K. and Khazanovich, L. (2012). Concrete Pavement Joint Diagnostics Using Ultrasonic Tomography. Transportation Research Record: Journal of the Transportation Research Board. Volume 2305: 54–61.

Hoegh, K., Yu, H. T., and Khazanovich, L. (2011). Ultrasonic Tomography Technique for Evaluation of Concrete Pavements. Transportation Research Record: Journal of the Transportation Research Board. Volume 2232: 85–94.

Hoegh, K. and Khazanovich, L. (2015). Extended Synthetic Aperture Focusing Technique for Ultrasonic Imaging of Concrete. NDT & E International. doi:10.1016/j.ndteint.2015.05.001.

Kim, G., In, C. W., Kim, J. Y., Kurtis, K. E., and Jacobs, L. J. (2014). Air-coupled detection of nonlinear Rayleigh surface waves in concrete—Application to microcracking detection. NDT & E International, 67, 64-70.

Langenberg, Karl-Jörg, René Marklein, and Klaus Mayer. (2012). Ultrasonic Nondestructive Testing of Materials: Theoretical Foundations. CRC Press.

Leśnicki, K. J., Kim, J. Y., Kurtis, K. E., and Jacobs, L. J. (2011). Characterization of ASR damage in concrete using nonlinear impact resonance acoustic spectroscopy technique. NDT & E International, 44(8), 721-727.

Leśnicki, K. J., Kim, J. Y., Kurtis, K. E., and Jacobs, L. J. (2013). Assessment of alkali–silica reaction damage through quantification of concrete nonlinearity. Materials and structures, 46(3), 497-509.

Levander, A. (1988). Fourth-order finite-difference P-SV seismograms. Geophysics, 53, 1425–1436.

Li, J., Zollinger, D. G. and Lytton, R. L. (2008). Detection of delamination in concrete pavements using ground-coupled ground-penetrating radar technique. Transportation Research Record: Journal of the Transportation Research Board, 2087, 68-77.

Lingvall, F., Olofsson, T., and Stepinski, T. (2003). Synthetic aperture imaging using sources with finite aperture: Deconvolution of the spatial impulse response. The Journal of the Acoustical Society of America 114.1: 225-234. http://dx.doi.org/10.1121/1.1575746.

Maser, K. R. (1996). Condition assessment of transportation infrastructure using ground-penetrating radar. Journal of infrastructure systems, 2, 94-101.

Maser, K. R. (2000). Pavement characterization using ground penetrating radar: State of the art and current practice. ASTM special technical publication, 1375, 313-326.

Maser, K. R. (2008). Integration of Ground Penetrating Radar and Infrared Thermography for Bridge Deck Condition Evaluation. Proceedings of the Symposium of NDE/NDT for Highways and Bridges, SMT, 2008. Citeseer, 67-74.

Maser, K. R. and Roddis, W. M. K. (1990). Principles of thermography and radar for bridge deck assessment. Journal of transportation engineering, 116, 583-601.

Morey, R. M. (1998). Ground penetrating radar for evaluating subsurface conditions for transportation facilities, Transportation Research Board.

Mozco, P., Kristek, J., and Galis, M. (2014). The finite Difference Modeling of Earthquake Motions. Cambridge University Press.

Mozco, P., Kristek, J., Galis, M., and Pazak, P. (2010). On accuracy of the finite-difference and finite-element schemes with respect to P-wave to S-wave speed ratio. Geophysical Journal International, 493-510.

Moczo, P., Kristek, J., Vavryˇcuk, V., Archuleta, R.J., and Halada, L. (2002). 3D heterogeneous staggered-grid finite-difference modeling of seismic motion with volume harmonic and arithmetic averaging of elastic moduli and densities. Bull. Seismic Soc. Am., 92, 3042–3066.

Multon, S., Cyr, M., Sellier, A., Diederich, P., Petit, L. (2010). Effects of aggregate size and alkali content on ASR expansion. Cement and Concrete Research, 40: 508 - 516.

Multon, S., Sellier, A., Cyr, M. (2009). Chemo–mechanical modeling for prediction of alkali silica reaction (ASR) expansion. Cement and Concrete Research, 39: 409 - 500.

NCHRP. (2003). Guide for Mechanistic-Empirical Design of New and Rehabilitated Pavement Structures. Final Report, NCHRP Project 1-37A, National Cooperative Highway Research Program, Transportation Research Board, National Research Council, Washington, D.C.

Nojavan, A., Schultz, A. E., Chao, S-H., Haselton, C., Simasathien, S., Palacios, G., and Liu, X. (2014). Preliminary Results for NEESR Full-Scale RC Column Tests under Collapse-Consistent Loading Protocols. 10th U.S. National Conference on Earthquake Engineering, Anchorage, AK, July 21-25.

Nojavan, A., Schultz, A.E., Haselton, C., Simathathien, S., Liu, X., and Chao, S-H. (2015). A New Dataset for Full-Scale RC Columns under Collapse-Consistent Loading Protocols. Earthquake Spectra, EERI, 31(2): 1211-1231.

NRMCA. (2006). Concrete in Practice: What, Why and How? CIP 39- Maturity Methods to Estimate Concrete Strength. National Ready Mixed Concrete Association. Silver Spring MD.

Olek, J., M. D. Cohen, C. F. Scholer, and D. R. Mandrekar. (2003). Use of Modulus of Rupture, Fatigue Resistance and Maturity in Determining Opening to Traffic Time for Concrete Pavements. Publication FHWA/IN/JTRP-2000/25. Joint Transportation Research Program, Indiana Department of Transportation and Purdue University, West Lafayette, Indiana.

Olsen, K.B., Archuleta, R.J., Matarese, J.R. (1995). Magnitude 7.75 earthquake on the San Andreas Fault: three-dimensional ground motion in Los Angeles, Science. 270, 1628–1632.

Park, Y.-J., and Ang, A. H.-S. (1985). Mechanistic Seismic Damage Model for Reinforced Concrete. Journal of Structural Engineering, 111(4), pp. 722–739.

Pitarka, A. (1999). 3D elastic finite-difference modeling of seismic motion using staggered grids with nonuniform spacing. Bull. seism. Soc. Am., 89, 54–68.

Plati, C. and Loizos, A. (2012). Using ground-penetrating radar for assessing the structural needs of asphalt pavements. Nondestructive Testing and Evaluation, 27, 273-284.

Popovics, J. S., Oh, T. and Ham, S. (2012). Effective visualization of impact-echo data for bridge deck NDE. AIP Conference Proceedings. 1681.

Popovics, S. and Popovics, J. S. (1992). A critique of the ultrasonic pulse velocity method for testing concrete. Nondestructive testing of concrete elements and structures. ASCE, 94-103.

Qu, J., Bazant, Z., Jacobs, L. J., and Guimaraes, M. (2015). Nonlinear ultrasonic diagnosis and prognosis of ASR damage in dry cask storage. Project. No. 12-3736. Nuclear Energy University Programs (NEUP). U. S. Department of Energy.

Rohne, Ryan J., and Bernard I. Izevbekhai. (2009). Demonstration of Concrete Maturity Test Process on the TH-694/ TH-35E Interchange - Unweave the Weave. Rep. no. MN/RC 2009-26.

Schickert, M., Krause, M. and Müller, W. (2003). Ultrasonic imaging of concrete elements using reconstruction by synthetic aperture focusing technique. Journal of Materials in Civil Engineering, 15, 235-246. Permalink: http://dx.doi.org/10.1061/(ASCE)0899-1561(2003)15:3(235).

Schubert, F. and Koehler, B. (2001). Three-dimensional time domain modeling of ultrasonic wave propagation in concrete in explicit consideration of aggregates and porosity. Journal of computational acoustics, 9, 1543-1560.

Schubert, F. and Köhler, B. (2008). Ten lectures on impact-echo. Journal of Nondestructive Evaluation, 27, 5-21.

Schubert, F., Lausch, R. and Wiggenhauser, H. (2003). Geometrical effects on

impact-echo testing of finite concrete specimens. Proceedings of International Symposium Non-Destructive Testing in Civil Engineering (NDT-CE), 16-19.

Scott, M., Duke, J. C., Davidson, N., Washed, G. and Weyers, R. (2000). Automated characterization of bridge deck distress using pattern recognition analysis of ground penetrating radar data. Materials evaluation, 58, 1305-1309.

Scott, M., Rezaizadeh, A., Delahaza, A., Santos, C. G., Moore, M., Graybeal, B. and Washer, G. (2003). A comparison of nondestructive evaluation methods for bridge deck assessment. NDT & E International, 36, 245-255.

Scullion, T. and Saarenketo, T. (1995). Ground penetrating radar technique in monitoring defects in roads and highways.

Shevaldykin, V. G., Samokrutov, A. A., and Kozlov, V. N. (2002). Ultrasonic Low-Frequency Transducers with Dry Dot Contact and Their Applications for Evaluation of Concrete Structures. IEEE Ultrason. Symp. Proc., Vol. 1–2, 2002, pp. 793–798.

Takeda, Toshikazu, Sozen, M. A. and Nielsen, N. Norby. (1970). Reinforced Concrete Response to Simulated Earthquakes. Journal of Structural Engineering, American Society of Civil Engineers, December 1970.

Voigt, Th., Ch. U. Grosse, Z. Sun, S. P. Shah, and H. -W. Reinhardt. (2005). Comparison of Ultrasonic Wave Transmission and Reflection Measurements with P- and S-waves on Early Age Mortar and Concrete. Materials and Structures 38.8: 729-38.

Voigt, T., G. Ye, Z. Sun, S. Shah, And K. Vanbreugel. (2005). Early Age Microstructure of Portland Cement Mortar Investigated by Ultrasonic Shear Waves and Numerical Simulation. Cement and Concrete Research 35.5, 858-66.

Voigt, Thomas, Yilmaz Akkaya, and Surendra P. Shah. (2003). Determination of Early Age Mortar and Concrete Strength by Ultrasonic Wave Reflections. Journal of Materials in Civil Engineering 15.3.

Vosooghi, A. and Saiidi, M. (2013). Shake-Table Studies of Repaired Reinforced Concrete Bridge Columns Using Carbon Fiber-Reinforced Polymer Fabrics. ACI Structural Journal, V. 110, No. 11, Jan-Feb., pp. 105-114.

Weiland, T. (1977). A discretization method for the solution of Maxwell's equations for six-component fields. Electronics and Communication (AEÜ), vol. 31, p. 116.

Zhu, J. and Popovics, J. (2002). Non-contact detection of surface waves in concrete using an air-coupled sensor. AIP Conference Proceedings, 2002. 1261.

Zhu, J. and Popovics, J. S. (2007). Imaging concrete structures using air-coupled impact-echo. Journal of engineering mechanics, 133, 628-640.

Zhu, J., Popovics, J. S. and Schubert, F. (2004). Leaky Rayleigh and Scholte waves at the fluid–solid interface subjected to transient point loading. The Journal of the Acoustical Society of America, 116, 2101.